Control of a Battery Energy Storage and STATCOM for Black Start Services

A Study on Power System Restoration in PSCAD

MSc. 4th Semester - Master Thesis

Julian Klaus Schwarzkopf & Marc Walti

AAU Energy
Aalborg University
http://www.energy.aau.dk

AALBORG UNIVERSITY
STUDENT REPORT

Title:
Control of a Battery Energy Storage and STATCOM for Black Start Services

Theme:
Master Thesis

Project Period:
Spring Semester 2024

Project Group:
EPSH4-1030

Participant(s):
Julian Klaus Schwarzkopf
Marc Walti

Supervisor(s):
Sanjay Chaudhary
Rakesh Sinha

Page Numbers: 95

Date of Completion:
May 30, 2024

Abstract:

Due to the decommissioning of conventional power plants to achieve climate targets, the development and implementation of non-traditional black start service providers is of utmost importance to ensure the restoration of normal operation in future power systems after blackouts. This master's thesis presents the application of a STATCOM with an integrated battery storage system (STATCOM-BESS) with grid-forming (GFM) control. The aim is to create a power island by energising segments of a transmission system with an overhead line and transformers and a distribution system with a grid-following (GFL) unit as well as static and dynamic loads. The EMT simulations in PSCAD demonstrate the overall black start capabilities of the developed STATCOM-BESS control structure by providing fast power and an inert frequency response to sudden load changes as well as a stable interaction with the GFL unit. Compliance with the black start requirements specified by the Belgian and British transmission system operators (TSO) is achieved.

Preface

This master's thesis was written by Julian Klaus Schwarzkopf and Marc Walti, students of the MSc. in *Electrical Power Systems and High Voltage Engineering* at Aalborg University. It was written from February to May in the spring semester of 2024 and explores the subject of power system restoration with non-traditional black start service providers. The simulations in this project were carried out with PSCAD and MATLAB/Simulink. For graphs and data processing MATLAB was used. Furthermore, *draw.io* was used for illustrations.

We want to express our sincere thanks to our supervisors Sanjay Chaudhary and Rakesh Sinha for their cooperation and guidance throughout this project. We would also like to thank Daniela Pagnani for her collaboration.

Aalborg University, May 30, 2024

Instructions for reading

This report is written in LaTeX, and each chapter is marked with a certain number and is divided into sections. All the references used throughout the report are indicated by the method referred to as the Institute of Electrical and Electronics Engineers (IEEE). The bibliography is made in Mendeley and BibTeX, and the citations used throughout the sections are noted in the text as each individual statement is made. Citations of figures and tables are mentioned in the caption. The figures in this report are all in .pdf format, allowing the reader to zoom in, without the figure pixelation. The best reading experience will be in a digital format.

Julian Klaus Schwarzkopf

Marc Walti

List of Abbreviations

DOL Direct On Line

DSO Distribution System Operator

DER Distributed Energy Resource

ENTSO-E European Network of Transmission System Operators for Electricity

FFT Fast Fourier Transform

GFM Grid-Forming

GFL Grid-Following

IBR Inverter-Based Resources

LPF Low-Pass Filter

MAF Moving Average Filter

MPPT Maximum Power Point Tracking

NGESO National Grid Electrical System Operator

OWPP Offshore Wind Power Plant

PCC Point of Common Coupling

PIR Pre-Insertion Resistor

PLL Phase-Locked Loop

PWM Pulse Width Modulation

RoCoF Rate of Change of Frequency

SCR Short Circuit Ratio

STFT Short-Time Fourier Transform

SG Synchronous Generator

TOV Temporary Overvoltage

TSO Transmission System Operator

VRE Variable Renewable Energy

VSM Virtual Synchronous Machine

WT Wind Turbine

List of Symbols

λ	Magnetic Flux	Wb
ω_m	Mechanical Angular Frequency	rad/s
ω_n	Nominal Angular Frequency	rad/s
ω_0	Characteristic Angular Frequency	rad/s
θ_m	Mechanical Angle of the Rotor	rad
ζ	Damping Constant	-
BW	Bandwidth	Hz
C_f	Filter Capacitance	F
C_{Base}	Base Capacitance	F
$cos(\varphi)$	Power Factor	-
D_p	Damping Constant	-
E_{kin}	Kinetic Energy	Ws
f	Frequency	Hz
f_0	Characteristic Frequency	Hz
H	Inertia Constant	s
i_{abc}	Current in abc Reference Frame	A
i_{dq}	Current in dq Reference Frame	A
J	Total Moment of Inertia	$kg \cdot m^2$
K_f	Droop Constant f-P Droop	-
K_i	Integral Gain	-
K_p	Proportional Gain PI Controller	-
K_q	Droop constant Q-V Droop	-

K_v	Droop Constant V-Q Droop	-
L_f	Filter Inductance	H
P	Active Power	W
P^*	Active Power Reference	W
P_e	Electrical Power	W
P_m	Mechanical Power	W
P_{meas}	Measured Active Power	W
Q	Reactive Power	var
Q^*	Reactive Power Reference	var
Q_{meas}	Measured Reactive Power	var
R	Droop Constant P-f Control	-
S_r	Rated Machine Power	VA
$S_{n,SB}$	Apparent Power of STATCOM-BESS	VA
T_i	Integral Time Constant PI Controller	s
T_{LPF}	Time Constant Low-Pass Filter	s
V	Voltage	V
V_L	Winding Voltage	V
v_n^*	Nominal Voltage Reference	pu
$v_{\alpha\beta}$	Voltage in $\alpha\beta$ Reference Frame	V
v_{abc}	Voltage in abc Reference Frame	V
v_{dq}	Voltage in dq Reference Frame	V
$V_{n,SB}$	Nominal Voltage of STATCOM-BESS	V
Z_{Base}	Base Impedance	Ω

Contents

1 Introduction

The fundamental prerequisite for the successful operation of the power grid is the provision of a reliable and uninterruptible power supply. Despite technological advances in monitoring, control and protection of power grids, the risk of instability due to an increasing number of intermittent energy sources, human factors, technical malfunctions, and extreme weather conditions is omnipresent. In the worst case, instabilities can lead to partial or complete blackouts often due to cascading failures, which confront Transmission System Operator (TSO)s, Distribution System Operator (DSO)s and plant operators with unprecedented challenges. Despite their rare occurrence, blackouts are of significant concern not only for grid and plant operators but also for society, as electricity is a crucial pillar of modern society. This is also emphasised by two current examples in Europe that show the consequences of power outages. [1]–[3]

- **Denmark:** A local fault on the Danish island of Bornholm tripped the submarine cable that connects Bornholm with Sweden in autumn 2022. This led to a power outage lasting several hours on the island with its 40,000 inhabitants. [4]
- **England:** A lightning strike on a transmission line in summer 2019 led to unexpected losses of generation units, resulting in the frequency reserve allocated by the TSO of England being exceeded. This triggered a drop in frequency, which resulted in load shedding and disconnected 1.1 million electricity customers from the grid for 45 minutes during rush hour. This power interruption had severe consequences for rail traffic in particular. [5], [6]

The occurrence of these events requires system restoration strategies to ensure the return to normal operating conditions in the safest and fastest way possible to minimise economic losses and the impact on society [7]. To restore normal operation after a blackout, a black start procedure has to be carried out, i.e. the restoration of a power plant or part of a power grid without depending on external power sources [8].

The traditional restoration strategy of grid operators usually relies on conventional power plants with synchronous generators in the form of fossil fuel-fired generators, pumped storage power plants and, to a much lesser extent, biomass. Interconnectors have also been technically tested and are being used, but these interconnectors are dependent on the neighbouring energy markets. However, many European countries, including the United Kingdom, have committed to the Paris Agreement of 2015 and have set ambitious

goals of decarbonising their electricity system, which should be achieved in the United Kingdom by 2035. Achieving this goal has and will increasingly involve the installation of renewable energy resources, while fossil fuel power plants are being phased out. [7], [9], [10]
A prospective future scenario for the installed capacities for 2022 to 2050 can be seen in Figure 1.1. This is presented in the annual reports *Future Energy Scenarios* [10] published by the British TSO National Grid Electrical System Operator (NGESO).

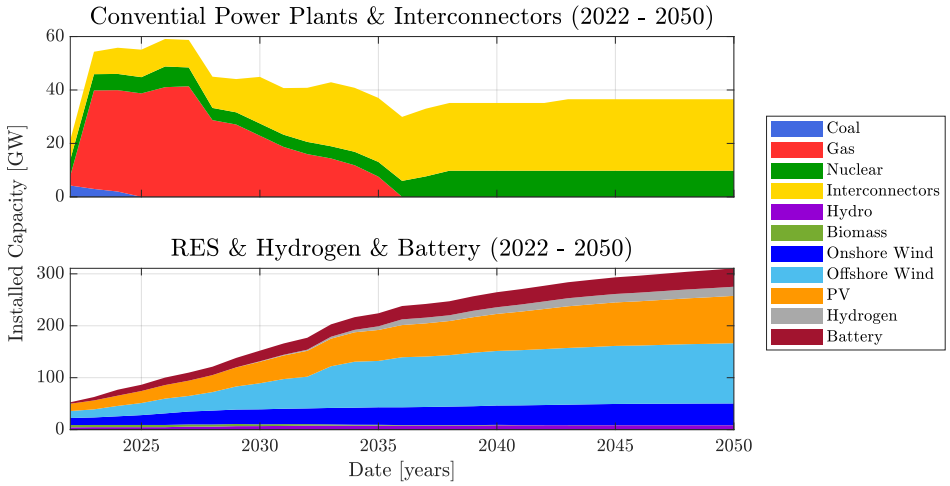

Figure 1.1: Installed capacity in Great Britain for the years 2022-2050 predicted by the scenario *Leading the way* [10], which leads to the fastest credible decarbonisation and thus to the most optimistic scenario of the energy scenarios presented in [10].

This scenario expects that the majority of conventional power plants will be phased out already by approximately 2035, while new technologies such as hydrogen power plants and battery storage systems will be introduced to the market. It can also be noted that Variable Renewable Energy (VRE)s, in particular Offshore Wind Power Plant (OWPP)s, will see enormous growth. This development requires an adaptation of current restoration strategies in Great Britain, as keeping conventional power plants on standby, for the sole purpose of providing black start, is not cost-efficient. Also, starting generators from cold leads to less reliability and longer restoration times. However, to maintain the same level of safety and reliability with new restoration strategies, the basic capabilities of Inverter-Based Resources (IBR) must be expanded to provide black start services in the form of grid-forming control structures, and, if necessary, an auxiliary power supply. [9], [11]

2 State of the Art

This chapter focuses on the challenges and current developments regarding power system restoration. This includes reviewing current restoration strategies and regulations, focusing on concepts and the requirements published by the TSOs of Great Britain and Belgium. In addition, an overview of the challenges when using non-traditional black start service providers and a review of the characteristics of Grid-Following (GFL) and in particular Grid-Forming (GFM) control structures will be given.

2.1 Power System Restoration

The strategies of system operators to achieve power system restoration can be categorised into *Bottom-up* and *Top-down*. The definitions of both strategies, according to [12] and [13], are briefly described below:

- **Bottom-up:** The system re-energisation is carried out by generation units with black start capability within the control area of the respective system operator, including those which are islanded on their house load.
- **Top-down:** This restoration strategy is based exclusively on HVDC or HVAC interconnections and thus on energy from neighbouring TSOs.

Some system operators also rely on a hybrid form, i.e. a combination of *Bottom-up* and *Top-down* strategy [7]. However, due to the change in the energy landscape in Europe towards a higher share of IBRs and a simultaneously declining number of Synchronous Generator (SG)s, as shown in Chapter 1 using Great Britain as a representative example, the number of traditional black start service providers is falling. This development confronts European grid operators with the challenge of outlining the capability requirements for the restoration of future power systems with a high penetration of IBRs without relying on the services provided by SGs [9]. Therefore the TSOs of Belgium and Great Britain, i.e. ELIA and NGESO, have independently conducted studies to assess black start capability requirements for non-traditional black start service providers [9], [14]. These studies are the basis for the following sections.

2.1.1 From Blackout to Restoration

In the event of a blackout, various steps have to be taken to restore normal operation conditions in the power system [9]. Therefore, this section focuses on the steps required

for power system restoration after a blackout event, following the *Bottom-up* restoration strategy illustrated in Figure 2.1, which has been introduced by NGESO in [9].

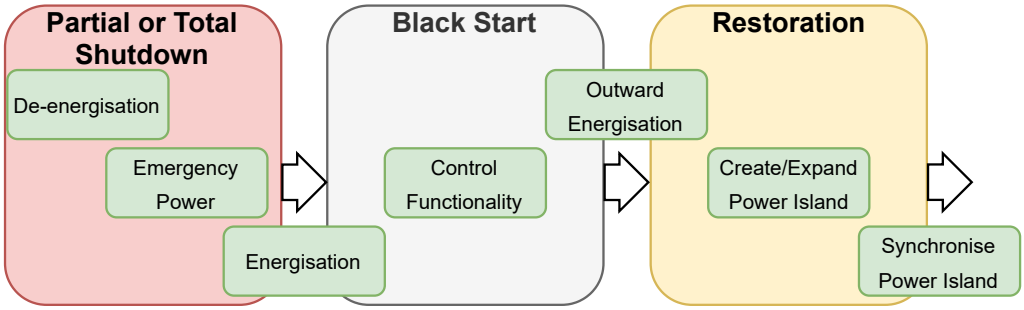

Figure 2.1: Stages for a power system restoration based on non-traditional black start service providers. Based on [9].

Figure 2.1 shows that the restoration process is characterised by three main phases: *Partial or Total Shutdown*, *Black Start* and *Restoration*, in order to create microgrids, so-called power islands, to gradually extend the energisation of the network [9]. The specific intermediate steps, shown in Figure 2.1, that are involved in achieving this objective are described in the following.

In the event of a partial or complete shutdown, the power plant operators are informed to carry out a safe de-energisation of their power plant [9]. The most typical approaches, according to [9] of how to de-energise a power plant are as follows:

- **Trip**: The power plants are disconnected from the utility grid and thus no longer import or export any power.
- **Ramp down**: If a power plant is instructed to ramp down, it has to decrease its output power until no more power is exchanged with the utility grid.
- **Trip to house load:** In this case, a tripping sequence ensures that the power plant is disconnected from the utility grid, but ensures the supply of certain critical in-house loads that are necessary to run the generation unit itself.

Despite being de-energised, most generation units still require a power supply, whether for the emergency control of wind turbine rotor blades or to supply the cooling system of a thermal power plant. This is also crucial for maintaining the ability to provide restoration services at a later stage. [9], [15]

The black start phase is initialised by re-energising the power plant. However, to be able to provide black start services, the generation unit must possess, according to [9], the following three fundamental capabilities:

- Start up itself without being dependent on external power supplies.
- Energise a part of the network.

- Accept block loading of local demand.

In the following, two restoration strategies will be presented. Both rely on the *Bottom-up* approach for power system restoration based on non-traditional black start service providers shown in Figure 2.1.

Black Start from Distributed Energy Sources

The traditional restoration strategy in Great Britain relies on large synchronous generators that directly energise the skeleton of the transmission grid first and regulate load demand as shown in Figure 2.2. However, the Distributed Energy Resource (DER) based restoration strategy introduced in [9] aims to re-energise the network, i.e. passive components, and subsequently creates a microgrid at the distribution level that operates independently of the main utility grid. This is to be achieved through a coordinated process of different grid-forming units, which involves in the first step the re-energisation of GFL based generation units and in a subsequent step the restoration of a certain quantity of loads at once, i.e. block loading. The described process refers to *Stage 1* illustrated in Figure 2.2. [9], [16]

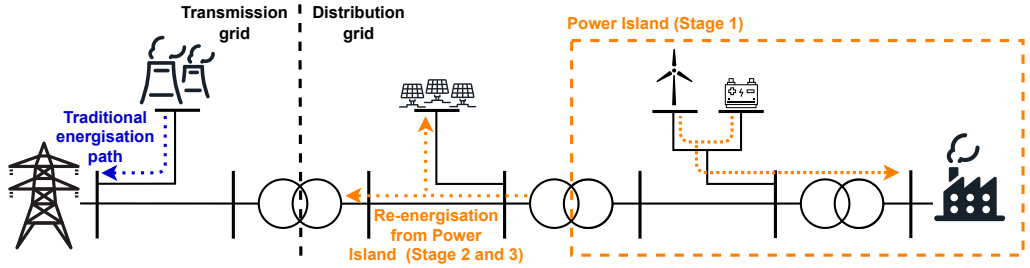

Figure 2.2: Development of microgrids, so-called power islands, for a DER based restoration strategy. Based on [16].

It should be noted that at *Stage 1*, the power island, which has an expected size between 1 MVA and 20 MVA, can either be synchronised with the transmission grid, in case this has already been restored, or the power island can be expanded by energising neighbouring parts of the distribution network (*Stage 2*), as shown in 2.2. In *Stage 3*, the generation units of the expanded power island could be pooled together to form a virtual power plant in order to energise parts of the transmission grid or synchronise with other power islands. However, reaching *Stage 2* and *Stage 3* is highly dependent on the available generation units and the existing critical loads that have to be supplied within the power island. [11], [16]

Black Start from Offshore Wind Power Plants

An alternative restoration approach based on a OWPP in combination with an energy storage system connected to the transmission system is presented in [17] and [18]. As for the DER-based restoration strategy, this approach follows the basic steps presented in Figure 2.1 and can be divided into three stages as shown in Figure 2.3 [17].

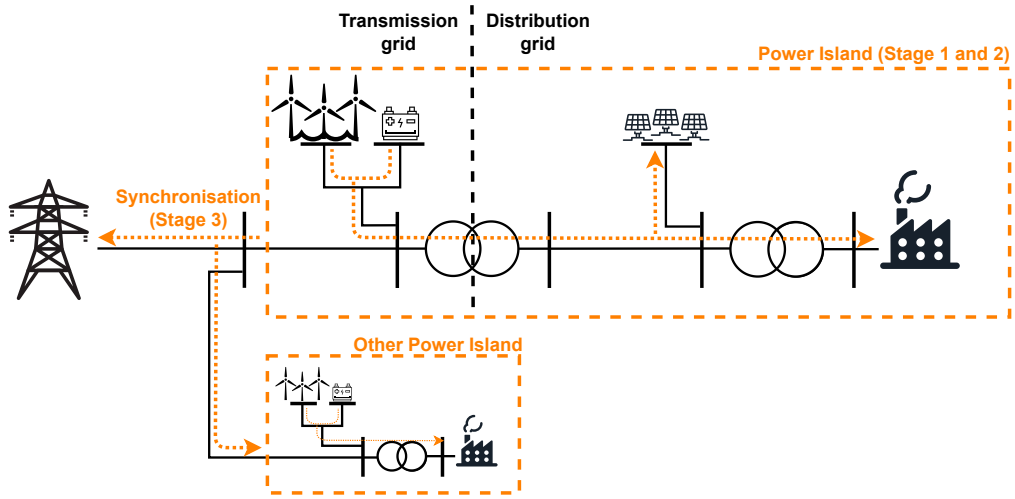

Figure 2.3: Development of power islands based on a restoration strategy using OWPP. Based on [17].

In the first stage, the OWPP system has to be energised, which includes primarily passive components such as cable connections, substations and the GFL based Wind Turbine (WT)s themselves. This process requires the availability of a black start-capable unit with GFM control, such as an energy storage system with reactive power capability. The objective of this phase is to operate the OWPP in islanded mode and to be able to keep its generation in balance with the system's internal load demand (*Stage 1*). After reaching a satisfactory stability level within the islanded OWPP system, *Stage 2* can start. This involves initially energising passive components of parts of the transmission and distribution grid, followed by block loading and possibly also the energisation of GFL based generation units at the distribution level. As for the restoration strategy based on DERs, the aim is again to create a power island. As this power island is still isolated, it has to be synchronised with other power islands in the final phase, *Stage 3*, to gradually restore a synchronous grid and complete the restoration process. [18]

2.1.2 Regulatory Requirements for Black Start

The TSOs in Great Britain (NGESO) and Belgium (ELIA) released black start requirements to include non-traditional black start providers. NGESO has therefore made regional tender zones as well as one supra-regional wind tender for its transmission system. The generation unit operators that fulfil the requirements listed in the tender can provide their service to NGESO. The requirements of ELIA are also split into tender zones but differ between the restoration of the 380kV "backbone" transmission system and the restoration of four underlying regional tender zones. Table 2.1 summarises the requirements from both TSOs [19], [20]. For NGESO only the wind tender is considered and for ELIA the underlying regional tender zones are considered.

Table 2.1: Black start requirements given by NGESO (wind tender) and ELIA (underlying regional tender) to connect non-traditional black start providers [19], [20].

	Requirements	
	National Grid ESO	**ELIA**
Self-start	Yes	Yes
Time to connect	$\leq$ 2 h	$\leq$ 1.5 - 3 h
Service availability	$\geq$ 80 %	Depending on provider
Voltage control	$\pm$ 10 % (for energisation and block loading process)	0s $\leq$ t < 2s: U$\geq$70% U_n; 2s $\leq$ t < 12s: U$\geq$85% U_n; 12s $\leq$ t: U$\geq$90% U_n (only block loading)
Frequency control (for block loading)	47.5 Hz - 52 Hz	47.5 Hz - 51.5 Hz
Black start service resilence of supply	$\geq$ 10 h	-
Black start auxiliary unit(s) resilence of supply	$\geq$ 72 h	$\geq$ 24 h
Block loading capability	$\geq$ 10 MW	$\geq$ 10 MW (with a cos $\varphi \geq 0.8$ inductive)
Reactive capability	$\geq$ 50 Mvar leading	$\geq$ 50 Mvar leading Depending on provider
Sequential start-ups	$\geq$ 3	$\geq$ 3
Short-circuit level (following the start of a system disturbance)	t $\leq$ 80ms: I$\geq\frac{240[MVA]}{\sqrt{3}\cdot U}$[kA]; t > 80ms: I$\geq\frac{100[MVA]}{\sqrt{3}\cdot U}$[kA]; U $\equiv$ connection voltage [kV]	-
Inertia value (stored energy)	$\geq$ 400 MVAs	-

Overall, both TSO demand a self-start within a defined time, after which the generation unit must be able to provide power to the Point of Common Coupling (PCC) and keep it upright for several hours. Further parameters that need to be controlled are voltage, frequency, short circuit level following a disturbance, and inertia provision. As it is not further specified in [19] and [20] whether the defined voltage limits refer to instantaneous or RMS values, the voltage limits are considered to be RMS values. This is also in accordance with the specified voltage limits in the grid code of NGESO [21].
Despite the changes and lowered requirements compared to earlier tenders [15], it is still a challenge for non-traditional black start service providers to meet the requirements. It is

unlikely that any single-generation unit fulfils all listed requirements. Therefore, NGESO and ELIA both allow aggregated generation units to fulfil the requirements. [14], [19], [20]

2.1.3 Challenges of Black Start

The transition to restoration strategies that rely on non-traditional black start service providers, as described in Section 2.1.1, poses new challenges of various natures. In [18], a summary of the technical challenges for OWPPs as black start service providers is given, which is the basis for this section.

- **Self-Start Capability:** At present, IBRs usually do not contribute to power system restoration as they are equipped with GFL converters and thus most of them are energised through their grid connection. Integrating black start capability into the IBRs is fundamental for providing sufficient and reliable black start service providers in the future. The implementation of GFM control topologies in combination with energy storage systems is therefore of great importance. [18]

- **Service Availability:** VREs like wind and solar power plants are weather-dependent and periods of little to no power supply occur. This limits the capacity and reliability of black start services. As NGESO and ELIA require high availability, and the output power of VRE fluctuates, VRE can only guarantee the requested black start service availability for a fraction of their nominal power. The implementation of energy storage systems can boost the service availability of VREs and increase the black start service capacity. [18], [22]

- **Inertia Provision:** Conventional power plants provide inertia support through the rotating mass of their synchronous generators. While some IBRs such as solar power have no inertia at all, others like wind power plants are often not designed to provide inertia. As an alternative to physical inertia, IBRs can provide virtual inertia. However, this requires IBRs controlled as a Virtual Synchronous Machine (VSM) and energy storage capabilities. Proving inertia support is crucial for slowing down Rate of Change of Frequency (RoCoF) in case of frequency disturbances through power imbalances. [18], [23]

- **Harmonic Performance:** The harmonic performance of a system depends on its components, such as power converters, cables and other passive elements. In addition, transformers draw transient inrush currents superimposed by harmonic components during the energisation process. This is due to the non-linear flux-current characteristics of the transformer. The magnitude and harmonic content of the magnetisation current depend on the switching time and the corresponding residual flux. According to [8], large inrush currents can occur especially during the energisation of large transformers in the transmission grid, where no soft-charging of passive components is possible. To avoid overloading the power converters through inrush currents, the controller should have current limiters. [8], [24], [25]

- **Transient Behaviour:** Transient behaviour through switching operations has to be taken into account in the energisation process, as the harmonic components might excite resonance, leading to resonant Temporary Overvoltage (TOV)s. This can be a challenge for the system, as these overvoltages can last for several periods and might exceed the normal operating voltage. This can trigger protective mechanisms or cause damage to the devices and in the worst case lead to the restoration process being aborted. [18], [25]
- **Control, Stability and Interoperability:** The use of aggregated generation units to fulfil the black start requirements complicates the energisation process and the operation of the power island in terms of controllability and interoperability. This is a demanding task as islanded systems are usually weak grids that jeopardise the stability of the system. Furthermore, the controller of a black start service provider needs to ensure a smooth transition from islanded operation to grid-connected operation to complete the restoration process. [16], [18]

2.2 Characteristics of Power Converters

Converters can generally be classified into GFL and GFM, based on their control scheme and operation in power grids. A simplified representation of GFL and GFM converters as controllable current or voltage sources is shown in Figure 2.4. [26], [27]

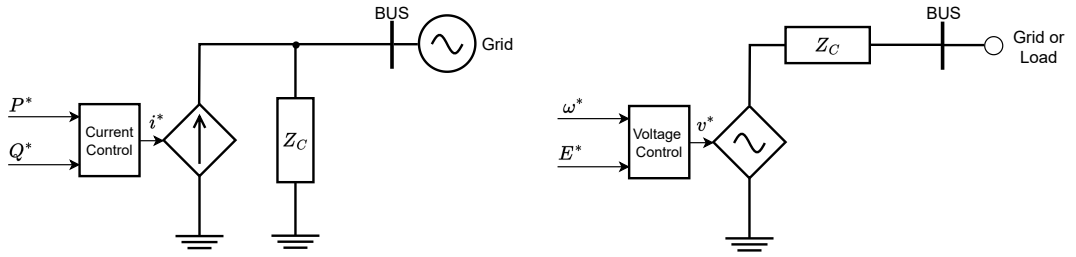

(a) Grid-following converter. **(b)** Grid-forming converter.

Figure 2.4: Simplified representation of power converters as controllable current or voltage sources. Note that Z_C represents a low output impedance for the GFM converter and a high parallel impedance for the GFL converter. Based on [26] and [27].

A GFL converter that injects the maximum available active power into the grid using Maximum Power Point Tracking (MPPT), while the reactive power is minimum, refers to a grid-feeding converter. Therefore this kind of GFL converter focuses on maximising the revenue of the IBR. However, due to the grid code specifications set by grid operators, especially large-scaled IBRs are obliged to support the grid in response to disturbances by adjusting their active and reactive power output. GFL converters operating in this mode refers also to a grid-supporting converter. Both modes maintain their active and reactive power reference values in the grid by regulating the output current as shown in Figure 2.4a. Due to their synchronization with the phase angle of the grid, which is achieved by tracking the grid voltage using a Phase-Locked Loop (PLL), at least one voltage source in the power grid is required that provides voltage and frequency reference. This results

in the key limitations of GFL converter, as they cannot be operated in islanded mode. Furthermore, due to their grid synchronization, unstable operation of the converter may occur in the event of voltage and frequency disturbances, especially in weak grids. [27], [28]
On the contrary, GFM converters have the ability to create and regulate the grid voltage as illustrated in Figure 2.4b and thus can either be the only generating unit in a system in islanded mode or be operated together with other GFL and/or GFM converters as well as with SGs in a grid-connected mode. If a GFM converter can be operated in parallel with other GFM-based IBRs and SGs, it is also referred to as a GFM grid-supporting converter [8]. Unlike GFL converters, some GFM do not require a PLL, as their self-synchronization is based on mimicking the principle of power-synchronization of SGs. However, the converter may become overloaded in stiff grids, as even a small deviation in the phase angle between the converter voltage and the grid voltage can lead to significant fluctuations in active power. [26], [27]
According to [27], the most prominent advantages and disadvantages of GFL and GFM converters can be summarised as follows:

Table 2.2: Comparison of GFL and GFM control. Based on [27].

Control Scheme	Advantages (+) and Disadvantages (−)
GFL	+ Quick regulation
	+ Simple control structure
	− Lack of frequency and voltage regulation
	− Unable to operate in islanded mode
	− Instability in weak grids
GFM	+ Able to operate in islanded mode
	+ Ability to regulate frequency and voltage
	− Instability in stiff grids
	− Easily susceptible to overload

2.2.1 Requirements for GFM Converters

Despite the researched characteristics on GFM converters as shown in Table 2.2 and their already established application in microgrids, there is to date no generally accepted definition of it [8]. However, a working group of the European Network of Transmission System Operators for Electricity (ENTSO-E) has proposed several capability requirements for IBRs with GFM control at European level in [29], which are listed below:

- Creating system voltage.
- Contributing to fault level.
- Contributing to system inertia.

- Supporting system survival to allow effective operation of *Load Frequency Demand Disconnection* for rare system splits.
- Prevent adverse control interactions.
- Acting as a sink to counter harmonics and unbalance in system voltage.

To meet the above requirements, the GFM must behave like a Thévenin equivalent circuit consisting of a voltage source in series connection with an impedance. This voltage source must be controllable in terms of magnitude and frequency to provide inertial support. This means that the voltage magnitude, frequency and phase angle must only change slowly during disturbance events, while at the same time allowing large and fast currents. Besides the first and fourth requirements listed above, which briefly address the support of restoration after a system collapse, this report also defines that GFM converters must generally be able to support the operation of the network during restoration without being dependent on SGs. [29]

2.2.2 Grid Forming Control for Black Start Services

As previously presented, GFM converters can create and regulate a voltage signal and can operate both in islanded and grid-connected mode, which are the key prerequisites for a black start service provider as shown in Section 2.1.2 and 2.1.3. Conversely, GFL converters are dependent on the synchronisation to an existing grid voltage signal and can therefore not be black starting units.

In [25], [30] and [31] investigations of various GFM control structures with black start capability are carried out. Based on the investigations of the aforementioned publications, this section briefly describes their five overlapping GFM topologies and compares their characteristic properties.

- **Droop-Based Control:** This control strategy aims to provide active and reactive power regulation based on Q-V and P-f droop control, which is complemented by a cascaded current and voltage control loop. The droop-based control strategy allows the operation of GFM converter both in islanded and grid-connection mode. Another advantage of this control method is the automatic power sharing between different IBRs to balance the power supply, which enables parallel operation with other generation units, without the necessity of fast and reliable communication, which can be difficult during a blackout. However, it should be noted that the droop-based approach can generally lead to steady-state errors. [25], [31]
- **Virtual Synchronous Machine:** The key element of this approach is the implementation of the swing equation to emulate the inertia provision of a SG. According to [23], three categories of VSM implementations can be distinguished based on their output reference, i.e. current, voltage and power reference. The actual implementation can be realised with different degrees of complexity up to high-order models.

The advantage of higher-order models is that the parameters can be set to emulate the characteristics of real SGs. These can be further adapted digitally depending on the application, without the physical constraints of a real SG. A disadvantage is that high-order models might lead to numerical instability. [23], [25]

- **Power-Synchronization Control:** The *Power-Synchronisation Control* was designed for HVDC applications in weak grids. It uses active power for grid synchronisation and calculates the phase angle by integrating the power difference, which differs from the *Virtual Synchronous Machine* approach using the swing equation. This leads to a comparatively higher stability margin. Further, to avoid overloading the converter a current limit has to be implemented. The disadvantage of the control structure is that without any modifications it provides no virtual inertia and damping as well as the necessity to have a PLL for applying current control in the event of faults in the grid and initial phase synchronisation. [25], [30]

- **Distributed PLL:** This control strategy [32] was developed for an OWPP that is connected to HVDC, that relies on a diode rectifier. The operating principle is based on the active power flow determining the d-axis voltage reference and the reactive power demand of the HVDC diode rectifier determining the frequency using Q-f-droop control. This approach differs from the conventional purpose of a PLL, as the reference voltage of the q-axis is not regulated to zero, but a frequency control loop is implemented to set the voltage reference for the q-axis. However, in [32] only limited findings are provided, as this control strategy was only used to perform a black start of the OWPP itself and its synchronisation with an already energised onshore grid, thus the effects of energising an export cable and the onshore converter were not investigated. [25], [30], [32]

- **Direct Power Control:** The *Direct Power Control* strategy was initially designed for Pulse Width Modulation (PWM) converters and is characterised by instantaneous active and reactive power control without the need for grid voltage measurements [33]. A modification to a GFM control structure is presented in [34], however, voltage measurements are required here, as it includes a PLL to perform reference frame transformations and to detect phase angle deviations when operating in island mode in the case of a system split. Furthermore, the estimated angular frequency of the PLL is used to perform P-f drop control for setting the active power reference to counter frequency deviations. This control structure has two outer control loops, an active and a reactive power control loop regulating the internal converter voltage and phase angle respectively. A characteristic of this modification is that it can cope with Short Circuit Ratio (SCR)s of less than 1.5. As a disadvantage missing electromechanical characteristics such as inertia emulation or damping can be identified. [25], [34]

The five GFM control strategies presented originate from various applications such as HVDC or OWPP and therefore possess distinct characteristics. However, they all show

potential black start capabilities according to [25]. A comparison of the advantages and disadvantages of the presented control strategies based on [25] is shown in Table 2.3.

Table 2.3: Comparison of GFM control strategies. Based on [25].

GFM Control Strategy	Advantages (+) and Disadvantages (−)
Droop based Control	+ Automatic power sharing − Steady-state errors might occur
Virtual Synchronous Machine	+ Virtual inertia and damping provision − High complexity and numerical instability for high-order models
Power-Synchronization Control	+ Developed for applications in weak grids − Lack of virtual inertia and damping
Distributed PLL	+ Autonomous frequency control and automatic synchronization techniques − The research is limited to the synchronisation to an energised grid.
Direct Power Control	+ Able to work in grids with low SCRs − Lack of virtual inertia and damping

2.3 Summary

In this chapter, restoration strategies with non-traditional black start service providers and the associated challenges were introduced. Moreover, relevant black start requirements given by the TSOs of Great Britain and Belgium were described. Finally, the characteristics of GFL and GFM converters were highlighted and a review of potential GFM control topologies for black start purposes was presented.

3 Problem Statement

Based on the findings in the Introduction and the State of the Art, it will be important to investigate the impact and feasibility of new black start service providers as traditional ones are phased out to reach dedicated climate goals. This leads to a number of challenges, e.g. in terms of self-start capability, service availability, but also control capability, to maintain the same level of reliability as traditional black-start service providers. In [24], a study is conducted, confirming the usability of a STATCOM with an integrated battery energy storage system for black start services. It is argued that the fast and dynamic reactive power response of the STATCOM along with the battery unit and its ability for bidirectional active power flow can provide inertial, frequency and voltage regulation that fulfil the black start requirements given by the British TSO [24]. This master's thesis uses the investigations made in paper [24] as proof of concept for this technology and as an argument for further research, which leads to the following problem statement:

> *Can a STATCOM with an integrated battery energy storage system (STATCOM-BESS) with grid-forming control structure be used to energise a transmission system and subsequently a distribution system while complying with the black start requirements specified by the Belgian and British TSOs?*

Objective

The main objective of this project is to build a GFM controller with black start capability for the *STATCOM-BESS* and to evaluate its performance and impact on the system when energising an islanded system. The focus is initially the energisation of transformers and an overhead line at the transmission level and subsequently creating a power island with load and generation units connected to the distribution level. This process refers to *Stage 2* shown in Figure 3.1.

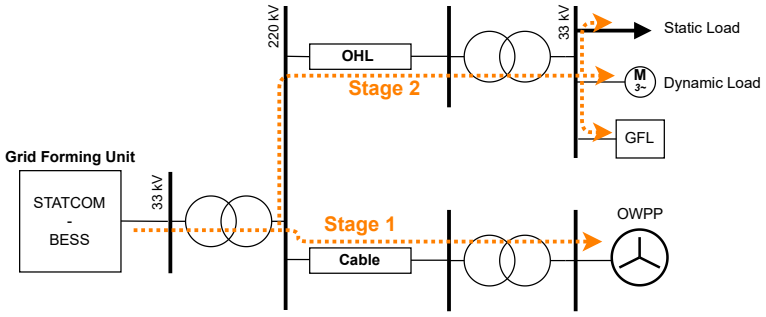

Figure 3.1: Basic schematic representation of the system considered in this project.

The stages for the energisation process shown in this figure refer to Section 2.1.1 and its part *Black Start from Offshore Wind Power Plant*. It is therefore assumed that the *STATCOM-BESS* is located at an onshore substation of a OWPP network connected to the transmission grid. It is to be noted that *Stage 1* shown in 3.1, the energisation of the OWPP, and *Stage 3*, the synchronisation with other power islands, will not be considered in this project. Therefore, this project considers the following objectives:

- Build a system model in PSCAD consisting of a *STATCOM-BESS* as GFM unit, two transformers, an overhead line, a GFL unit as well as static and dynamic loads.
- Build a GFM controller for the *STATCOM-BESS* and the GFL controller for the generation unit connected to the distribution level in PSCAD. The GFM controller shall have black start capability.
- Energise the modelled transmission system including an overhead line and transformers and investigate the system response and the developed GFM controller.
- Perform block loading of static and dynamic loads at the distribution level to create a power island. Moreover, the performance of the *STATCOM-BESS* and the GFL unit as aggregated units during the block loading is to be analysed.

Sucess criteria

The success criteria for the restoration process and thus for the development of the controllers is to fulfil the following requirements during the energisation process:

- Independent self-start of the GFM unit.
- Maintain RMS voltage and frequency limits during the energisation process including block loading.
- Comply with the current limits of the controllers at any time.

The first two requirements refer to the released specifications of the Belgian and British TSOs, given in Table 2.1, while the current limits will be defined in the corresponding modelling sections of the controllers.

3.1 Limitations

The project excludes the following topics and makes the following assumptions due to time constraints, relevance or complexity:

- **Constant DC Link voltage:** Battery dynamics, state of charge, and potential weather dependencies are neglected. Therefore an ideal DC-link voltage is assumed for the *STATCOM-BESS* and GFL model.
- **Circuit Breakers:** No single pole operations of the circuit breakers are considered in this project, meaning all phases are switched simultaneously.

- **Protection:** Protective devices, that would lead to disconnection of generation unit or other power system components during disturbances are not implemented or investigated in this project.
- **PWM Signal:** The control of the switching devices generating a PWM signal at the inverter output is excluded from this project. Instead, average models are used for the GFM and GFL units, allowing a direct conversion from the dq to the abc reference frame to generate the three-phase voltage signal at the output.
- **OWPP Network**: The OWPP network, connected to the onshore substation where the *STATCOM-BESS* is located, is not part of this project. This decision was made at an earlier stage of the project to focus on the control of *STATCOM-BESS* and the energisation of the transmission as well as the distribution system.

3.2 Structure

The content of the project is structured into the following chapters:

- **Chapter 1:** The first chapter emphasises the necessity of investigating new restoration strategies and new potential providers of black start services.
- **Chapter 2:** The state-of-the-art chapter describes the restoration strategy based on non-traditional black start service providers. In addition, the challenges and requirements associated with the restoration process are described. Emphasis is also put on the characteristics of GFL and in particular GFM control topologies.
- **Chapter 3:** In this chapter, the problem statement is presented, including the objectives, success criteria and limitations of the project.
- **Chapter 4:** This chapter will contain the modelling of the system in PSCAD and the corresponding GFM control scheme of the *STATCOM-BESS*. Subsequently, the response of the *STATCOM-BESS* to a sudden load change will be tested.
- **Chapter 5:** In this chapter, the modelled transmission system will be energised initially with an ideal voltage source and later with the *STATCOM-BESS* as the black start service provider. The response of the system and controller during the black start will be analysed.
- **Chapter 6:** In this chapter, the modelling of the distribution system including the the dynamic load and the GFL unit will be described. After this, the block loading with static and dynamic load models at the distribution level will be performed aiming to establish a power island. The performance of the *STATCOM-BESS* and the GFL unit as aggregated units during block loading will be analysed.
- **Chapter 7, 8 & 9:** In the final chapter, an overall conclusion is drawn based on the results of the black start investigations and relevant findings will be discussed. Possible future work and improvements for the continuation of this project will be presented.

4 System and Controller Modelling

This chapter describes the modelling of the system in PSCAD and the corresponding GFM control scheme of the *STATCOM-BESS*. Initially, the components of the system are briefly described, followed by transformer saturation modelling in PSCAD. Afterwards, the implementation and the characteristics of the individual control loops of the GFM controller are presented. Finally, the response of the *STATCOM-BESS* to a sudden load change is evaluated through a step response test, to ensure that the built GFM controller works satisfactorily.

4.1 System Description

As described in Chapter 3, a *STATCOM-BESS* is considered to be the black start service provider in this project and is assumed to be located at an onshore substation of an OWPP. Figure 4.1 shows the single-line diagram of the system built in PSCAD.

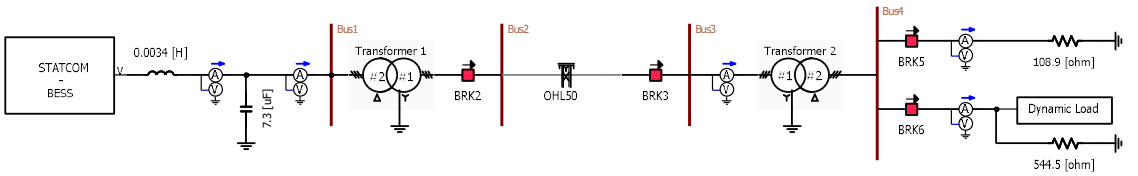

Figure 4.1: Single line diagram of the modelled system in PSCAD.

The components of the system include a *STATCOM-BESS* with an LC filter at *Bus1*, two transformers and an overhead line between *Bus2* and *Bus3*. The static and dynamic load model shown connected to *Bus4* will be discussed in Chapter 6.
The *STATCOM-BESS* has a rated power of $50\,\mathrm{Mvar}$ and $10\,\mathrm{MW}$, following the minimum requirements given in Table 2.1. The LC filter of the *STATCOM-BESS* consists of a series reactor and a shunt capacitor. The reactance of the series reactor L_f is $0.0034\,\mathrm{H}$, which corresponds to $0.05\,\mathrm{pu}$ of the base impedance Z_{Base} as shown in the following: [24], [35].

$$Z_{Base} = \frac{V_{n,SB}^2}{S_{n,SB}} \rightarrow L_f = \frac{0.05 \cdot Z_{Base}}{2\pi \cdot f} \tag{4.1}$$

Here the parameters $V_{n,SB}$ and $S_{n,SB}$ are the nominal voltage and the nominal apparent power of the *STATCOM-BESS* respectively. The shunt capacitor C_f has a twofold function, namely the provision of reactive power and the filtering of harmonic components in

combination with the series reactor by providing a low-impedance path to the ground. The capacitance of the filter C_f is set to 7.3 µF and is determined following [35]:

$$C_{Base} = \frac{1}{2\pi \cdot f \cdot Z_{Base}} \rightarrow C_f = 0.05 \cdot C_{Base} \tag{4.2}$$

The *STATCOM-BESS* including its LC filter is connected to the transmission system by a $33kV/220kV$ step-up transformer. For the $50\,\mathrm{km}$ long overhead line between *Bus2* and *Bus3*, the *Frequency-dependent (phase) model* is used to accurately reflect the frequency behaviour of the line [36]. The parameters of the line model are based on [37]. A $220kV/33kV$ step-down transformer connects *Bus3* with *Bus4*, where a static and dynamic motor load is connected to the system at *Bus4*. Further description for the load modelling will be covered in Chapter 6.

An overview of the parameters of the line model can be found in Figure A.1, while the ratings for the *STATCOM-BESS* including filter are given in Table A.1 in Appendix A.

Transformer Saturation Modeling
In PSCAD a basic saturation characteristic of a transformer is defined by using three parameters: Air Core Reactance, magnetising current I_m at nominal voltage V_n and knee voltage V_k. Note that the saturation curve asymptotically approaches the line formed by the knee point and the the air reactance. [38]
The resulting saturation curve describing the relation between magnetic flux λ and magnetisation current I_m given by PSCAD [39] can be seen in Figure 4.2.

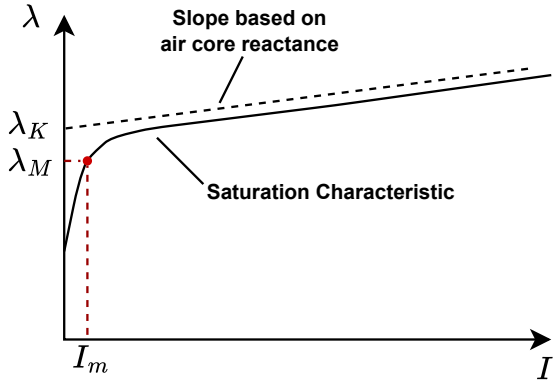

Figure 4.2: Core saturation characteristics of the transformer model in PSCAD. Based on [39].

In Figure 4.2, the steady-state operation range at rated conditions is seen as the range below the red dotted line [39]. The knee point K of the saturation curve is defined in per unit of the nominal operation point and is typically in the range of $1.15\,\mathrm{pu}$ to $1.25\,\mathrm{pu}$ [39]. The relation between magnetic flux and voltage in the linear range is described in the following Equation [39].

$$\lambda = \int V_L(t) \cdot dt \tag{4.3}$$

Here λ is the magnetic flux, V_L is the winding voltage and t is the time between zero crossings. The relation of the knee point of the flux λ_K and the peak magnetic flux λ_M at nominal operation conditions is defined in the following equation [39].

$$\lambda_K = K \cdot \lambda_M \tag{4.4}$$

These considerations are used in the PSCAD model for this project and built the foundation of the transformer model. The parameters of the transformer model are based on [37] and can be found in Table A.2 in Appendix A. Furthermore, a theoretical description of the transformer saturation can also be found in also in Appendix A.

4.2 GFM Controller Description

The GFM control structure considered in this project refers to a VSM control and is based on [40]. The choice of VSM was made due to its specific ability to provide virtual inertia and being able to operate in islanded mode [40], [41]. The frequency characteristic of the VSM is based on the principle of power synchronization by emulating the dynamics of the swing equation, which is the basis for the determination of the phase angle θ used for all dq-abc and abc-dq transformations [41]. Therefore the VSM does not rely on grid synchronization methods using PLLs. The reference for the voltage amplitude is adjusted by a Q-V droop controller. The cascaded control loops of the VSM can be seen in Figure 4.3, where a distinction is made between power, current and voltage control loop [40].

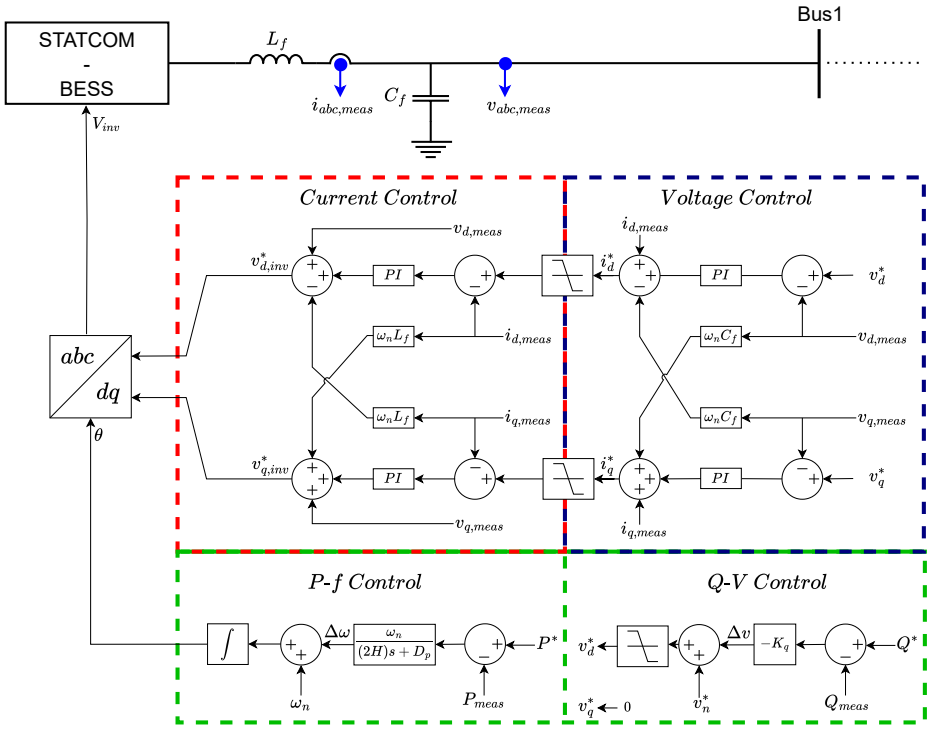

Figure 4.3: Average model of the VSM based GFM control structure used in the *STATCOM-BESS*. Based on [40].

The input signals $v_{d,meas}$, $v_{q,meas}$, $i_{d,meas}$ and $i_{q,meas}$ of the control structure are based on the measured voltage and current signals $i_{abc,meas}$ and $v_{abc,meas}$. The measured signals are converted into the dq-reference frame, and fed into the voltage and current control loop. The active power P_{meas} and reactive power Q_{meas} supplied by the *STATCOM-BESS* and used in the outer power loops can be described as follows [42]:

$$P_{meas} = v_{d,meas} \cdot i_{d,meas} + v_{q,meas} \cdot i_{q,meas} \approx v_{d,meas} \cdot i_{d,meas} \tag{4.5}$$

$$Q_{meas} = -v_{d,meas} \cdot i_{q,meas} + v_{q,meas} \cdot i_{d,meas} \approx -v_{d,meas} \cdot i_{q,meas} \tag{4.6}$$

In Eq. (4.5) and (4.6) it can also be seen that setting the reference v_q^* to zero as shown in Figure 4.3 leads to a simplification of the P_{meas} and Q_{meas} relations in steady state.

The modelling and characteristics of each control loop are further explained in the following sections:

- **Section 4.2.1**: This section describes the implementation and behaviour of the P-f control loop that determines the phase angle θ by mimicking the inertial behaviour of a SG.
- **Section 4.2.2**: In this section the Q-V droop control which adjusts the reference for the voltage amplitude is described.
- **Section 4.2.3**: This section includes a description of the basic functionality and the tuning process of the current and voltage control loop.
- **Section 4.2.4**: In this section the response of the *STATCOM-BESS* to a sudden load change of $10\,\mathrm{MW}$ is analysed to validate the determined control parameters.

4.2.1 P-f Control

An important part of power systems is the stored kinetic energy in the rotating mass of the SG, to balance fluctuation between generation and load demand. Under balanced conditions, the rotating mass runs with nominal frequency and through its inertia, it behaves as a storage of potential energy. This leads to its ability to resist changes in rotational speed and therefore changes in frequency. The behaviour of the rotor speed and therefore the grid frequency to imbalances in power can be described through the following swing equation according to [43].

$$J\omega_m \frac{d^2\theta_m}{dt^2} = P_m - P_e \tag{4.7}$$

Here ω_m is the mechanical angular frequency of the rotor, J is the moment of inertia of the rotating mass, θ_m is the mechanical angle of the rotor, and P_m and P_e are mechanical and electrical power acting on the rotor.
The higher the moment of inertia and the angular frequency, the more kinetic energy E_{kin} is stored in the rotating mass, which is described as *Inertia Value* by NGESO in Table 2.1 and has to be at least $400\,\mathrm{MVAs}$. For a SG, the inertia constant H describes for how many

seconds the rated power of the machine S_r can be drawn from the stored kinetic energy in the rotating mass until the machine would stand still. This can be described through the following equation [44].

$$H = \frac{E_{kin}}{S_r} = \frac{J\omega_m^2}{2S_r} \tag{4.8}$$

With IBR not having a rotating mass, the P-f control of the VSM fulfils the function of emulating the frequency characteristic of a rotating mass of a SG and behaves as a first-order Low-Pass Filter (LPF), according to the transfer function given in the following equation [40].

$$G(s) = \frac{\omega_n}{(2 \cdot H)s + D_p} \tag{4.9}$$

Here H represents the inertia constant in seconds, which slows down the change in frequency. D_p is the damping constant, and ω_n represents the nominal angular frequency [40]. Note that $2 \cdot H$ is here defined according to [45] as the moment of inertia J.
NGESO and ELIA do not state a minimum inertia constant in their requirements, but in NGESOs grid code, it is given that the inertia constant H can be calculated using the equation below [21].

$$H = \frac{Inertia\ Value\ [MVA]}{Rated\ Machine\ Power\ [MVA]} \tag{4.10}$$

With an *Inertia Value* of $400\,\mathrm{MVAs}$ and a rated machine power of $51\,\mathrm{MVA}$, this leads to an inertia constant of $7.8\,\mathrm{s}$.
To calculate the damping constant D_p from the transfer function given in Eq. (4.9), it was chosen that a change in active power output of $100\,\%$ of the *STATCOM-BESS*, which equals $0.196\,\mathrm{pu}$ of the apparent power, should lead to a change in frequency of $5\,\%$ [21]. This corresponds to a change of $1\,\mathrm{Hz}$ per $4\,\mathrm{MW}$ active power output of the *STATCOM-BESS* and results in a droop constant of $R = 0.255$. Its reciprocal value is the damping constant D_p, which is calculated through the following Equation and leads to a damping constant of $D_p = 3.92$ [45]:

$$D_p = \frac{1}{R} \tag{4.11}$$

The behaviour of the implemented P-f control can be seen in Figure 4.4, which shows the correlation of the difference between P_{meas} and P^* and the corresponding controller output frequency.

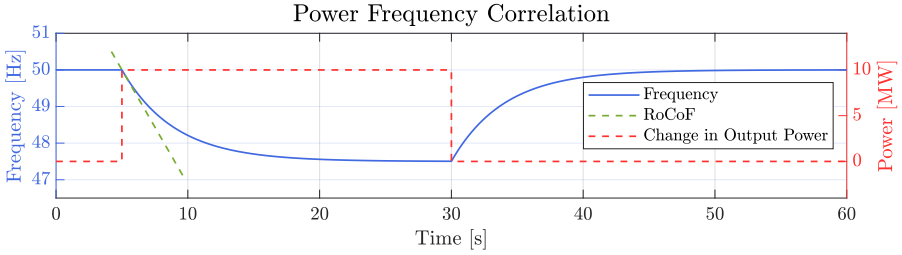

Figure 4.4: Behaviour of the frequency under change of active power as described in Eq. (4.9). The active power of $10\,\mathrm{MW}$ represents $0.196\,\mathrm{pu}$ of the total apparent power output of the *STATCOM-BESS*.

The P-f control sets an output frequency of $50\,\mathrm{Hz}$ when P_{meas} equals P^*. At $5\,\mathrm{s}$, a load of $10\,\mathrm{MW}$ is connected, leading to a drop in frequency down to $47.5\,\mathrm{Hz}$. In the initial moment, the speed of the frequency drop is limited by the inertia constant, while afterwards the damping constant limits the frequency to $47.5\,\mathrm{Hz}$. The highest occurring RoCoF is $0.625\,\mathrm{Hz/s}$, which is below the maximum RoCoF of $1\,\mathrm{Hz/s}$, as specified by NGESO [21]. When reducing the load at 30 seconds, the frequency increases again to its initial state of $50\,\mathrm{Hz}$.

4.2.2 Q-V Droop Control

For adjusting the voltage reference of the *STATCOM-BESS*, a Q-V droop control is implemented in the VSM control structure. The Q-V control is based on the following equation [40].

$$v_d^* = v_n^* - K_q(Q^* - Q_{meas}) \tag{4.12}$$

The output value v_d^* of the Q-V droop control is defined through the nominal output voltage v_n^* and Δv that is adjusted through the droop constant K_q and the difference between setpoint Q^* and the measured reactive power Q_{meas}. The droop is calculated to be $K_q = 0.051$, leading to an $5\,\%$ change in v_n^* per $50\,\mathrm{Mvar}$ change in the reactive power output of the *STATCOM-BESS*. The output of the Q-V droop control is limited to an output value between $0.95\,\mathrm{pu}$ to $1.05\,\mathrm{pu}$, to ensure that the RMS voltage limits of $\pm 10\,\%$ around the nominal voltage given by NGESO are fulfilled.
In steady state with an inductive load, the *STATCOM-BESS* provides reactive power and therefore increases v_n^*. When connecting a capacitive load, the *STATCOM-BESS* absorb reactive power and the setpoint v_n^* decreases.

4.2.3 Voltage and Current Control Loop

The cascaded voltage and current control loop shown in Figure 4.3 form the two inner control loops of the outer power loops. Both inner control loops are based on PI controllers and consist of decoupling terms for independent control of their d- and q-components [46]. While the voltage control loop aims to maintain the set reference values v_d^* and v_q^*, it defines the current references i_d^* and i_q^* for the current control loop. The following current control loop adjusts the output voltage of the *STATCOM-BESS* accordingly to meet the power demand set by the loads of the islanded system.
Moreover, current limits are implemented for i_d^* and i_q^* to ensure that the physical limits of the *STATCOM-BESS* are not violated due to overcurrent. Based on [47] inverters are typically designed for a maximum total current between $1\,\mathrm{pu}$ and $1.2\,\mathrm{pu}$ of their nominal current. Therefore, the current limits are set to $\pm 0.22\,\mathrm{pu}$ for i_d^* and $\pm 1.08\,\mathrm{pu}$ for i_q^*, corresponding to a maximum total current of $1.1\,\mathrm{pu}$.
Furthermore, it is constantly monitored whether the specified current limits are exceeded in order to freeze the output of the PI controller in the voltage control loop. This is done to prevent the output of the PI controller from rising uncontrollably when the current

references reach their specified limit, which improves the overall stability of the GFM controller.

Tuning Voltage and Current Control Loop

Following the design and implementation of the P-f and Q-V power control loops in the previous section, the control parameters for the voltage and current control loops need to be determined in order to provide a fast and accurate response while maintaining the stability of the controller. The tuning of the control parameters in MATLAB is initially based on the basic structure of the voltage and current control loop illustrated in Figure 4.5.

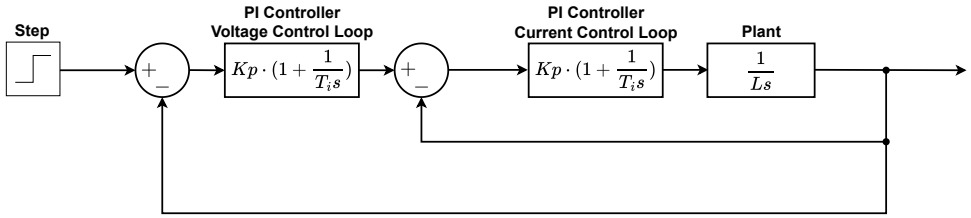

Figure 4.5: Simplified structure of the cascaded voltage and current control loop for the tuning process in MATLAB.

Both control loops consist of a PI controller, whereby the voltage controller represents the outer control loop of the current controller and thus forms a cascaded control scheme. For the current control loop, the series reactor L_f of the LC filter acts as the plant with a value of $0.159 \times 10^{-3}\,\mathrm{pu}$ at $50\,\mathrm{Hz}$ based on the design criteria given in Section 4.1. The plant for the voltage controller is formed by the closed current control loop.

As the focus of the current control loop is on fast and accurate response, the design criteria for the current control loop are a bandwidth of around $500\,\mathrm{Hz}$, a phase margin of $\geq 45^\circ$ and a maximum overshoot of $5\,\%$ [48]–[50]. The dynamics of the voltage control loop should be about ten times slower than those of the current control loop. This is done to decouple the two control loops and avoid inferences between them [48].
However, during the initial testing of control parameters in the PSCAD model by applying a sudden load change of $10\,\mathrm{MW}$ to the *STATCOM-BESS*, the GFM controller response showed severe oscillations and instabilities. This occurred despite prior assessment of the control parameters in MATLAB with a step response test using the simplified structure shown in Figure 4.5. It was found on an experimental basis in PSCAD that to overcome these problems and maintain a stable operation of the controller, the response of the voltage control loop had to be slowed down significantly, resulting in a response approximately 1000 times slower than the current control loop. The selected control parameters for the PI controllers for the current and voltage control loops are a compromise between low overshoot and fast response of the controller when applying the aforementioned sudden load change in PSCAD. Table 4.1 provides an overview of the control parameters K_P and T_i including the bandwidth BW of both control loops.

Table 4.1: Control parameters for the PI controllers including the bandwidth BW of both control loops.

	K_p	T_i	BW
Voltage Control Loop	0.375	0.1	0.47 Hz
Current Control Loop	0.5	0.05	502 Hz

When applying a step at the input of the control scheme shown in Figure 4.5 with the control parameters specified in Table 4.1, the following step response can be observed in MATLAB:

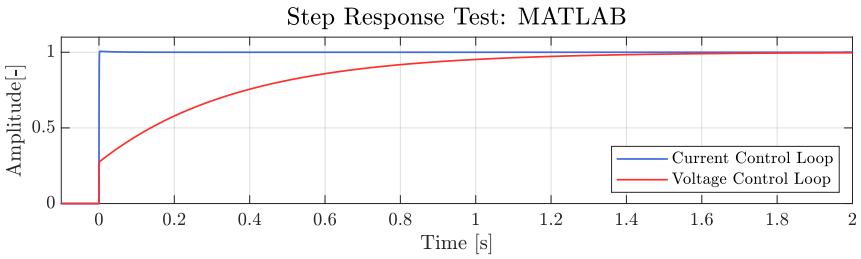

Figure 4.6: Step response in MATLAB of the voltage and current control loop.

Here the significantly lower response time of the voltage control loop compared to the current control loop can be observed. In detail, the voltage control loop has a settling time of $1.27\,\mathrm{s}$ and an overshoot of zero, while the current control loop has a settling time of $0.0013\,\mathrm{s}$ and an overshoot of $0.6\,\%$. Overall, it can be seen that both control loops show stable responses, with the current control loop fulfilling the defined requirements. The response of the voltage shows that the requirement to be around ten times slower than the current control loop is far from being met.

4.2.4 Step Response Test in PSCAD

As aforementioned, the control parameters shown in Table 4.1 were mostly determined by observing the response of the GFM controller to a sudden load change. A load change of $10\,\mathrm{MW}$ was applied on the *STATCOM-BESS* including the LC filter in PSCAD. For the test, the voltage is ramped up from $0\,\mathrm{pu}$ to $1\,\mathrm{pu}$ in $0.3\,\mathrm{s}$. Afterwards, a resistive load with $108.9\,\Omega$, corresponding to $10\,\mathrm{MW}$, is connected to *Bus1* at $0.4\,\mathrm{s}$ instead of the system shown in Figure 4.1. The load is then disconnected at $0.6\,\mathrm{s}$. The corresponding phase voltage v_{meas}, the voltage magnitude $|v_{meas}|$, the voltage reference v_d^* of the GFM controller, the power demand of the islanded system and the frequency of the *STATCOM-BESS* during the test period are shown in Figure 4.7.

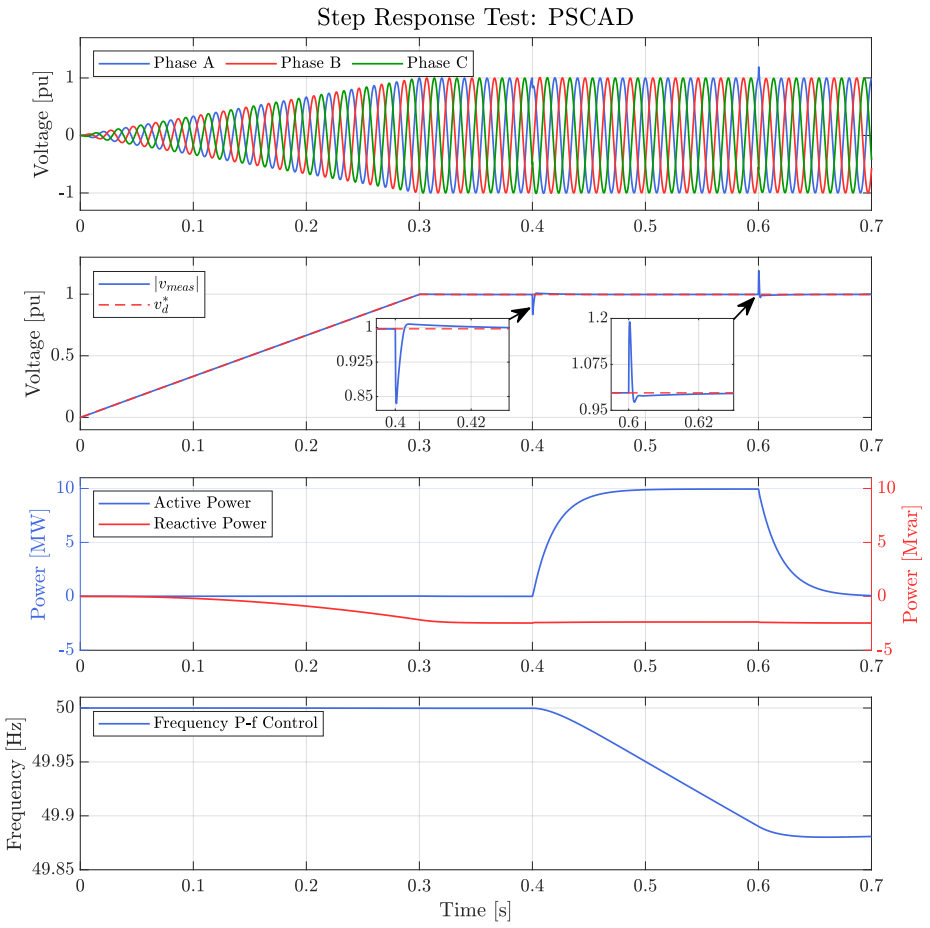

Figure 4.7: Response of the phase voltage v_{meas}, the voltage magnitude $|v_{meas}|$, the voltage reference v_d^* of the GFM controller, the power demand of the islanded system and the frequency of the *STATCOM-BESS* during the test period. Note that $1\,\mathrm{pu}$ correspond to a phase voltages with $U_{peak} = 26.9\,\mathrm{kV}$ and that the voltage magnitude is calculated using the α-β reference frame: $|v_{meas}| = \sqrt{v_\alpha^2 + v_\beta^2}$.

The first two subfigures show that the controller can satisfactorily follow its voltage set-point defined by v_d^* and thus can precisely control the voltage v_{meas} during the voltage ramp-up. To validate the accuracy of the implemented Q-V droop control, Eq. (4.12) is applied at $0.39\,\mathrm{s}$ with Q_{meas} being $-2.473\,\mathrm{Mvar}$, Q^* being $0\,\mathrm{Mvar}$ and v_n^* being $1\,\mathrm{pu}$, resulting in a v_d^* of $0.9975\,\mathrm{pu}$. This corresponds precisely to the actual value for v_d^* present in the second subfigure of Figure 4.7.
When the resistive load is connected at $0.4\,\mathrm{s}$, the voltage magnitude $|v_{meas}|$ shows a dip to around $0.83\,\mathrm{pu}$. However, the controller of the *STATCOM-BESS* responds in a stable manner to the disturbance by regulating the voltage v_{meas} back to a steady state within $4.1\,\mathrm{ms}$, considering a tolerance band of $1\,\%$. When the load is disconnected, the voltage magnitude $|v_{meas}|$ shows a peak of about $1.19\,\mathrm{pu}$ and reaches a steady state after $2.5\,\mathrm{ms}$. The seen voltage transients, mainly occurring in Phase A, are within the tolerable range according to the RMS voltage limits given by NGESO in Table 2.1, as shown in Figure 4.8.

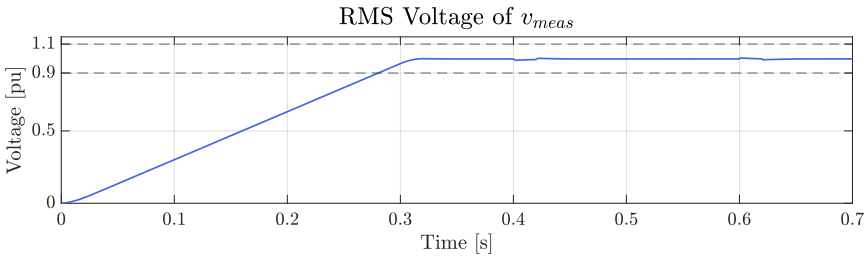

Figure 4.8: Response of the the line-to-line RMS value of v_{meas} during the test period. Note that $1\,\mathrm{pu}$ correspond to a line-line RMS voltage of $33\,\mathrm{kV}$. The RMS value is calculated digitally in PSCAD for each simulation time step with an observation window of $20\,\mathrm{ms}$.

The third subplot in Figure 4.7 shows that the *STATCOM-BESS* is able to meet the active and reactive power demand of the islanded system, which is determined by the connected resistive load and the passive components of the filter. Note that the rise and decay of active and reactive power are slowed down by the smoothing time constant of $0.02\,\mathrm{s}$, used for power measurement in PSCAD.
The last subplot shows that the generated frequency of the P-f control decreases slowly from $0.4\,\mathrm{s}$ as intended due to the positive difference between P_{meas} and P^*. It reaches a minimum of $49.88\,\mathrm{Hz}$ after $0.66\,\mathrm{s}$ and starts rising again due to disconnection of the load. The reason for the delayed minima after the disconnection of the load is that measured active power does not decrease immediately to zero, due to the smoothing time constant of the power measurement. The comparatively small frequency drop is due to the short time duration of $0.2\,\mathrm{s}$ in which the load of $10\,\mathrm{MW}$ is connected, as well as the inert frequency response through the implemented transfer function specified in Eq. (4.9) as shown in Section 4.2.1.

4.3 Summary

In this chapter, the system model has been introduced and the corresponding control loops of the VSM control scheme were highlighted. The overall performance of the GFM controller and the determined control parameters were tested by simulating a step response test in the form of sudden load changes. From this, satisfactory results were obtained, leading to the conclusion that the controller works as intended.

5 Analysis I: Transmission System Energisation

In this chapter, the behaviour during the energisation of the transmission system till *Bus4* will be analysed. The simulations are done in PSCAD with a time step of $100\,\mu s$ and are the basis for analysing the response of the transmission system and the corresponding black start service provider during the energisation of the system. The chapter is therefore structured as follows:

- **Section 5.1:** This section focuses on the energisation of the transmission system till *Bus4*, where an ideal voltage source provides a rigid output voltage before the series reactor L_f. The current drawn by the passive components such as the filter, overhead line and transformers are investigated by connecting them one by one. Different mitigation techniques are tested to reduce disturbances during the black start process.
- **Section 5.2:** This section focuses on investigating the origin of the disturbances during black start by measuring at different points of the transmission grid. It follows the energisation procedure and mitigation techniques introduced in Section 5.1.
- **Section 5.3:** In this section, the energisation of the transmission system till *Bus4* will be carried out with the GFM based *STATCOM-BESS* as black start service provider. The system and controller responses during the energisation process will be analysed.

5.1 Initial Black Start Investigations with Voltage Source

In the following section, a constant voltage source is used to represent the *STATCOM-BESS* in simplified form, to assess the response of the individual passive components to the energisation process. The results are presented in the following from the perspective of the black start service provider.

Energisation Filter and Transformer 1
In the first step, the system shown in Figure 4.1 is energised up to *BRK2*, including the LC filter and *Transformer 1*, by using the soft-charging technique. This is done by slowly increasing the voltage from $0\,\mathrm{pu}$ to $1\,\mathrm{pu}$ using a GFM inverter or, as in this case, a voltage

source [8]. Soft charging has the distinct advantage of being able to limit the transient inrush currents during the energisation process [17]. The system energisation for the LC filter and *Transformer 1* is considered to be a legitimate procedure as this part of the system is commonly energised in *Stage 1*, see Section 2.1.1, along with the passive components of the OWPP system. However, soft-charging is only applicable for the first energisation stage and can not be repeated for the following stages, as parts of the system are already in operation at this point. For the implementation of soft-charging in this project, three different voltage ramp-up times are tested in Figure 5.1 to evaluate their influence on the magnetizing current of *Transformer 1* and consequently the transient inrush current in the system.

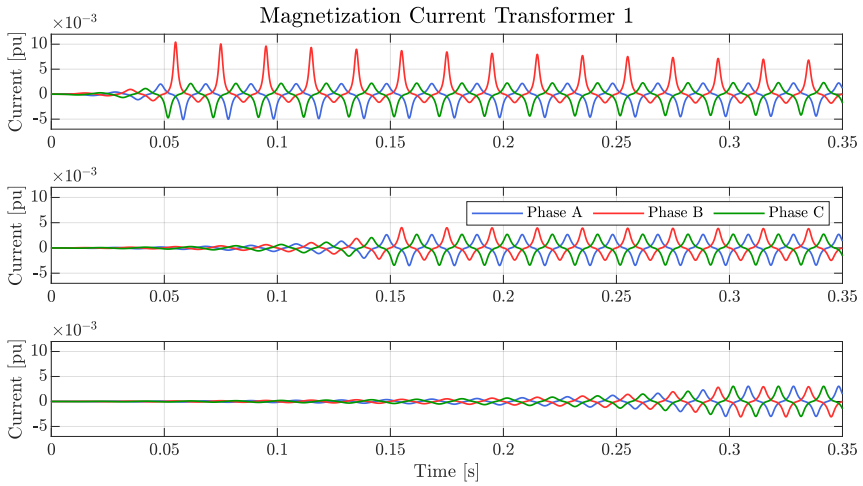

Figure 5.1: Magnetisation currents of *Transformer 1* with different voltage ramp-up time applied on the voltage source: $0.05\,\mathrm{s}$, $0.15\,\mathrm{s}$ and $0.3\,\mathrm{s}$. It should be noted that the voltage ramp-up times are defined by their duration to increase from $0\,\mathrm{pu}$ to $1\,\mathrm{pu}$ voltage. Note also that $1\,\mathrm{pu}$ corresponds to the nominal phase current of $1.262\,\mathrm{kA}$ and that the polarity of the magnetisation current is changed to match with Figure 5.2, as PSCAD measures magnetisation current in the transformer model with different polarity.

Overall, it can be seen that all applied voltage ramp-up times lead to comparatively low magnetisation currents since according to [51], these can reach a multiple of the nominal magnetisation current of a transformer. The upper subfigure shows that a voltage ramp-up time of $0.05\,\mathrm{s}$ still leads to a saturation of *Transformer 1*. This results in a maximum magnetising current of about $0.01\,\mathrm{pu}$ in Phase B and asymmetries in all phases that decay over time. A lower magnetising current can be achieved with a voltage ramp-up time of $0.15\,\mathrm{s}$, as shown in the middle subfigure. However, asymmetries are still present in all phases with a maximum value of about $0.004\,\mathrm{pu}$ in Phase B. In the bottom subfigure, with a voltage ramp-up time of $0.3\,\mathrm{s}$, no severe asymmetries can be observed and the current peak only reaches about $0.003\,\mathrm{pu}$. The overall current waveform corresponds to a minimum to no saturation of *Transformer 1* [51]. Therefore a voltage ramp-up time of $0.3\,\mathrm{s}$ is deemed satisfactory for soft-charging the LC filter and *Transformer 1*.

Energisation Overhead Line and Transformer 2

In the following energisation step, the passive components of the overhead line *OHL50* and the *Transformer 2* are energised by hard switching. This is done by energising one component after another with a sufficient time interval in between [8]. Therefore the overhead line is first energised at $0.5\,\mathrm{s}$ followed by the second transformer at $1.5\,\mathrm{s}$. The output current of the voltage source over the whole energisation period is shown in 5.2.

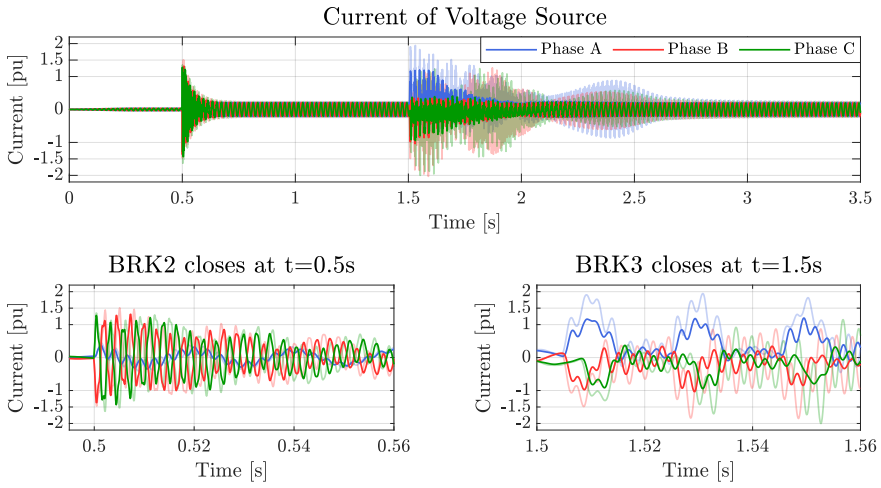

Figure 5.2: Output current of the voltage source with two zoomed subfigures when the breaker *BRK2* and *BRK3* closes at $0.5\,\mathrm{s}$ and $1.5\,\mathrm{s}$ respectively. The transparent lines show the current without a tap changer, while the full lines show the output current when the secondary voltage of *Transformer 1* is reduced by $10\,\%$ through the tap changer. Note that $1\,\mathrm{pu}$ corresponds to the nominal phase current of $1.262\,\mathrm{kA}$.

Considering only the transparent lines in this figure, large transient inrush currents in the output current of the voltage source can be observed at the two switching instants $0.5\,\mathrm{s}$ and $1.5\,\mathrm{s}$. When the overhead line is energised, a transient current with a peak value of more than $1.5\,\mathrm{pu}$ can be noted in Phase B and C, which decays as underdamped oscillation within $0.2\,\mathrm{s}$ [52]. Phase A shows minimum to no transient response but is also superimposed by a frequency component of around $350\,\mathrm{Hz}$ as Phase B and C due to an interaction between the line capacitance and the inductive elements in the system. The lower transient response in Phase A can be explained by the voltage in Phase A being at zero crossing, while Phase B and C are close to their peak value and therefore have a higher transient response [52].

During the energisation of *Transformer 2* starting at $1.5\,\mathrm{s}$, the transient inrush currents reach a maximum of about $2\,\mathrm{pu}$. These maximum peaks occur several cycles after the breaker *BRK3* was closed. However, here the decay process lasts longer than $1.5\,\mathrm{s}$, and the current signals are superimposed by more than one dominant frequency component resulting in highly distorted current waveforms. A more detailed analysis of the frequency and DC components contained in the phase currents of the voltage source during the whole energisation process can be found in Figure B.2 in Appendix B.2.

At both switching instants, transient currents at the output of the voltage source would

exceed far the specified current limits of $1.1\,\mathrm{pu}$ as described in Section 4.2.3. To mitigate the observed transient currents, the voltage is reduced by implementing an on-load tap changer on the high voltage side of *Transformer 1* [43]. The basic schematic of the used tap changer can be found in Figure B.1a in Appendix B.1. Following the lower voltage limit for the energisation process given in Section 2.1.2, the tap changer is set to a value of $-10\,\%$. The effect of this implementation can be seen again in Figure 5.2, marked as full lines. While this implementation has only a small damping effect on the transient currents for the overhead line energisation, it leads to a significant reduction of the maximum current transient of around $60\,\%$ when *Transformer 2* is energised at $1.5\,\mathrm{s}$. Additionally, the previously existing long-lasting decaying process is significantly shortened.

Since the maximum transient current still reaches about $1.43\,\mathrm{pu}$, Pre-Insertion Resistor (PIR)s are additionally implemented in the breakers *BRK2* and *BRK3*. Generally, PIR have the ability to lower the peak and fasten the decay of transient currents [31]. The schematic of the PIR structure used by PSCAD [53] can be found in Figure B.1b in Appendix B.1. The value for the resistance is chosen to be $600\,\Omega$, while the on-time is set to $10\,\mathrm{ms}$ following [54] and [55] respectively. Figure 5.3 compares the output current of the voltage source for the energisation process up to *Bus4* with PIRs and the tap changer to the results in Figure 5.2 where only the tap changer is used.

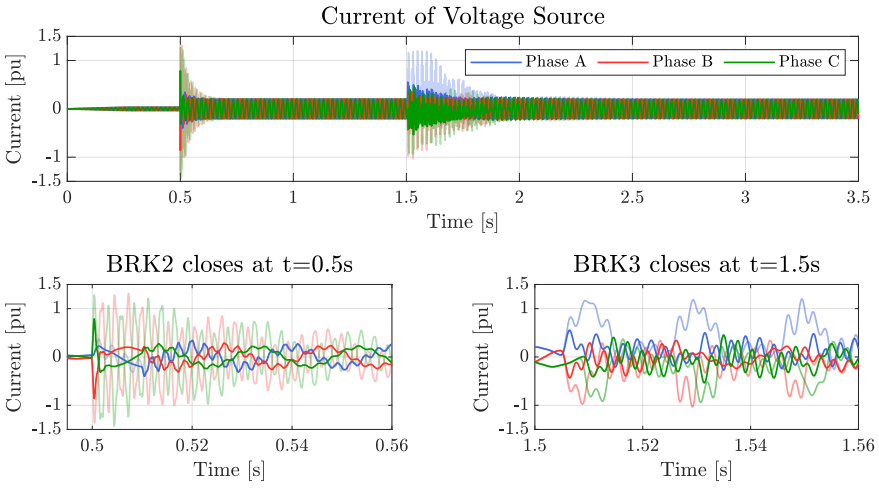

Figure 5.3: Output current of the voltage source with two zoomed subfigures when the breaker *BRK2* and *BRK3* closes at $0.5\,\mathrm{s}$ and $1.5\,\mathrm{s}$ respectively. The transparent lines show the current with a tap of $-10\,\%$ at *Transformer 1*, while the full lines show the output current when PIRs in breaker *BRK2* and *BRK3* are implemented additionally. Note that $1\,\mathrm{pu}$ corresponds to the nominal phase current of $1.262\,\mathrm{kA}$.

The damping effect of the additionally implemented PIRs can be clearly seen in the figure above. During the on-time of the PIR in *BRK2* between $0.5\,\mathrm{s}$ and $0.51\,\mathrm{s}$ the maximum occurring current peak can be reduced to $0.86\,\mathrm{pu}$ and oscillation are mostly suppressed. After $10\,\mathrm{ms}$, when the PIR in *BRK2* is bypassed, a superimposed frequency component with a significantly smaller amplitude than without PIR is visible in all phases with the previously found frequency of about $350\,\mathrm{Hz}$. It can also be seen that the application of

a PIR leads to a much faster decay of the transient currents when closing breaker *BRK2*. When energizing *Transformer 2* at $1.5\,\mathrm{s}$, the PIR in *BRK3* also leads to significant improvements by reducing the maximum transient currents by more than half to around $0.55\,\mathrm{pu}$. In addition, the decay process can be significantly further accelerated, leading to an earlier settling of the current to a steady state.
In Appendix B.2, the influence of the PIR and implemented tap changer in *Transfomrer 1* on the frequency and DC components in the phase currents of the voltage source during the whole energisation process is further investigated.

5.1.1 Discussion and Summary of Initial Investigations

Overall, it can be seen that the combined application of transformer tap changer and PIRs results in a substantial reduction in the maximum transient currents from around $2\,\mathrm{pu}$ to $0.86\,\mathrm{pu}$ and to a much faster decay process. Moreover, the harmonic components occurring during the energisation process can be successfully damped, as shown in Appendix B.2. However, it should be noted that the implementation of PIRs has the disadvantage that it leads to higher system costs and additional losses during its on-time, i.e. heat dissipation [31]. The losses during the on-time of $10\,\mathrm{ms}$ are investigated in Figure B.6 in the Appendix B.3 and correspond to $0.0072\,\mathrm{MJ}$ for *BRK2* and $0.0044\,\mathrm{MJ}$ for *BRK3*. These values define the heat capacity, that the PIRs have to be able to absorb. On the other hand, on-load tap-changers are the most widely used technology for voltage regulation regardless of the voltage level and are therefore more likely to be available for the black start process [1].

Through the investigation of the energisation process carried out in this section, a black start procedure has been developed to energise passive components. Based on the results from the investigation in this section, the energisation process can be summarised as follows:

- **Step 1:** Soft charging of the LC filter and *Transformer 1* from $0\,\mathrm{pu}$ to $1\,\mathrm{pu}$ during $0\,\mathrm{s}$ to $0.3\,\mathrm{s}$.
- **Step 2:** Closing breaker *BRK2* at $0.5\,\mathrm{s}$, the overhead line *OHL50* will be energised. This energisation step is executed with a PIR of $600\,\Omega$ and an on-time of $10\,\mathrm{ms}$ in *BRK2*. Additionally an on-load tap changer at the high voltage side of *Transformer 1* that lowers the voltage to 0.9 of U_n is implemented.
- **Step 3:** Closing breaker *BRK3* at $1.5\,\mathrm{s}$, *Transformer 2* will be energised. As in **Step 2**, a PIR of $600\,\Omega$ with an on-time of $10\,\mathrm{ms}$ is used for this in *BRK3* and the tap changer keeps its high voltage side at 0.9 of U_n.

In accordance with the outlined energisation steps above, the time sequence for the energisation up to *Bus4* is shown in Figure 5.4:

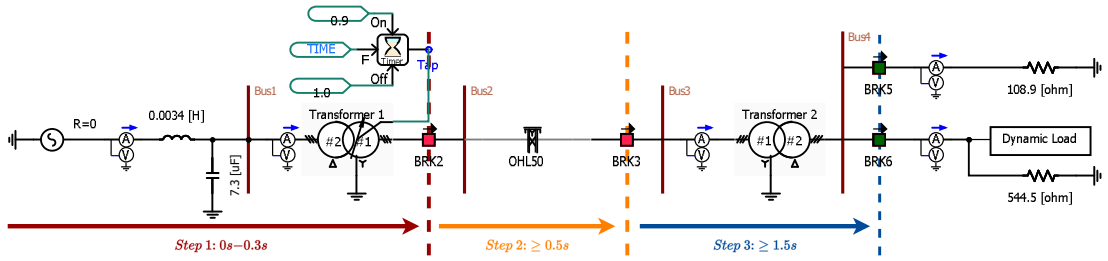

Figure 5.4: Visualization of the time sequence for the energisation of the passive components in the PSCAD model.

5.2 Black Start with Voltage Source

Based on the introduced black start procedure in Section 5.1, the energisation process of the system shown in Figure 4.1 is repeated. Again an ideal voltage source that represents the *STATCOM-BESS* is used, to evaluate the impact of the energisation process on the system rather than on the perspective of the black start service provider. This section therefore examines the system response at different measuring points.

As a starting point of this analysis, the phase voltages at the low voltage side of *Transformer 1* are shown in Figure 5.5.

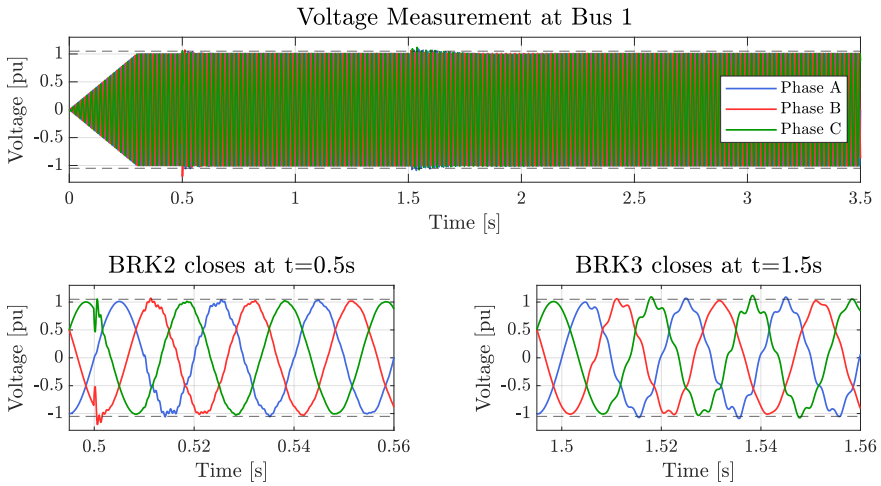

Figure 5.5: Phase voltages with an amplitude of $U_{peak} = 26.9\,\text{kV}$ (1 pu) measured at *Bus1* with two zoomed subfigures when the breaker *BRK2* and *BRK3* close at 0.5 s and 1.5 s respectively. The dashed line marks the maximum operating voltage of $1.05 \cdot U_{peak}$ considered for TOVs.

The figure shows that disturbances in the sinusoidal voltage waveform appear when energising the overhead line *OHL50* at 0.5 s and *Transformer 2* at 1.5 s. At around 0.5 s when the overhead line is energised, two prominent voltage spikes appear, reaching 0.47 pu and 1.06 pu in Phase C and -0.52 pu and -1.2 pu in Phase B. These spikes occur again in the following cycles but to a much lesser extent, and have essentially subsided after around three cycles. After the *Transformer 2* is energised at 1.5 s, the overvoltage as well

as harmonic distortion can be detected in all phases. In Phase A and C, however, higher distortions and overvoltages can be observed than in Phase B, which reach a maximum of about $-1.09\,\mathrm{pu}$ in Phase A at $1.535\,\mathrm{s}$ and $1.12\,\mathrm{pu}$ in Phase C at $1.538\,\mathrm{s}$. The decay of the voltage disturbances takes approximately $0.25\,\mathrm{s}$ until the phase voltage reaches a steady state and no more obvious distortion can be detected.
Defining the maximum operating voltage of the system as $1.05\,\mathrm{pu}$ according to *CIGRE WG 33.10* [56], the overvoltages observed in Figure 5.5 are considered as TOVs, as they exceed $1.05\,\mathrm{pu}$ and last for $20\,\mathrm{ms}$ or longer [57]. In detail, TOVs appear in Phase A after the energisation of the overhead line and in Phase A and C after the energisation of *Transformer 2*. The occurrence of TOVs is not considered to be problematic according to the *Technical Guidance Note* [58] on TOVs published by NGESO. Here it is defined that TOVs must not exceed the maximum phase operating voltage by $200\,\%$. Consequently, this corresponds to a maximum permissible value of $2.1\,\mathrm{pu}$, which is not violated in Figure 5.5 at any time. Moreover, the RMS voltage limits of NGESO as defined in Table 2.1 are not exceeded as shown in Figure C.2 in Appendix C.

In the next step, the current flow between the filter and *Transformer 1* is analysed as shown in Figure 5.6.

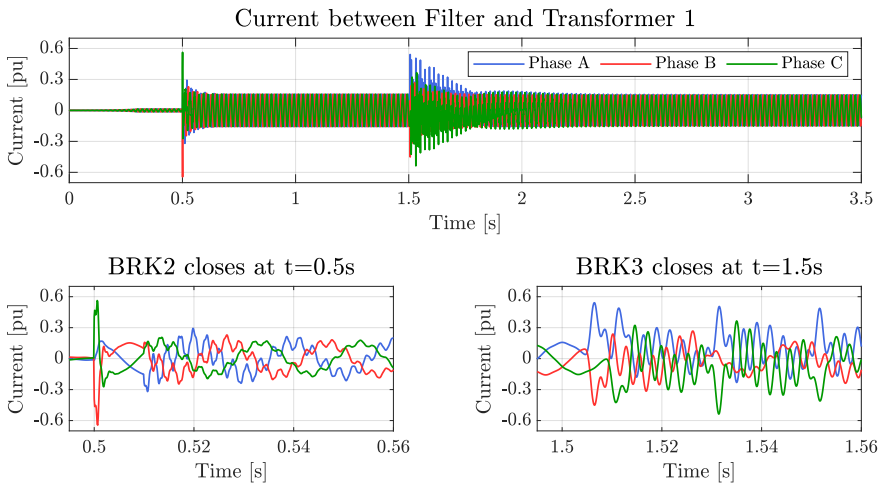

Figure 5.6: Phase currents measured between the filter and *Transformer 1* with two zoomed subfigures when the breaker *BRK2* and *BRK3* closes at $0.5\,\mathrm{s}$ and $1.5\,\mathrm{s}$ respectively. Note that $1\,\mathrm{pu}$ corresponds to the nominal phase current of $1.262\,\mathrm{kA}$.

At $0.5\,\mathrm{s}$, the current experiences a transient response with a maximum current of $-0.64\,\mathrm{pu}$ in Phase B and $0.56\,\mathrm{pu}$ in C, which quickly decay but still have highly distorted waveforms. From $1.5\,\mathrm{s}$ on, the distortion of the current waveform is significantly higher than after energising the line at $0.5\,\mathrm{s}$ and decay takes more time. The highest spikes appear at $1.507\,\mathrm{s}$ in Phase A and $1.55\,\mathrm{s}$ and Phase C with about $0.54\,\mathrm{pu}$ respectively. Overall, the observed behaviour is comparable to the tendencies in Figure 5.3 in Section 5.1.
In addition, the observed transient voltages when energising the overhead line and *Transformer 2* at $0.5\,\mathrm{s}$ and $1.5\,\mathrm{s}$ lead to a slight increase in the magnetisation current of *Trans-*

former 1. Therefore, it only has a minor influence on the current shown in Figure 5.6. The magnetisation current of *Transformer 1* is shown in Figure C.1 in Appendix C.

For further assessment of the system response, a second voltage and current measurement point at the high voltage side of *Transformer 2* is analysed. The corresponding phase voltages can be seen in Figure 5.7.

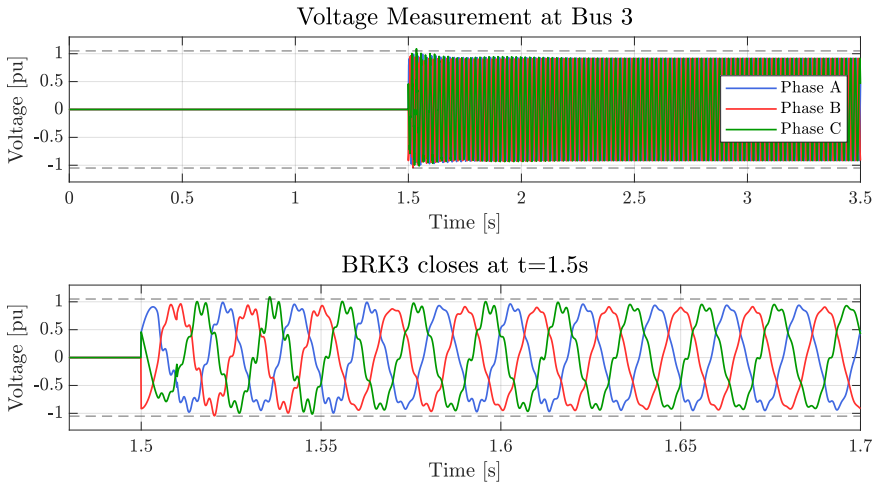

Figure 5.7: Phase voltages with an amplitude of $U_{peak} = 179.6\,\mathrm{kV}$ (1 pu) measured at *Bus3* with one zoomed subfigures when the breaker *BRK3* closes at $1.5\,\mathrm{s}$. Note that the measurement at $0.5\,\mathrm{s}$ is not shown, as *Bus3* is not energised at this time. The dashed line marks the maximum operating voltage of $1.05 \cdot U_{peak}$ considered for TOVs.

The figure shows that the close distance to *Transformer 2* increases the intensity of the voltage disturbances, which are also visible to a much lesser extent in Figure 5.5. At this measuring point, all phase voltages are distorted and overvoltages occur that reach a maximum of $-1.04\,\mathrm{pu}$ at $1.52\,\mathrm{s}$ in Phase B and $1.09\,\mathrm{pu}$ at $1.536\,\mathrm{s}$ in Phase C. The decay process takes approx. $0.8\,\mathrm{s}$ until the phase voltage reaches a steady state and no significant distortion can be detected anymore. Furthermore, no TOVs can be seen, as the overvoltages exceed $1.05\,\mathrm{pu}$ once, but do not last $20\,\mathrm{ms}$ or longer. The seen voltage disturbances are also within the tolerable range as the corresponding RMS voltage stays within RMS voltage limits given by NGESO. This can be seen in Figure C.2 in Appendix C.

The corresponding current between the overhead line *OHL50* and *Transformer 2* of this second measuring point is shown in Figure 5.8.

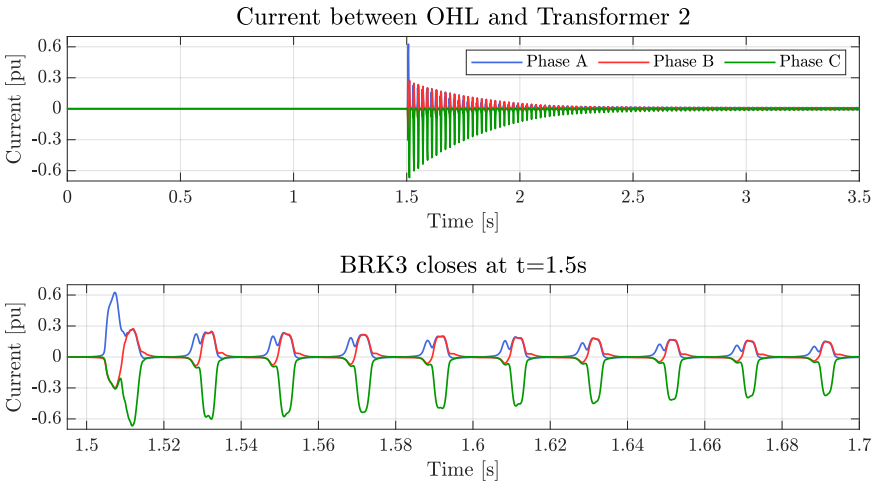

Figure 5.8: Phase currents measured between overhead line and *Transformer 2* with one zoomed subfigure when the breaker *BRK3* closes at $1.5\,\mathrm{s}$. Note that the measurement at $0.5\,\mathrm{s}$ is not shown, as *Bus3* is not energised at this time. Note that $1\,\mathrm{pu}$ corresponds to the nominal phase current of $0.189\,\mathrm{kA}$.

In the above Figure, transient inrush currents are visible after breaker *BRK3* closes a $1.5\,\mathrm{s}$, in particular for Phase A and C, reaching a maximum of about $0.65\,\mathrm{pu}$. The phase currents in Phase A and C show the typical characteristics of inrush currents with their half-cycle waveform and superimposed by a DC component [51]. This is the case as the voltages of phases A and C are comparatively closer to zero crossing at the switching instant, while Phase B contains only a minimal DC component as its phase voltage is close to the negative voltage peak at the switching instant.
In order to determine the origin of the high inrush currents in Figure 5.8, the magnetisation current of *Transformer 2* is shown in Figure 5.9.

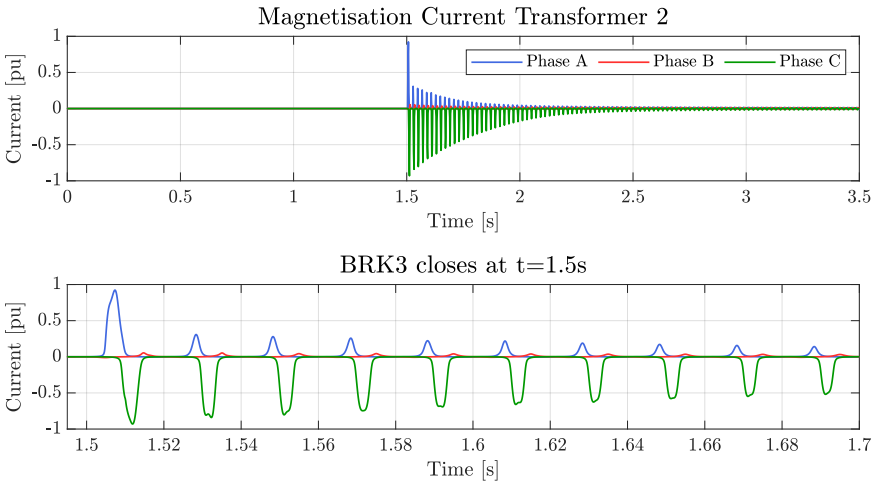

Figure 5.9: Magnetisation current of *Transformer 2*. Note that the polarity of the magnetisation current is changed to match with Figure 5.8, as PSCAD measures magnetisation current in the transformer model with different polarity. Note that $1\,\mathrm{pu}$ corresponds to the nominal phase current of $0.189\,\mathrm{kA}$.

This figure shows how the voltage value of each phase voltage at the switching time

of the breaker *BRK3* influences the drawn magnetizing current in *Transformer 2* due to the saturation of the magnetic core and thus the inrush current in each phase. Phase B, which is at its negative voltage peak at the time of switching, only draws a low magnetisation current, which is then also reflected in the inrush current of Phase B in Figure 5.8. On the other hand, Phases A and C draw a significantly higher magnetisation current through their voltage values at the switching instant, which results in higher inrush currents in Figure 5.8. The delayed sharp increase of the magnetizing currents shown at around $1.504\,\mathrm{s}$ in Phase A and at $1.508\,\mathrm{s}$ in Phase C is due to the saturation range not being reached immediately. The magnetizing currents behave in the beginning still linear, as seen in Figure 4.2. This behaviour occurs periodically after the magnetic core is desaturated by the opposite voltage half-wave. Moreover, a harmonic analysis of the frequency components contained in the magnetisation current of *Transformer 2* is performed in Appendix B.2. This shows time-varying low-order harmonics occur during the energisation of *Transformer 2* and an expected DC component, particularly in Phases A and C. It is also observed that the magnetisation currents in Figure 5.9 are higher than the inrush currents in Figure 5.8. In order to further investigate this behaviour, a simplified model was built consisting only of an ideal voltage source, a transformer and a breaker with the same model parameters. However, it was found that the phenomenon still occurs, confirming the accuracy of the model in this project and that the behaviour is caused within the transformer model of PSCAD.

The active and reactive power of the ideal voltage source during the energisation process can be seen in Figure 5.10.

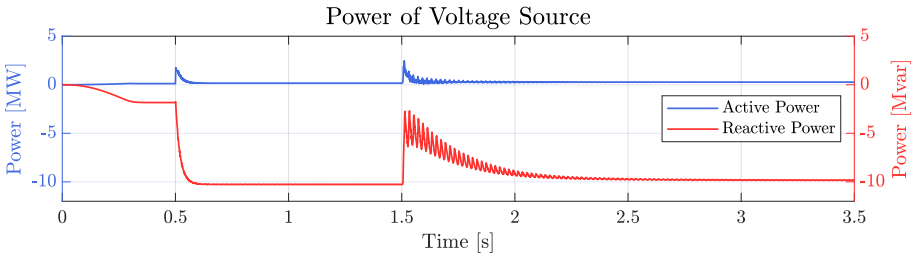

Figure 5.10: Active and reactive power of the ideal voltage source as the sum of all three phases. Note that a smoothing time constant of $0.02\,\mathrm{s}$ for power measurements in PSCAD is used.

In the first $0.3\,\mathrm{s}$ when soft-charging is applied, a steadily increasing reactive power can be observed, which is absorbed by the ideal voltage source and generated by the capacitance C_f of the filter. This also shows that the filter capacitance provides more reactive power than *Transformer 1* absorbs during and after its energisation. After closing breaker *BRK2* at $0.5\,\mathrm{s}$, the overhead line *OHL50* is energised, leading to an increased reactive power absorption of $-10.3\,\mathrm{Mvar}$ by the voltage source. This is due to the overhead line being unloaded, which results in higher charging currents of the capacitive components than the actual load current and thus to an overall capacitive and not inductive behaviour of the overhead line. This behaviour is also known as the Ferranti effect [43].
With closing breaker *BRK3* at $1.5\,\mathrm{s}$, a significant reduction in reactive power by around

$8\,\mathrm{Mvar}$ can be seen, which is due to the energisation of the highly inductive *Transformer 2*. It absorbs reactive power due to the drawn magnetization current as shown in Figure 5.9. As a result, the reactive power of the line is largely compensated for a short time. However, after the energisation moment, the reactive power increases again, with high fluctuations due to the observed voltage and current disturbances. It reaches a steady state slightly below the value before the transformer was energised.
For the active power, two peaks can be detected when the overhead line and the transformer are energised and reach a maximum of $1.76\,\mathrm{MW}$ and $2.47\,\mathrm{MW}$ respectively.

5.2.1 Conclusion

Overall it can be seen that the energisation process leads to significant transient inrush currents and transient voltages. Furthermore, considerable distortions occur due to low-order harmonics, particularly in the current signals. While the transient currents do not lead to a violation of the maximum phase current of $1.1\,\mathrm{pu}$ of the black start service provider as specified in Section 4.2.3, overvoltages occur on the $33\,\mathrm{kV}$ side of *Transformer 1* and the $220\,\mathrm{kV}$ side of *Transformer 2*. However, these do not violate the limits for TOVs and RMS voltages specified by NGESO. Finally, the active and reactive power capacities of the voltage source are not exceeded during the entire energisation process.

5.3 Black Start with STATCOM-BESS

After investigating the black start of the system with an ideal voltage source in the previous section, the black start procedure is repeated with the *STATCOM-BESS* and its developed GFM controller. This section aims to prove the ability of the *STATCOM-BESS* to carry out a black start of the system shown in Figure 4.1 til *Bus4*.

Initial Investigations for the Black Start with STATCOM-BESS
While conducting initial black start tests with the *STATCOM-BESS* as the black start service provider, expected voltage and current disturbances caused by the energisation of the overhead line and the two transformers affected the controller performance of the *STATCOM-BESS* and thus the overall system behaviour. The behaviour could be improved by the implementation of signal filtering for the measured input parameters $v_{d,meas}$, $v_{q,meas}$, $i_{d,meas}$ and $i_{d,meas}$. This is further described in Appendix D.1. It was found that the implementation of second-order LPFs with characteristic frequencies of 100 Hz for $i_{d,meas}$ and $i_{d,meas}$ and 2000 Hz for $v_{d,meas}$ and $v_{q,meas}$ reduce the level of distortion and oscillation of $v_{abc,meas}$ and $i_{abc,meas}$ and improve the overall system behaviour during the black start.

After implementing the signal filtering in the GFM controller, the necessity of having the damping capabilities provided by the PIRs in *BRK2* and *BRK3* during black start is verified once more. This is done by evaluating their effect on the output current *STATCOM-BESS* as shown in Figure 5.11.

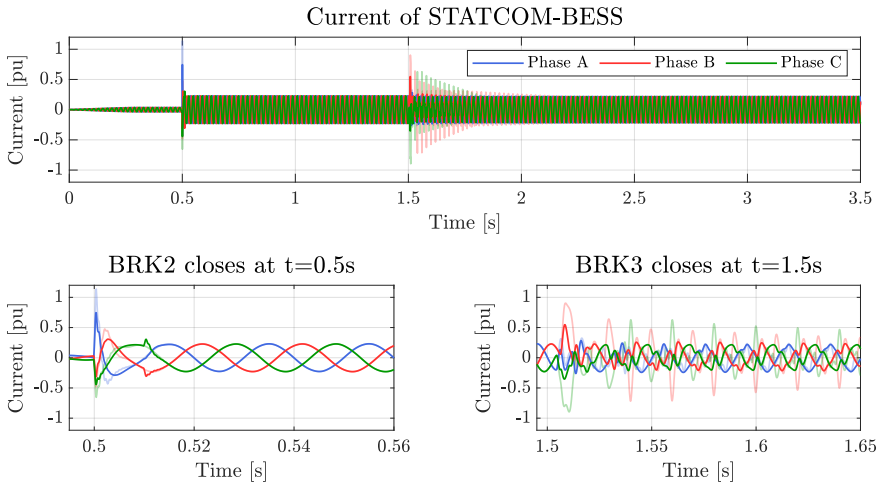

Figure 5.11: Output current of the *STATCOM-BESS* with two zoomed subfigures when the breaker *BRK2* and *BRK3* closes at 0.5 s and 1.5 s respectively. The transparent lines show the current without PIRs, while the full lines show the output current when PIRs are applied in the breakers *BRK2* and *BRK3* for 10 ms. Note that 1 pu corresponds to the nominal phase current of 1.262 kA.

It can be seen that through damping of the PIRs the transient behaviour and the distortions in the current waveforms can be significantly reduced overall. In addition, the

maximum current occurring at the output of the *STATCOM-BESS* also decreases significantly from $1.14\,\mathrm{pu}$ to $0.75\,\mathrm{pu}$.

This section will investigate the performance of the *STATCOM-BESS* and the corresponding system behaviour during the black start. As the updated control scheme with the second-order LPFs and the PIRs in breakers *BRK2* and *BRK3* have proven their positive effect, both implementations are considered.
For the overall black start procedure, it is referred to Section 5.1, with the only adjustment that no tap changer is used in *Transformer 1*, as the voltage is lowered by the voltage reference v_d^* within the VSM control scheme of the *STATCOM-BESS*. The system will be soft-charged from $0\,\mathrm{pu}$ to $0.95\,\mathrm{pu}$ within $0.3\,\mathrm{s}$ using an up ramp block from PSCAD and it remains at $0.95\,\mathrm{pu}$ during the whole energisation of the system.

Analysis Black Start with STATCOM-BESS
Following the order of the analysis in Section 5.2, the phase voltages v_{meas} on the low-voltage side of *Transformer 1* are first shown in Figure 5.5 during the energisation of the system.

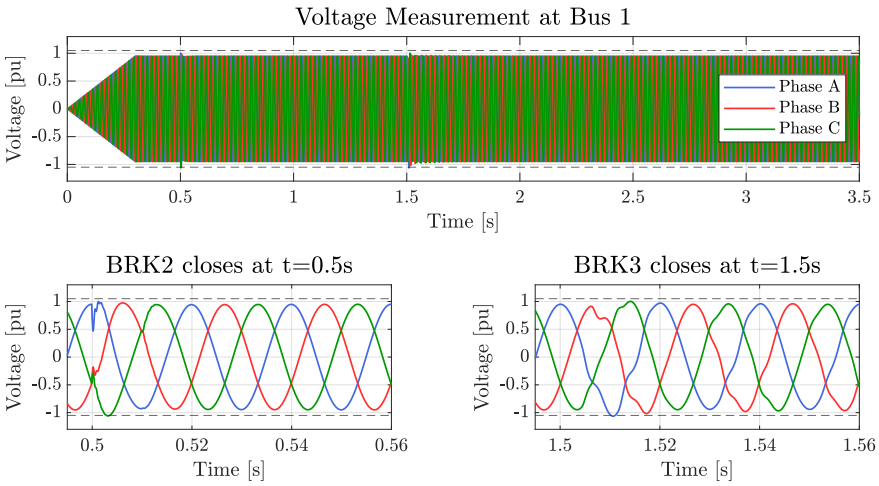

Figure 5.12: Phase voltages v_{meas} with an nominal amplitude of $U_{peak} = 26.9\,\mathrm{kV}$ (1 pu) measured at *Bus1* with two zoomed subfigures when the breaker *BRK2* and *BRK3* close at $0.5\,\mathrm{s}$ and $1.5\,\mathrm{s}$ respectively. The dashed line marks the maximum operating voltage of $1.05 \cdot U_{peak}$ considered for TOVs.

This figure shows that the voltage amplitude increases to $0.95\,\mathrm{pu}$ within $0.3\,\mathrm{s}$ as intended and thus soft charges the filter of the *STATCOM-BESS* and *Transformer 1*. When the overhead line is energised at $0.5\,\mathrm{s}$, voltage dips and subsequent oscillating overshoots can be seen that are most severe in Phase A. The observed oscillations correspond to a frequency of $1.43\,\mathrm{kHz}$ and originate mostly from an interaction between the capacitor C_f and the series reactor L_f and *Transformer 1*. The degree of these oscillations is also influenced by the implemented second-order LPF in the GFM controller as shown in Figure D.1 in Appendix D.1. At $1.5\,\mathrm{s}$ when *Transformer 2* is energised, increased and distorted voltages can be observed, which reach a maximum in Phase C with $1.06\,\mathrm{pu}$. Due to the reduced

phase voltage to $0.95\,\mathrm{pu}$ set by the GFM controller and faster decay of harmonic distortion compared to the black start with a voltage source, no TOVs as defined in Section 5.2 are present.
Overall, it can be seen that the disturbances are attenuated comparatively quickly after both switching instances, as no TOVs can be detected, despite the phase voltages at $0.503\,\mathrm{s}$ and $1.51\,\mathrm{s}$ exceed $1.05\,\mathrm{pu}$ twice. Furthermore, the limits for the RMS voltage specified by NGESO are not violated at any time, as shown in Figure D.3 in the Appendix D.2.

In the following, the current of the measuring point between the filter of the *STATCOM-BESS* and the low-voltage side of *Transformer 1* is shown in Figure 5.13.

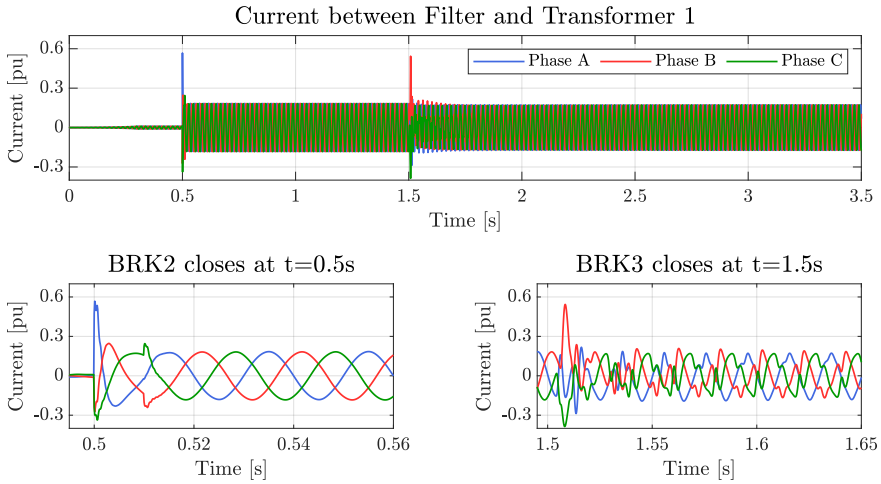

Figure 5.13: Current between the filter of the *STATCOM-BESS* and the low-voltage side of *Transformer 1* with two zoomed subfigures when the breaker *BRK2* and *BRK3* closes at $0.5\,\mathrm{s}$ and $1.5\,\mathrm{s}$ respectively. Note that $1\,\mathrm{pu}$ corresponds to the nominal phase current of $1.262\,\mathrm{kA}$.

At $0.5\,\mathrm{s}$ when the overhead line is energised, a transient current is present in all phases, with a maximum in Phase A of $0.57\,\mathrm{pu}$. When the PIR in breaker *BRK2* is bypassed after $10\,\mathrm{ms}$, a comparatively small current transient with subsequent oscillations occurs before it returns to a sinusoidal waveform. The energisation of the *Transformer 2* at $1.5\,\mathrm{s}$ leads to current transients in all phases, which are highest in Phase B with $0.54\,\mathrm{pu}$. The following distorted current waveforms are rich in low-order harmonics and only decay slowly as shown in the spectrogram in Figure D.4 in Appendix D.3 The energisation of the overhead line and *Transformer 2* at $0.5\,\mathrm{s}$ and $1.5\,\mathrm{s}$ result in a slight increase in the magnetisation current of *Transformer 1* and hence have only minimal influence on the current shown in Figure 5.13. The magnetisation current of *Transformer 1* can be found in Figure D.2 in Appendix D.2.

Following the analysis in Section 5.2, a second voltage and current measuring point located at the high voltage side of *Transformer 2* is introduced to further analyse the system behaviour during the black start with the *STATCOM-BESS*. Therefore, the corresponding phase voltages are shown in Figure 5.14.

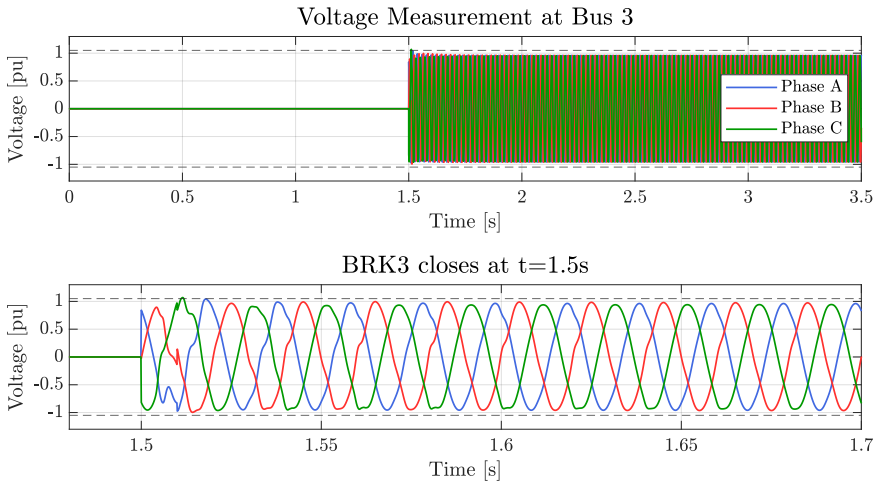

Figure 5.14: Phase voltages with an amplitude of $U_{peak} = 179.6\,\mathrm{kV}$ (1 pu) measured at *Bus3* with one zoomed subfigures when the breaker *BRK3* closes at $1.5\,\mathrm{s}$. Note that the measurement at $0.5\,\mathrm{s}$ is not shown, as *Bus3* is not energised at this time. The dashed line marks the maximum operating voltage of $1.05 \cdot U_{peak}$ considered for TOVs.

The energisation of the overhead line leads to harmonic distortion in all phases along with voltage deviation with a maximum in Phase C of $1.07\,\mathrm{pu}$. Also noticeable is the voltage disturbance in all phases that occurs at $1.51\,\mathrm{s}$ when the PIR in breaker *BRK3* is bypassed. Despite the present overvoltages, the RMS voltage limits specified by NGESO are not exceeded as shown in Figure D.3 in Appendix D.2.

Figure 5.15 shows the phase current measured between the overhead line *OHL50* and *Transformer 2* as well as the magnetisation current of *Transformer 2*.

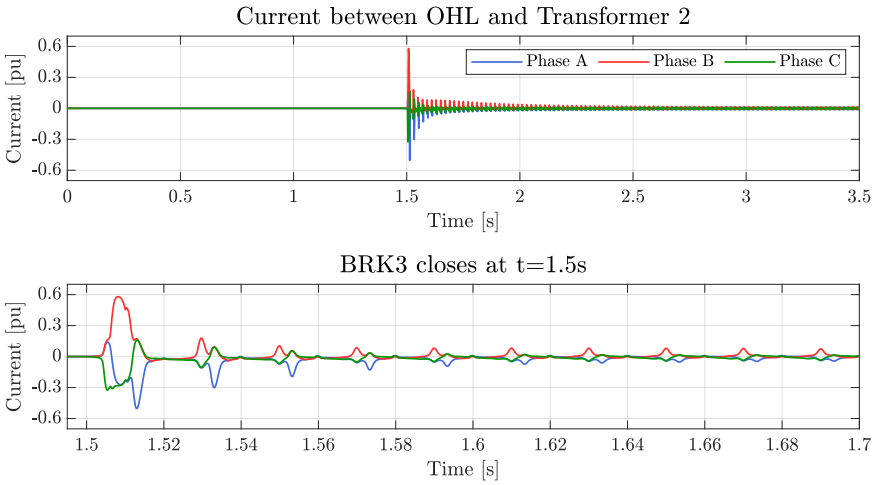

(a) Phase currents measured between overhead line and *Transformer 2*.

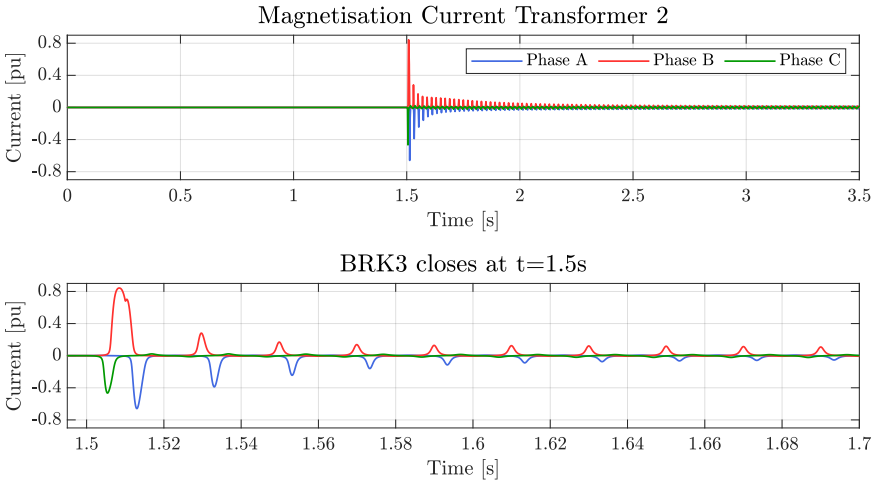

(b) Magnetisation current of *Transformer 2*.

Figure 5.15: Phase currents measured between overhead line and *Transformer 2* **(a)** and Magnetisation current of *Transformer 2* **(b)**. Note also that $1\,\mathrm{pu}$ corresponds to the nominal phase current of $0.189\,\mathrm{kA}$ and that the polarity of the magnetisation current in **(b)** is changed to match with Figure 5.15a, as PSCAD measures magnetisation current in the transformer model with different polarity.

When the breaker *BRK3* is closed at $1.5\,\mathrm{s}$, transient inrush currents with a characteristic half-wave shape and DC component occur in the magnetisation current of *Transformer 2*. The current in Phase B shows the highest inrush current with $0.58\,\mathrm{pu}$, as the corresponding phase voltage in Figure 5.14 is at zero crossing when energising *Transformer 2*. As the voltage in Phase C is shortly before the negative peak when breaker *BRK3* is closed, it leads to a negative inrush current. Finally, the characteristics of the current in Phase A also relate to the corresponding phase voltage, which starts in the last third of the positive half-wave and is followed by a comparatively longer negative half-wave, resulting in an overall negative inrush current.

Furthermore, an analysis of the harmonic performance in Section D.3 shows that the magnetisation currents in Phase A and C are rich in time-varying low-order harmonics during the energisation of *Transformer 2*. Most noticeable are the 2nd, 3rd and 4th harmonics and the expected DC components.
In Figure 5.15a, it can be seen that the basic characteristic of the inrush current is shaped by the magnetisation currents of *Transformer 2*. However, not all of the behaviour observed in the current waveform in Figure 5.15a can be linked to the magnetisation currents. This observation is further illustrated in the Appendix D.3.

The following Figure 5.16 shows the power output and frequency of the *STATCOM-BESS* after the series reactor L_f.

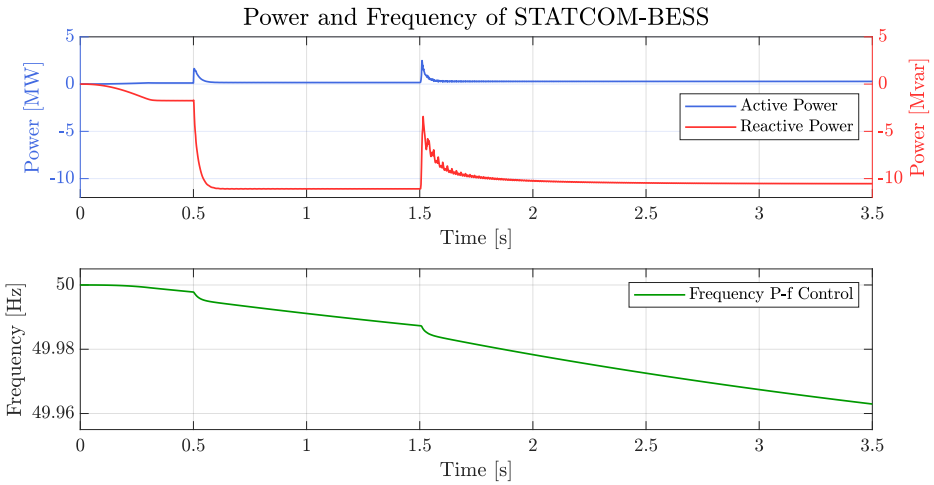

Figure 5.16: Active and reactive power of the *STATCOM-BESS* as the sum of all three phases after the series reactor L_f. Note that a smoothing time constant of $0.02\,\mathrm{s}$ for power measurements in PSCAD is used.

The active and reactive power of the *STATCOM-BESS* after the series reactor L_f can be seen in the upper subfigure. The same tendencies and phenomena can be observed in Figure 5.10 in Section 5.2. However, compared to the ideal voltage source, notable lower ripples in the output power are visible. This is due to the lower voltage and current disturbances during the black start, which have a particular effect on the reactive power when *Transformer 2* is energised at $1.5\,\mathrm{s}$. The output frequency of the *STATCOM-BESS*, which only depends on the provided active power, is seen in the lower subfigure.
As soon as the soft-charging increases the output voltage of the *STATCOM-BESS*, it has to provide active power to compensate for losses in *Transformer 1*, which leads to a first decrease in frequency. The steepness of frequency decay and the settled frequency per active power is dependent on the inertia constant and the damping constant as described in Section 4.2.1. At $0.5\,\mathrm{s}$, when the overhead line is connected, an initial spike in the active and reactive power response of the *STATCOM-BESS* can be seen. Afterwards, the *STATCOM-BESS* has a steady active power output of $0.17\,\mathrm{MW}$, which leads to a further decrease in frequency. At $1.5\,\mathrm{s}$, *Transformer 2* is connected, leading to higher steady-state output power of around $0.28\,\mathrm{MW}$. This further speeds up the frequency decay. Due to

the comparatively short observation period of $3.5\,\mathrm{s}$, mainly the inertia constant affects the frequency decay, which leads to its gradual decrease. With a longer observation time, the frequency for an output power of $0.28\,\mathrm{MW}$ would settle at around $49.93\,\mathrm{Hz}$ as defined through the damping constant D_p.

5.3.1 Conclusion

Overall, the energisation processes carried out in this section yielded much smoother results than those obtained with the ideal voltage source in Section 5.2. Furthermore, the overall ability to successfully energise the system using the *STATCOM-BESS* as the black start service provider was proven. This is due to the RMS voltages at the considered measuring points staying within the permissible limits specified by NGESO. In addition, the defined current limit of the *STATCOM-BESS* of $1.1\,\mathrm{pu}$ was well maintained. These results can be attributed to the damping properties of the GFM control structure including the LPFs, the lowered system voltage to $0.95\,\mathrm{pu}$ and the PIRs in *BRK2* and *BRK3*. Finally, the power demand of the island system during the black start could be covered by the GFM-based *STATCOM-BESS* without exceeding its power capabilities.

5.4 Summary

In this chapter, the energisation of the system til *Bus4* has been performed initially with an ideal voltage source and subsequently with the GFM-based *STATCOM-BESS*. The system and controller responses were analysed based on relevant limits given by NGESO. Specifically, emphasis was put on the assessment of voltage and current disturbances during the energisation of the overhead line and the transformers. Furthermore, the necessity of signal filtering of the dq-components in the VSM control scheme and the relevance of mitigation techniques including the reduction of the system voltage and PIRs for the energisation process were demonstrated.

6 Analysis II: Block Loading

After the successful energisation of the system til *Bus4* in Section 5.3, the tests in this chapter aim to prove the overall capability of the *STATCOM-BESS* to establish a power island by performing block loading of a $10\,\mathrm{MW}$ static load at distribution level according to the requirements specified by NGESO and ELIA. This corresponds to the final step to complete *Stage 2* as introduced in Figure 2.3. In addition to the investigation of the energisation of a static load, a dynamic load model will be designed and analysed. Furthermore, a GFL-based generation unit connected to *Bus4* is added, to de-load the *STATCOM-BESS* by providing a local power supply for the loads connected at the distribution level. The expanded system built in PSCAD, which will be considered in this chapter, can be seen in Figure 6.1.

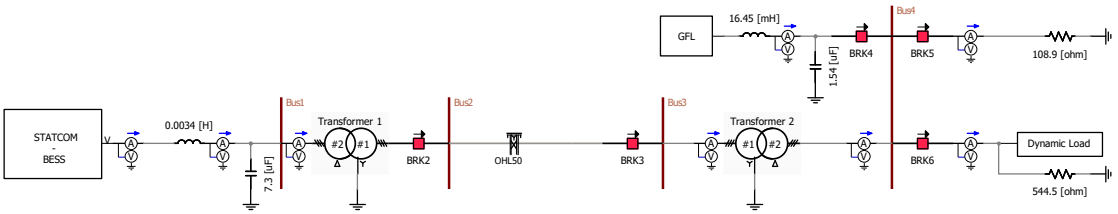

Figure 6.1: Single line diagram of the expanded system in PSCAD.

The pure static load is modelled as a resistance with a value of $108.9\,\Omega$ corresponding to the required block load of $10\,\mathrm{MW}$ as stated in Section 2.1.2. The dynamic load model consists of an induction motor with a resistance connected in parallel. The total rated power of the dynamic load model is $5\,\mathrm{MVA}$. The GFL unit, that is additionally connected to *Bus4*, has a rated power of $10\,\mathrm{MW}$.

The following sections of this chapter provide a description of the modelling of the components connected to the distribution system as well as the analysis of the energisation of the dynamic and static loads. Therefore this chapter is structured as follows:

- **Section 6.1**: This section describes the modelling of the components connected at the distribution level, including the GFL control structure and the model of the induction motor.
- **Section 6.2**: This section covers the test case of energising the pure static load. The system response and the interaction between the generation units are analysed.

- **Section 6.3**: The test case included in this section analyses the system response and the generation units when the dynamic load model is energised. Furthermore, increased proportions of the induction motor within the dynamic load model are tested in Section 6.3.1.

6.1 Modeling of GFL unit and Induction Motor

This section initially describes the GFL control structure and its behaviour during a step response test, followed by the modelling and characteristic behaviour of the squirrel cage induction motor.

GFL unit

The generation unit connected to the distribution system is modelled as an average model with a GFL control structure. For this GFL average model an ideal DC link is assumed, allowing the nominal power of $10\,\mathrm{MW}$ to be provided at all times to fulfil the service availability requirement given by NGESO in Table 2.1. The current and power control loop of the GFL control scheme shown in Figure 6.2 are based on the "Synchronous Frame VOC: PQ Closed-Loop Control" given in [42].

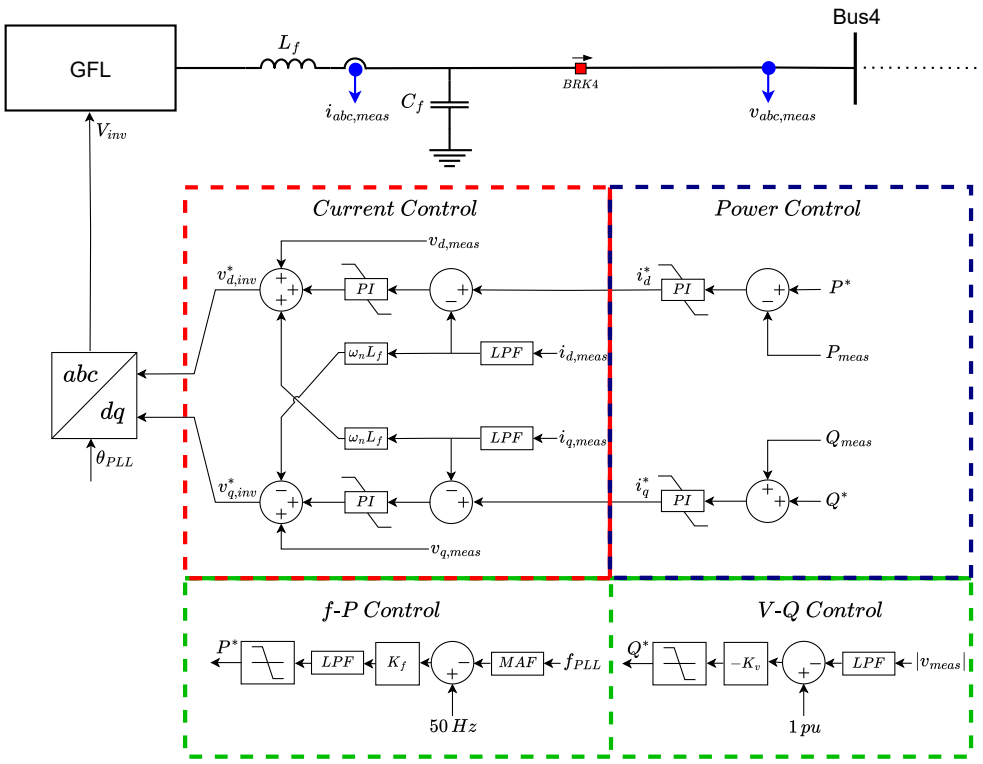

Figure 6.2: Average model of the generation unit at the distribution level with a grid-following control structure. Based on [42].

The GFL control structure shown in the Figure above consists of a cascaded scheme where the power references P^* and Q^* for the power control loop are generated by a f-P and V-Q droop control. For the voltage magnitude of the V-Q droop control, a first-order

LPF is used to smooth occurring disturbances in the measurement, while the estimated frequency of the PLL used for the f-P droop control is first filtered by a Moving Average Filter (MAF) from the PSCAD library, followed by a first-order LPF that smoothes the resulting active power reference. The relation of the droop constants K_f and K_v can be described as follows:

$$P^* = K_f \cdot \Delta f \qquad (6.1a) \qquad\qquad Q^* = -K_v \cdot \Delta|v| \qquad (6.1b)$$

Assuming a power factor of 0.95 and a droop value of $10\,\%$, the droop constant K_v in Eq. (6.1b) can be determined as 3.12, leading to a change of $0.312\,\mathrm{pu}$ ($3.29\,\mathrm{Mvar}$) in reactive power reference per $0.1\,\mathrm{pu}$ change in voltage magnitude. Based on a droop value of $0.95\,\%$, the droop constant K_f in Eq. (6.1a) is determined as 2 resulting in a $0.95\,\mathrm{pu}$ ($10\,\mathrm{MW}$) change in active power reference per $0.475\,\mathrm{Hz}$ change in frequency. This corresponds to characteristic of $21.05\,\mathrm{MW/Hz}$ and thus to a 5.26 times higher active power output per Hz than the active-power-frequency characteristic of the *STATCOM-BESS*. Note that the aforementioned per unit values are determined considering an apparent power of $10.53\,\mathrm{Mvar}$ as a base. Additionally, the limits for P^* and i_d^* are both set to $0\,\mathrm{pu}$ and $1.045\,\mathrm{pu}$, while the limits for Q^* and i_q^* are defined as $\pm 0.34\,\mathrm{pu}$. The mentioned limits, refer to a total maximum current of $1.1\,\mathrm{pu}$ as defined in Section 4.2.3. An overview of the parameters of the GFL unit including the filters, controller and PLL can be found in Table E.1 in Appendix E.

In order to verify the response of the GFL unit during rapid changes in the grid, a step response test is made. This is done in a simplified system consisting only of an ideal voltage source and the GFL unit including its LC filter. For the step response, the frequency of the ideal voltage source is set to drop at $6\,\mathrm{s}$ from $50\,\mathrm{Hz}$ down to $49.525\,\mathrm{Hz}$. At $8\,\mathrm{s}$, the frequency is set back to $50\,\mathrm{Hz}$. The corresponding power responses after the series reactor and the frequency estimation of the PLL before filtering can be seen in Figure 6.3.

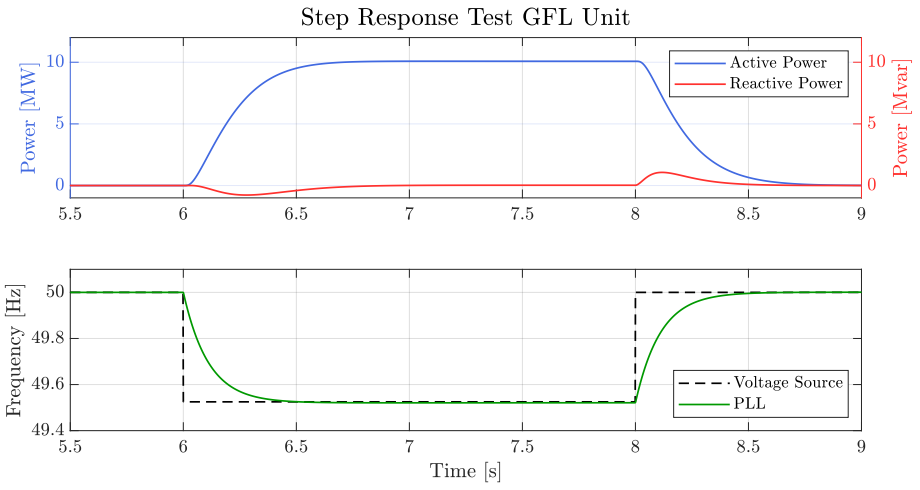

Figure 6.3: Responses of the active and reactive power of the GFL unit as the sum of all three phases as well as the frequency estimation of the PLL during the step response test.

From these step responses, it can be seen that at a steady state, the active power reaches $10.08\,\mathrm{MW}$ ($0.957\,\mathrm{pu}$), while the frequency estimation of the PLL corresponds to $49.521\,\mathrm{Hz}$. Using equation (6.1a), it can be found that the active power in a steady state corresponds accurately to the frequency deviation from $50\,\mathrm{Hz}$. It should be noted that the frequency estimation itself has an error of about $4\,\mathrm{mHz}$, leading to this slight deviation of $0.007\,\mathrm{pu}$ in active power. However, this is considered to be acceptable as it is below the measurement uncertainty of $\pm 10\,\mathrm{mHz}$ defined by the IEC 61000-4-30 standard [59].
Due to the ideal voltage source, the voltage magnitude does not deviate from its nominal value, and thus the reactive power reference of the GFL unit remains zero during the step response test. Therefore, it can be seen that the GFL controller can maintain its reactive power reference at the measuring point and only deviates when the active power changes.

Induction Motor

Electrical motors are widely used and are responsible for 60 to $70\,\%$ of the total consumed electrical energy in the power systems, whereas squirrel cage induction motors make up the majority [60]. The dynamic load is emulated by a $3\,\mathrm{MVA}$ squirrel cage induction motor based on [61], with a $2\,\mathrm{MW}$ resistance in parallel. This corresponds to a motor load of $60\,\%$ of the entire dynamic load model. The following Figure 6.4 shows the schematic as it is applied in the *Dynamic Load* block in Figure 6.1 [61].

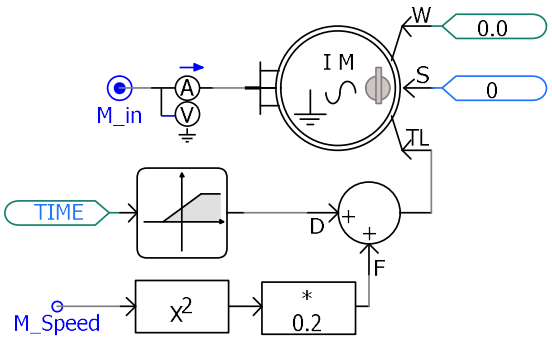

Figure 6.4: Model of squirrel cage induction motor based on [61].

The PSCAD wound rotor induction motor model can be set to work as a squirrel cage induction motor as shown in Figure 6.4 by deactivating the external connection to the rotor. By setting Input S to zero, the input TL is defined as mechanical load torque in pu. To simulate a motor start-up, the speed input W is set to zero, meaning the initial mechanical rotor speed is zero. In this project, the motor model has a small mechanical load torque that is dependent on the mechanical rotor speed *M_Speed* and reaches $0.2\,\mathrm{pu}$ of the nominal load torque at nominal rotor speed. From $10.5\,\mathrm{s}$, shortly after reaching the nominal speed, an additional mechanical torque of $0.7\,\mathrm{pu}$ will be applied as a ramp-up. The time necessary for the motor to reach nominal speed depends on various factors such as inertia constant and winding resistance. The corresponding specification of the motor used in this project can be found in Table E.2 in Appendix E.1. [61]
It shall be noted that usually, the distribution system operator defines in its grid connec-

tion regulations a maximum rated apparent power for a Direct On Line (DOL) motor starting in utility grids to avoid high inrush currents caused during motor start-up [62]. It is therefore improbable that a single 3 MVA motor will experience a DOL start-up. However, it can not be ruled out that the simultaneous starting process of multiple small motors together may cause similar disturbances. Therefore, one big induction motor with DOL start-up will be considered, to emulate this scenario.
In the following Figure 6.5, the internal measurement parameters of the modelled squirrel cage induction motor are shown. Furthermore, active and reactive power as well as the current magnitude are measured at the motor terminals. With this figure, an understanding of the motor behaviour shall be gained for further investigation when connecting the dynamic load model to the distribution network.

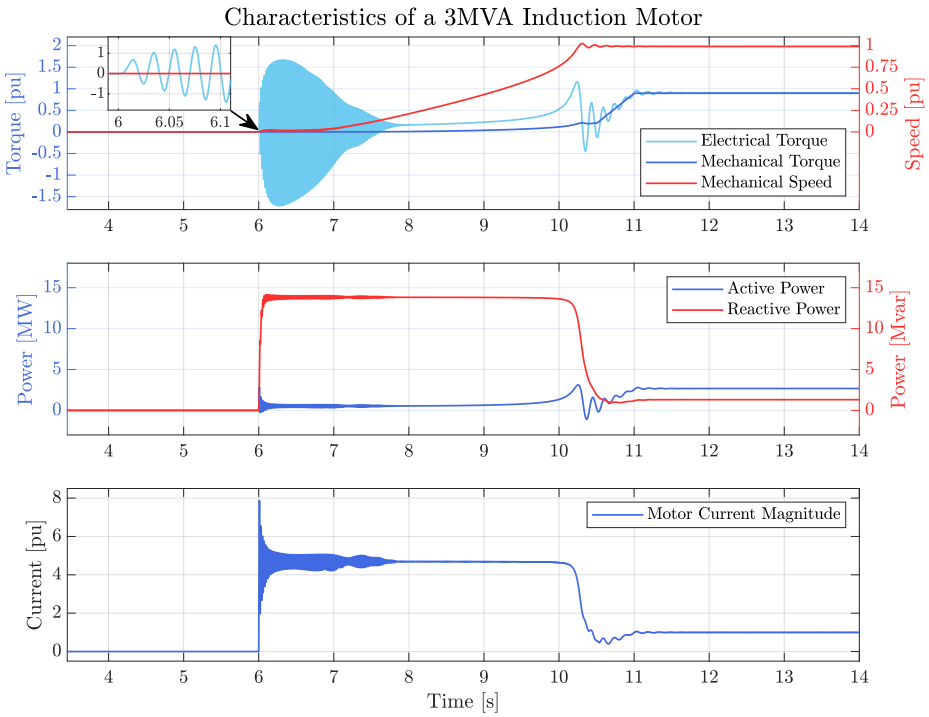

Figure 6.5: Characteristics of a 3 MVA squirrel cage induction motor start-up process with mechanical load ramp-up at 10.5 s designed as squirrel cage induction motor. Note that the third subfigure shows the motor current magnitude with 1 pu corresponding to 74.2 A, which is calculated using the α-β reference frame:

$$|i_M| = \sqrt{i_\alpha^2 + i_\beta^2}.$$

The induction motor is energised at 6 s. At this moment, multiple events can be observed. Initially, a strong oscillation in electrical torque is observable in the first subfigure, with a peak in oscillation building up until around 6.3 s and decaying afterwards. This oscillation has a frequency of around 50 Hz and is caused by transient currents in the induction motor caused by the DOL start-up [63]–[65]. The effects of the transients in the motor current magnitude are reflected in the oscillation of the electrical torque, with the difference that the current magnitude has its highest peak at the initial moment of connection. Due to the smoothing time constant, the oscillation is less visible in the active

and reactive power. Despite the oscillation in electrical torque and current magnitude, the average electrical torque is still positive. This accelerates the rotor, leading to an increase in mechanical rotor speed and therefore to an increase in mechanical load torque. The acceleration process takes place from $6\,\mathrm{s}$ to shortly after $10\,\mathrm{s}$ when the rotor reaches close to synchronous speed ($1\,\mathrm{pu}$). During acceleration, the motor draws high reactive and comparatively small active power. While the drawn reactive power stays on average at $14\,\mathrm{Mvar}$ during the acceleration process, the active power changes proportional to the electrical torque.
The modelled squirrel cage induction motor has its breakdown torque at around $96\,\%$ of synchronous speed, which is reached at around $10.2\,\mathrm{s}$. The high electrical torque causes a steep acceleration and an overshoot in mechanical speed to above $1\,\mathrm{pu}$, leading the rotor to rotate faster than the stator field. The induction machine now operates in generator mode, causing a negative electrical torque and active power flow, followed by a deceleration of mechanical speed and oscillation in electrical torque and active power flow.
With the rotor reaching steady-state mechanical speed, the reactive power consumption decreases and the mechanical torque, which inhibits the rotor, reaches $0.2\,\mathrm{pu}$. While the current magnitude decreases after $10\,\mathrm{s}$, the oscillating currents drawn by the electrical torque are still visible.
At $10.5\,\mathrm{s}$ an additional mechanical torque of $0.7\,\mathrm{pu}$ is applied with a ramp-up period of $0.5\,\mathrm{s}$. While the mechanical speed of the rotor decreases only very little, the electrical torque increases to counteract the additional applied mechanical torque. With this increase in electrical torque, also the active power demand increases, now exceeding the reactive power. The motor is now in steady-state operation condition and if the mechanical torque does not exceed the rated electrical torque of the induction motor, the mechanical speed will settle in a steady state between breakdown torque and synchronous speed.

6.2 Block Loading with GFL unit and Static Load

In the first test, the block load capability of the *STATCOM-BESS* is proven when the pure static load with $10\,\mathrm{MW}$ is instantaneously connected to the distribution network. Beyond this, the performance of the *STATCOM-BESS* and the GFL unit as aggregated units during block loading is analysed. Therefore this test includes the following steps:

- **Step 1:** Ramping up the voltage amplitude of the *STATCOM-BESS* from $0.9\,\mathrm{pu}$ to $1\,\mathrm{pu}$ between $3.5\,\mathrm{s}$ and $3.8\,\mathrm{s}$. This is done with an additional ramp-up block from the PSCAD library.
- **Step 2:** The GFL unit including its LC filter is connected to the distribution network at $4\,\mathrm{s}$ by closing breaker *BRK4*.
- **Step 3:** At $6\,\mathrm{s}$, the breaker *BRK5* is closed to connect the static load of $10\,\mathrm{MW}$ to the distribution network.

The success criteria of this test are the RMS voltage and frequency limits of NGESO and ELIA given in Table 2.1. Moreover, the current limits for the GFM and GFL controllers must be maintained.

For an initial assessment, the RMS voltage is analysed along with the current magnitude when the GFL unit including the LC filter is connected and the pure static load is energised. It should be noted that the current magnitudes have different base values, where $1\,\mathrm{pu}$ corresponds to $1.262\,\mathrm{kA}$ for the *STATCOM-BESS* and $0.261\,\mathrm{kA}$ for the GFL unit.

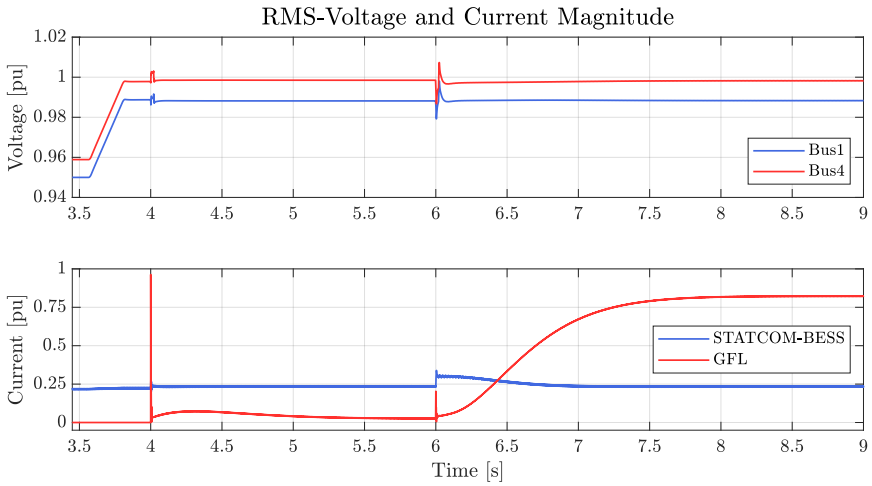

Figure 6.6: Response of current magnitude of the *STATCOM-BESS* and GFL unit measured after their series reactor as well as the line-to-line RMS value at *Bus1* and *Bus4*. Note that the current magnitude is calculated using the α-β reference frame: $|i_{meas}| = \sqrt{i_\alpha^2 + i_\beta^2}$.

In the upper subfigure, it can be seen that the voltage is initially rising towards $0.99\,\mathrm{pu}$. The reason for not reaching $1\,\mathrm{pu}$ is the absorption of reactive power by the *STATCOM-BESS* and its correspondingly reacting Q-V droop control lowering the voltage reference. The reactive power flow from the overhead line to the *STATCOM-BESS* is also the reason for the slightly higher voltage at *Bus4* compared to *Bus1*. Further, two transient responses in the RMS voltage can be seen when the LC filter of the GFL unit is energised at $4\,\mathrm{s}$ and when the static load is connected at $6\,\mathrm{s}$. In both instances, however, the RMS voltage stays well within the voltage limit of NGESO and ELIA.
Two distinct peaks of $0.94\,\mathrm{pu}$ and $0.25\,\mathrm{pu}$ with subsequent oscillations can be identified in the current magnitude measured after the series reactor of the GFL unit when the LC filter of the GFL unit and the static load is energised. Even though the current limits are not exceeded in any of the generation units at any time, the current spike at $4\,\mathrm{s}$ is considered to be critical, as it is close to the current limit of the GFL unit. Furthermore, the interaction between the two generation units can be observed in terms of load sharing, which is described in more detail in the following when looking into their power responses.

In Figure 6.7, the frequency, active and reactive power responses of the *STATCOM-BESS* along with the GFL unit are shown.

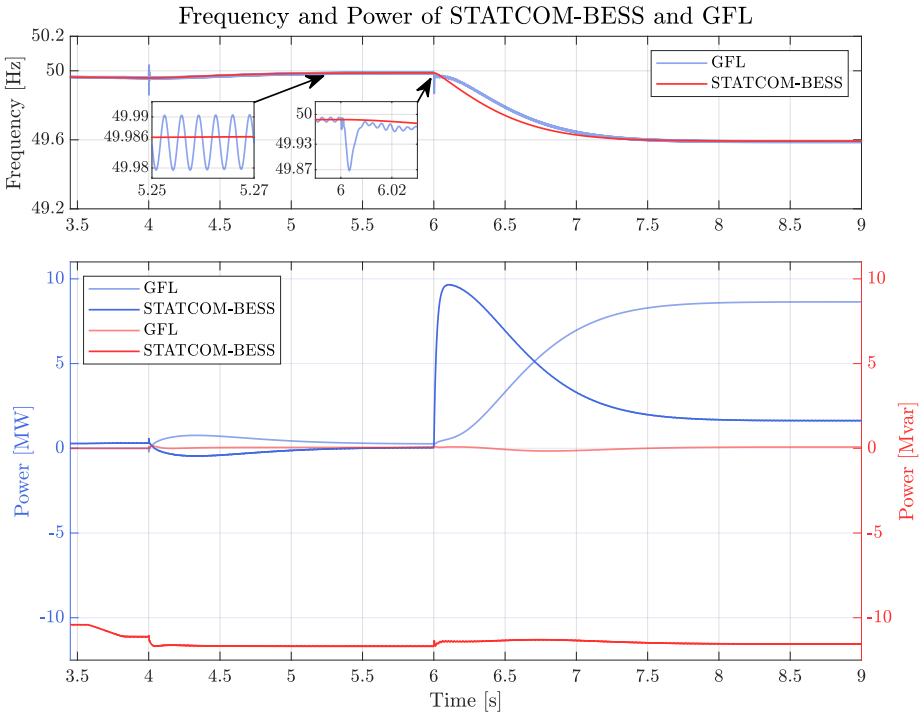

Figure 6.7: Frequency response of the *STATCOM-BESS* along with estimated frequency of the PLL of the GFL unit before any signal filtering (top subfigure). Active and reactive power responses of the *STATCOM-BESS* and the GFL unit during the energisation of the GFL unit itself and static load (bottom subfigure).

The first subfigure shows the frequency set by the *STATCOM-BESS* along with the estimated frequency of the PLL before any signal filtering. The transient responses in the voltage shown in Figure 6.6 lead to disturbances at $4\,\mathrm{s}$ and $6\,\mathrm{s}$ in the frequency estimation of the PLL with a maximum deviation from the frequency of the *STATCOM-BESS* of $\pm 0.15\,\mathrm{Hz}$. In addition, steady-state ripples of about $11\,\mathrm{mHz}$ can be detected as shown in the zoom-in figure, but these are within the measurement uncertainty of $\pm 10\,\mathrm{mHz}$ of the IEC 61000-4-30 standard [59]. However, these disturbances do not fully affect the generation of the reference value of the active power in the GFL unit, as the frequency estimation is filtered by a MAF and the resulting active power reference by a LPF. The effect of these implemented filters in the f-P droop control of the GFL unit is further demonstrated in Figure E.1 in Appendix E.2.

The active and reactive power response of the *STATCOM-BESS* along with the GFL unit are shown in the lower subfigure. It can be seen that the GFL unit when connected at $4\,\mathrm{s}$, responds to the frequency difference of $50\,\mathrm{Hz}$ and the estimated frequency, resulting in an initial increase up to $0.76\,\mathrm{MW}$ at around $4.3\,\mathrm{s}$. It is to be noted that the smooth and inert increase is shaped by the time constant of $20\,\mathrm{ms}$ used for the power measurement in PSCAD and the LPF in the f-P droop control of the GFL unit. The *STATCOM-BESS* reacts accordingly to this increase by absorbing the surplus of active power, which leads the frequency *STATCOM-BESS* moving back towards $50\,\mathrm{Hz}$. However, due to the inert frequency response caused by the swing equation implemented in the *STATCOM-BESS*,

its frequency increases only slowly, so that the GFL unit reacts to this by gradually reducing its active power output in return. This leads to the *STATCOM-BESS* not reaching a frequency above $50\,\mathrm{Hz}$, as it would be when active power is absorbed for a longer duration. Instead, through the described active power response of the GFL unit the frequency set by the *STATCOM-BESS* levelling off around $49.99\,\mathrm{Hz}$. This ultimately leads to an active power output of the GFL unit of $0.25\,\mathrm{MW}$ at around $5.5\,\mathrm{s}$ and thus to a de-loading of the *STATCOM-BESS*.
When the static load is connected, the *STATCOM-BESS* provides a fast active power response to the load change, resulting in a decreasing frequency of the *STATCOM-BESS*, as shown in the upper subfigure. The GFL unit reacts to the dropping frequency by increasing its active power output accordingly. This interaction between the generation units leads to a de-loading of the *STATCOM-BESS* through its reduced active power output. While any active power support from the GFL unit reduces the drop in frequency, the GFL unit provides the majority of active power due to its characteristic, which provides higher active power output per Hz than the active-power-frequency characteristic of the *STATCOM-BESS*. This response of the GFL unit limits the frequency drop of the *STATCOM-BESS* to about $49.59\,\mathrm{Hz}$. This value corresponds to the highest frequency deviation from $50\,\mathrm{Hz}$ during the observed period, however, the frequency limits of NGESO and ELIA are not violated.
The reactive power output of the GFL unit remains close to zero due to the low voltage deviation of $1\,\mathrm{pu}$ in the observed period, while the *STATCOM-BESS* takes over the majority of the reactive power management in the system. The active power, reactive power and the frequency response of the *STATCOM-BESS* during the block loading with and without the GFL unit connected are further investigated in Figure E.2 in Appendix E.2.

6.3 Block Loading with GFL unit and Dynamic Load

In the second test, the block loading capability of the *STATCOM-BESS* is further investigated by connecting the dynamic load model as introduced in Section 6.1 to the distribution grid instantaneously at 6 s. Therefore, the chronological energisation steps and the success criteria presented in Section 6.2 are followed.

In Figure 6.8, the RMS voltage and the current magnitudes will be investigated, to check for violations of the defined success criteria.

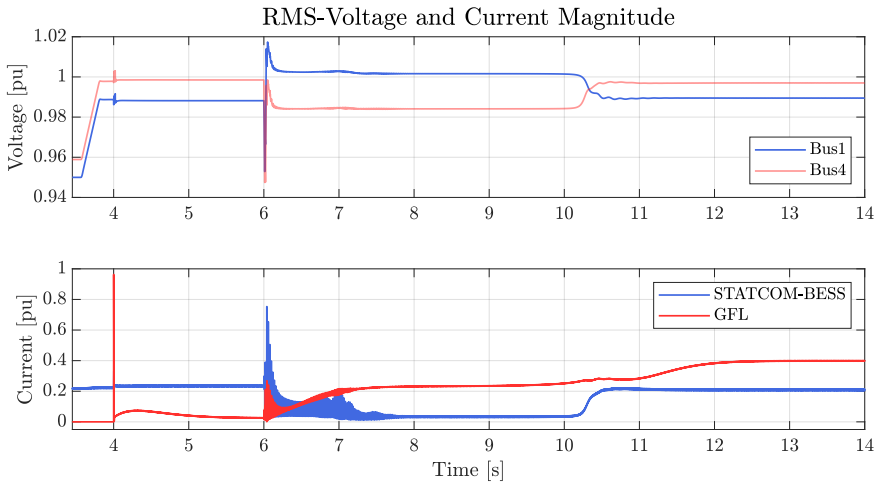

Figure 6.8: Response of current magnitude of the *STATCOM-BESS* and GFL unit measured after their series reactor as well as the line-to-line RMS value at *Bus1* and *Bus4*. Note that the current magnitude is calculated using the α-β reference frame: $|i_{meas}| = \sqrt{i_\alpha^2 + i_\beta^2}$.

In the above figure, the observations until 6 s are identical to the static load in the section 6.2 due to the same energisation sequences. At 6 s, breaker *BRK6* closes and the dynamic load model is energised. In the initial moment of the motor start-up, the RMS voltages drop significantly to around 0.95 pu, followed by a change in polarity of the voltage difference between *Bus1* and *Bus4*. The change is caused by a change in reactive power flow due to the induction motor as shown in Figure 6.5. It can be seen that when the acceleration period of the motor load is finished, the reactive power demand reduces accordingly, which causes the voltage at *Bus1* to be higher again than at *Bus4*. Overall no violation of the voltage limits specified by NGESO and ELIA can be detected.
In the subfigure showing the current magnitude, high current spikes slightly after 6 s can be observed, which are slightly delayed to the motor current seen in Figure 6.5. This correlates with the transient response of the RMS voltage in the first subfigure. Further investigations have shown that the current of the *STATCOM-BESS* is superimposed by disturbances caused by passive components. In the following, oscillations caused by the acceleration of the induction motor can be seen. At 10 s, the current magnitude of *STATCOM-BESS* and GFL unit increase to cover the load demand of the passive components of the system and the induction motor.

The active and reactive power response of the *STATCOM-BESS* and GFL unit can be seen in Figure 6.9. Furthermore, their frequency responses are shown.

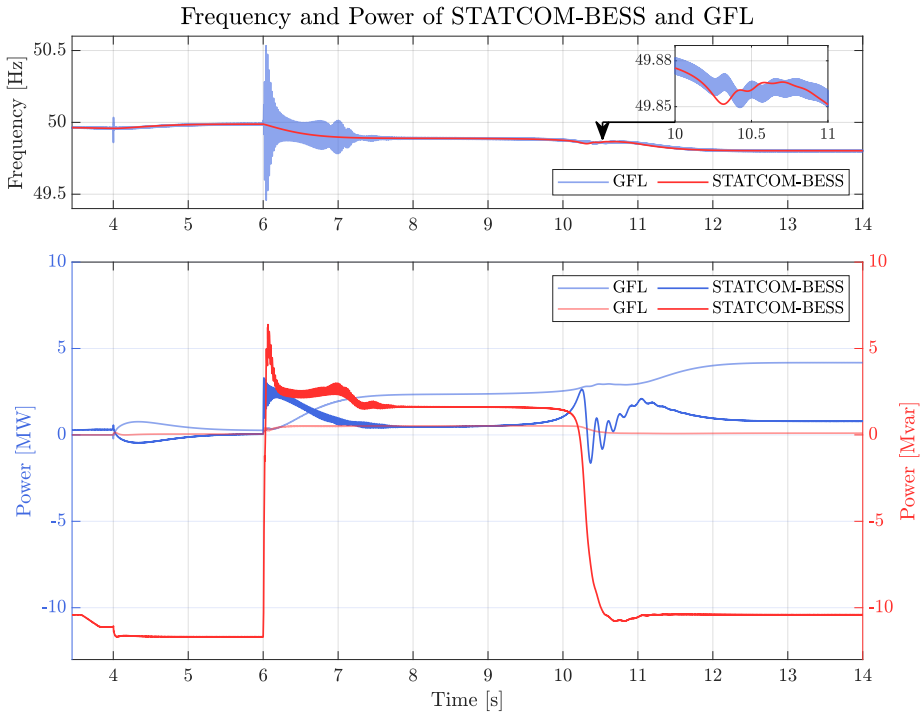

Figure 6.9: Frequency response of the *STATCOM-BESS* along with the estimated frequency of the PLL of the GFL unit before any signal filtering (top subfigure). Active and reactive power responses of the *STATCOM-BESS* and the GFL unit during the energisation of the GFL unit itself and the dynamic load model (bottom subfigure).

The frequency response of the *STATCOM-BESS* and the GFL unit can be seen in the upper subfigure. The *STATCOM-BESS* sets the frequency according to its active power output, however, it can be seen that the implemented swing equation allows it to provide a smooth frequency despite oscillations in its active power output. This is particularly visible after 6 s and after 10.2 s when strong oscillations in active power occur due to the characteristic of the induction motor as shown in Figure 6.5. However, this results in only minor oscillations in the frequency of the *STATCOM-BESS*. For the latter instance, this can be seen in the zoom-in in the first subfigure. This behaviour contributes to the overall system stability, as the GFL unit reacts accordingly to deviations of the system frequency from 50 Hz with its f-P droop control.
In comparison, the frequency estimation of the PLL within the GFL unit shows comparatively large deviations, reaching more than 49.5 Hz to 50.5 Hz between 6 s and 8 s. This is due to the frequency estimation of the PLL being exposed to the disturbances of the voltage measurement at *Bus4* shown in Figure 6.8.
The bottom subfigure shows the active and reactive power response of the *STATCOM-BESS* and the GFL unit. At 6 s, the dynamic load model is connected. It can be seen, that

the reactive power demand during the acceleration of the induction motor is majorly covered by the *STATCOM-BESS*. Notable is also that the induction motor and its high demand for reactive power during its acceleration compensate for the reactive power provided by the overhead line *OHL50*. The seen behaviour of high reactive power demand of the induction motor results in the *STATCOM-BESS* providing reactive power during the acceleration period of the induction motor. Moreover, it can be observed that the demand for reactive power during the acceleration of the induction motor is a multiple of the consumed active power and is caused by the high start-up currents drawn by the induction motor as shown in Figure 6.5. At around $10.2\,\mathrm{s}$, the reactive power drops to around $-10\,\mathrm{Mvar}$ due to the motor reducing its demand for reactive power. The oscillations in electrical torque seen in Figure 6.5 cause the oscillations in active power from $10.2\,\mathrm{s}$, that are mostly covered by the *STATCOM-BESS*, while the active power output of the GFL unit fluctuates very little due to the smooth frequency output of the *STATCOM-BESS*. The oscillation of the electrical torque and the associated operation of the induction motor in the generator region is also the reason for the temporary negative active power output of the *STATCOM-BESS*.
With the increase of mechanical load torque at $10.5\,\mathrm{s}$ shown in Figure 6.5, the consumed active power of the motor increases, which is initially covered by the *STATCOM-BESS* and subsequently by the GFL unit responding on the frequency drop set by the *STATCOM-BESS*. This interaction between *STATCOM-BESS* and GFL unit reduces the active power output of the *STATCOM-BESS* significantly and thus reduces its loading.
From about $13\,\mathrm{s}$, the active and reactive power outputs are steady. As described for the static load energisation, the GFL unit provides the majority of active power due to its characteristic, which provides higher active power output per Hz than the active-power-frequency characteristic of the *STATCOM-BESS*. This response of the GFL unit limits the frequency drop to about $49.8\,\mathrm{Hz}$ and stays within the requirements specified by NGESO and ELIA. For the reactive power, the *STATCOM-BESS* absorbs almost all of it provided by the overhead line *OHL50* and the capacitance of the filters. At the same time, the GFL unit has a low reactive power output due to its selected droop value and the voltage magnitude at *Bus4* being close to $1\,\mathrm{pu}$.
For a more detailed comparison of active and reactive power response of the *STATCOM-BESS*, the dynamic load test case is repeated with and without GFL unit support. It is therefore referred to Figure E.3 in the Appendix E.3.

6.3.1 Dynamic Load with Increased Share of Induction Motor

While block loading with a static load of $10\,\mathrm{MW}$ has proven successful, the same size for the dynamic load model was initially considered in the previous Section 6.3. However, during the initial testing of the dynamic load model with $10\,\mathrm{MVA}$, voltage drops and current peaks occurred that exceeded their defined limits and, in the worst case, led to instability of the simulation model. The main cause for this was high transient currents during the motor start-up, which the *STATCOM-BESS* and the GFL unit were unable to provide. To keep the ratio at 60-70 % of the induction motor within the dynamic load model, its total apparent power was reduced to $5\,\mathrm{MVA}$, as this resulted in stable system

response.
This section further investigates the influence of the dynamics of the induction motor model within the dynamic load model and its impact on the stability of the system when motor-dominated block loads are energised. Therefore, three different proportions of the induction motor are tested in this section, while keeping the total apparent power of the dynamic load model at 5 MVA. Starting from a proportion of 70 % (3.5 MVA), the proportion of the induction motor is then further increased to 75 % (3.75 MVA) and 80 % (4 MVA) of the total apparent power of the dynamic load model. The corresponding RMS voltages measured at *Bus1* and *Bus4*, as well as the current magnitudes of the *STATCOM-BESS* and GFL unit are shown in Figure 6.10.

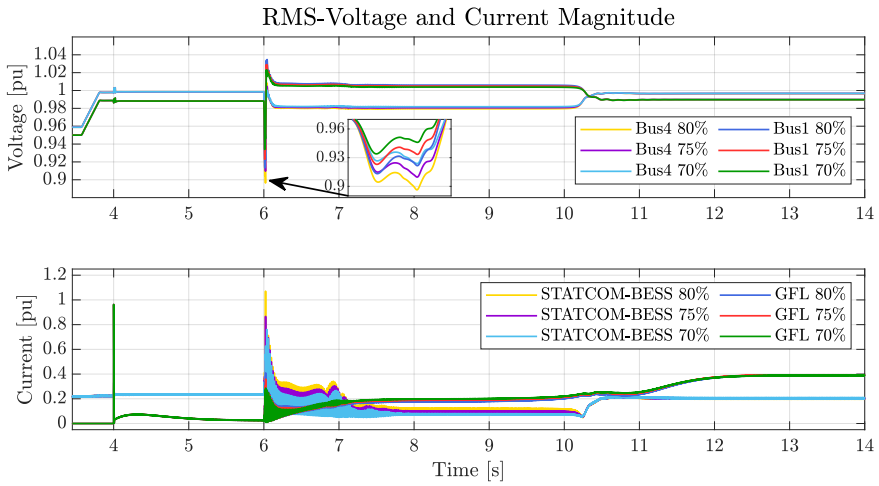

Figure 6.10: Response of current magnitude of the *STATCOM-BESS* and GFL unit measured after their series reactor as well as the line-to-line RMS value at *Bus1* and *Bus4* during the energisation of the 5 MVA dynamic load model with different proportions of the induction motor.

The figure above shows that the overall dynamics in the RMS voltage and current magnitude caused by the energisation of the induction motor are unchanged from the observations described in Section 6.3. Differences in the transient behaviour of the RMS voltage and the current magnitude can be seen, particularly at the initial moment of the energisation of the dynamic load model at around 6 s. The maximum values of the transient response of the maximum RMS voltage and current magnitude at around 6 s are presented in the following Table 6.1. Note that for the current magnitude, only the *STATCOM-BESS* is shown, as the current spikes of the GFL unit at 6 s are lower than at 13 s, when the motor is in steady state.

Table 6.1: Maximum RMS voltages at *Bus1* and *Bus4* and current magnitude of the *STATCOM-BESS*.

	$I_{max,GFM}$ [pu]	$V_{max,Bus1}$ [pu]	$V_{max,Bus4}$ [pu]
70%	0.626	0.934	0.924
75%	0.866	0.923	0.91
80%	1.07	0.913	0.896

It can be seen that, with an $80\,\%$ proportion of the induction motor, the voltage drop exceeds the limits given by NGESO, but not by ELIA. The current limit of $1.1\,\mathrm{pu}$ defined for the *STATCOM-BESS* are just maintained. With a proportion of $70\,\%$ and $75\,\%$, the voltage limits and current limits are still maintained. These voltage drops at *Bus1* and *Bus4* are caused by high starting currents of the induction motor, which consequently have to be supplied by the *STATCOM-BESS* and GFL unit.

The corresponding response of the *STATCOM-BESS* and GFL unit in power and frequency for these three proportions are shown in Figure 6.11.

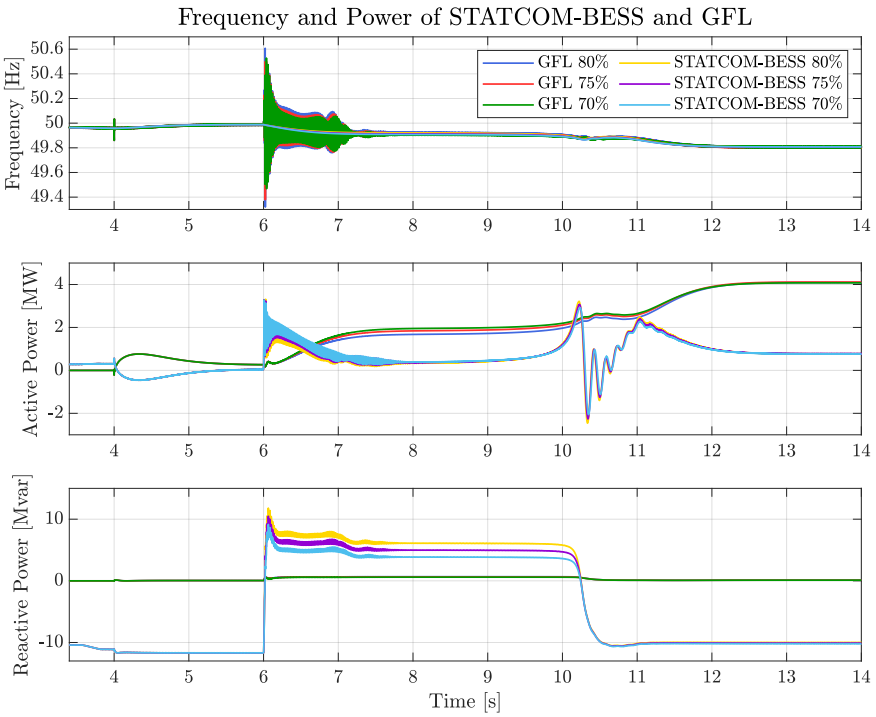

Figure 6.11: Frequency response of the *STATCOM-BESS* along with the estimated frequency of the PLL of the GFL unit before any signal filtering (top subfigure). Active and reactive power responses of the *STATCOM-BESS* and the GFL unit during the energisation of the dynamic load (second and third subfigure).

In the first subfigure, the correlation between the transient behaviour of the voltage and the frequency estimation of the PLL of the GFL unit can be seen. The increased fluctuations in the frequency estimation are a result of the more severe voltage transients caused by the current transients of the induction motor, which are proportional to the size of the induction motor. From the frequency of the *STATCOM-BESS* however, only a minimal frequency change can be observed when the proportions of the induction motor are varied, and only during the start-up of the motor between $6\,\mathrm{s}$ and $10\,\mathrm{s}$. During this period, the induction motor draws high reactive power and comparatively little active power. Increasing the proportion of the induction motor leads to a decrease in active power consumed by the dynamic load model during the start-up period. This is due to the static

load being the main consumer of active power and it is decreased with an increasing proportion of the induction motor. However, this behaviour changes at around $10.2\,\mathrm{s}$, when the motor reaches its breakdown torque and draws higher active power. The subsequent active power oscillations due to the characteristic of the induction motor as shown in Figure 6.5, are higher with a higher proportion of the induction motor. After the ramp-up of mechanical torque between $10.5\,\mathrm{s}$ and $11\,\mathrm{s}$, the motor reaches a steady state. This leads to a steady active power consumption by the dynamic load model of $5\,\mathrm{MVA}$, split between *STATCOM-BESS* and GFL unit.
In the third subfigure, the behaviour of reactive power can be observed. As only the induction motor draws reactive power within the dynamic load model, a higher percentage of induction motor increases the reactive power demand. This reactive power is mostly provided by the *STATCOM-BESS*, especially in the initial moment of connecting the dynamic load to the system at $6\,\mathrm{s}$. After the motor reaches its point of breakdown torque at around $10.2\,\mathrm{s}$, it consumes less reactive power, and the deviations between different percentages of the induction motor are not visible anymore.

6.4 Conclusion Block Loading

Based on the results of this section, it can be concluded that the final step to create a power island has been successfully completed by performing block loading of a static load with $10\,\mathrm{MW}$ to meet the required block loading capability of NGESO and ELIA. This was successfully achieved not only with a pure static load of $10\,\mathrm{MW}$ but also with a $5\,\mathrm{MVA}$ dynamic load model consisting of a $3\,\mathrm{MVA}$ induction motor. In both cases, the success criteria in terms of voltage, frequency and current limits were met at any time. Moreover, it was proven that the interaction of *STATCOM-BESS* and GFL unit as aggregated units is an effective solution to provide active power support and thus de-load the *STATCOM-BESS* during block loading.
The synchronisation of the GFL unit with its LC filter led to a temporary surplus in active power that was absorbed by the *STATCOM-BESS*. Furthermore, a high current spike occurred when connecting the GFL unit to *Bus4*. Despite not violating the limit, the spike can be considered problematic as it is close to the current limits of the GFL unit.
While the block loading of the pure static load was a comparatively smooth event with only small disturbances, issues were initially encountered with the energisation of the dynamic load model. This was due to the high currents of the induction motor during its acceleration period, which led to significant voltage drops at *Bus4* and corresponding oscillations of the frequency estimation of the PLL of the GFL unit. However, by reducing the dynamic load model to $5\,\mathrm{MVA}$, the voltage, frequency and current limits could ultimately be maintained at any time. Moreover, the maximum proportions of the induction motor within the final dynamic load model were determined to be $75\,\%$ ($5\,\mathrm{MVA}$) without violating defined current and voltage limits. This defines the boundaries for the block loading of dynamic loads in this system and emphasises the challenges with the phenomena occurring during the energisation of motor-dominated block loads. Finally, the importance of the inert frequency response of the *STATCOM-BESS* was demonstrated

under rapidly changing load conditions such as the active power oscillations after the induction motor reached its breakdown torque. This was found to be crucial for maintaining a stable active power response of the GFL unit and thus a stable interaction between the generation units.

6.5 Summary

In this section, block loading of static and dynamic loads was analysed in order to complete the creation of a power island. Initially, extensions to the system model were introduced, including the modelling of the GFL unit and the induction motor. Subsequently, the energisation of the GFL unit itself as well as the energisation of static and dynamic load models was investigated based on the limit specified by NGESO and ELIA. This also included the response and interaction of the generation units. Finally, the effects of increasing the proportion of the induction motor within the dynamic load model were analysed.

7 Discussion

In this thesis, a GFM unit with black start capability was built, and a transmission system and block loads were energised. Furthermore, the system was enhanced with a GFL unit to support the *STATCOM-BESS* during block loading. This chapter focuses on some specific decisions made to achieve the objectives stated in Chapter 3 and their impact on certain results shall here be further discussed:

- **Overhead line *OHL50*:** The overhead line is based on a PSCAD model for a wind park connected to a $33\,\mathrm{kV}$ distribution line [37]. While the voltage level of the overhead line was raised to $220\,\mathrm{kV}$ for this project, the size of the tower and the line-to-line distance of $1\,\mathrm{m}$ were left unchanged. This leads to a comparatively high capacitance of the overhead line and therefore to the high reactive power provision observed. With a more realistic line-to-line distance of around $3.5\,\mathrm{m}$ as stated in [66], the capacitance and reactive power provision of the overhead line *OHL50* would decrease.

- **Mitigation techniques:** For the transmission system energisation till *Bus4*, mitigation techniques such as reduced system voltage and PIRs have been proven to reduce inrush currents sufficiently. While the PIR and the tap changers could be implemented straightforwardly in PSCAD, it can not be guaranteed that they are available in real-life applications. Without any mitigation techniques, the requirements set by NGESO could not be fulfilled in this project and other solutions would have to be found and tested.

- **Position and design of the GFL unit:** In Chapter 6, a GFL unit was modelled and connected to *Bus4* in the PSCAD simulation model. The position was chosen to have a more comprehensive *Stage 2* of the restoration process with block loading and a local power supply that de-loads the *STATCOM-BESS*. Furthermore, with connecting the GFL unit to *Bus4*, it was not necessary to repeat the elaborate energisation steps covered in Chapter 5. When connecting a GFL based OWPP system to *Bus1*, the time-demanding energisation of the transmission system would have had to be repeated to investigate the response of the modified system.

- **Battery Size and weather dependency of the GFL unit:** To support the *STATCOM-BESS* during block loading and beyond, an ideal GFL unit without any weather dependency was modelled. As shown for the block loading of a static load in Figure

6.7, the *STATCOM-BESS* has to provide $1.63\,\mathrm{MW}$ in steady state, while the remaining power demand is covered by the GFL unit. For a resilience of supply of $72\,\mathrm{h}$ as demanded by NGESO, the battery of the *STATCOM-BESS* would need a minimum capacity of $117.4\,\mathrm{MWh}$ to cover the total resilience of supply period. This amount of battery storage is immense as the currently largest battery storage system in Europe has a storage capacity of $198\,\mathrm{MWh}$ [67] and considering that an ideal GFL unit without power fluctuation was used. When using GFL based VREs to support system energisation, nominal power can not be provided at all times due to weather dependencies, which would require an even bigger battery storage. This leaves out an important consideration for the evaluation of the provided black start service with aggregated units and resilience of supply in this project.

8 Conclusion

The main focus of this project was the application of a STATCOM with an integrated battery storage system for black start services following the requirements specified by NGESO and ELIA. The development and implementation of such non-traditional black start service providers are of utmost importance for restoring normal operation of future power systems after blackouts without relying on conventional power plants with synchronous generators. Therefore, a GFM based *STATCOM-BESS* was modelled and its performance and the corresponding system response were investigated when creating a power island after a blackout. This was realised by re-energising segments of a transmission system and subsequently a distribution network including GFL and load units. The key findings and conclusions of this project are highlighted in the following.

Transmission System Energisation
The energisation of the modelled system til *Bus4* was initially done with an ideal voltage source and afterwards with the developed *STATCOM-BESS* as the black start service provider. This energisation step refers to Chapter 5.

- **Soft-Charging:** The voltage ramp for the energisation of the LC filter and *Transformer 1* has proven to be an effective method to reduce magnetisation currents and the overall disturbance level for this energisation step.
- **Need of Mitigation Techniques:** During the energisation of the overhead line and *Transformer 2* through hard switching, various disturbance phenomena were encountered with the most challenging being inrush currents. As a result of the inrush currents that exceeded defined current limits, PIRs and reduced system voltage were indispensable mitigation techniques for the successful transmission system energisation in this project.
- **Harmonic Analysis:** The inrush currents occurring especially when energising *Transformer 2* were additionally superimposed by time-varying low-order harmonics. These low-order harmonics were investigated by applying Short-Time Fourier Transform (STFT) and spectrograms, which have been proven useful in analysing and representing the amplitudes of the frequency components over time.

Overall, the passive components in the system were successfully energised up to *Bus4*, both by the developed GFM controller of the *STATCOM-BESS* and by the ideal voltage

source. The encountered level of disturbances during the energisation of the transmission system, as seen in Chapter 5, allows the conclusion that the *STATCOM-BESS* counteracts arising disturbances better than the rigid voltage source. However, in both cases, corresponding success criteria, specifically the RMS voltage limits of $\pm 10\,\%$ around the nominal voltage defined by NGESO and the current limits of $1.1\,\mathrm{pu}$ of the *STATCOM-BESS*, were met at any time.

Block Loading
For completing the process of establishing a power island and to fulfil the required block load capability of NGESO and ELIA, a static load of $10\,\mathrm{MW}$ was instantaneously connected to the distribution level in Chapter 6. Expanding upon the block loading of the static load, a dynamic load model of $5\,\mathrm{MVA}$ with a proportion of $60\,\%$ induction motor was energised, whereby the proportion of the induction motor was subsequently increased to up to $80\,\%$.

- **Energisation GFL unit:** The connection of the GFL unit including its LC filter to *Bus4* led to a significant current transient response at the moment of energisation. During the energisation process, these transients almost reached the nominal current of the GFL unit and must be considered when including generation units and their passive components.
- **Interaction of *STATCOM-BESS* and GFL unit:** The interaction of *STATCOM-BESS* and GFL unit during the block loading of the static and the dynamic load model is considered as a promising approach to support and thus de-load the *STATCOM-BESS*. It can be concluded that the fast power and inert frequency response of the *STATCOM-BESS* enables the integration of other GFL units without the need for communication. Beyond that, this characteristic is crucial for the overall system stability, as it ensures stable active power response of the GFL unit.
- **Energisation Static Load:** From the simulation results obtained in Section 6.2, it can be concluded that the block loading of the static load of $10\,\mathrm{MW}$ poses a comparatively smooth event with only small disturbances.
- **Energisation Induction Motor:** The energisation of the induction motor led to significant transient currents in the moment of energisation, resulting in voltage disturbances at *Bus4* and corresponding oscillations in the frequency estimation of the PLL within the GFL unit. This behaviour limited ultimately the size of the induction motor due to violation of the current and voltage limits. The acceleration period of the induction motor can therefore considered to be the decisive period for the success of this energisation step.

Overall, compliance with the voltage limits of $\pm 10\,\%$ around the nominal voltage, the frequency limits of $47.5\,\mathrm{Hz}$ and $51.5\,\mathrm{Hz}$, and the current limits of $1.1\,\mathrm{pu}$ were maintained at any time during the block loading. Consequently, this also includes compliance with

the black start requirements specified by the NGESO and ELIA. In conclusion, this proves the suitability of the *STATCOM-BESS* and the GFL unit to work as aggregated units to cover instantaneous connected block loads, which ultimately leads to the formation of a power island and thus to the full completion of *Stage 2*.

9 Future work

During this thesis, the main focus was on the implementation of control structures for the *STATCOM-BESS* and the GFL unit, the energisation of the transmission system and the block loading of the static and dynamic load. Comprehensive work was done to achieve successful system energisation, which resulted ultimately in establishing a power island. However, delimitations had to be made to maintain the focus on these topics, and some results showed possibilities for improvement and expansions. To address these, the following points can be further investigated:

- **Further restoration stages:** In Section 2.1.1, different restoration stages were discussed. This project focuses only on *Stage 2*, creating a power island with load and generation units connected to a distribution system. Future work could model an OWPP system connected to *Bus1* and investigate its energisation (*Stage 1*). In addition, the energised power island could be synchronised with other power islands (*Stage 3*) to investigate the interaction with other GFM units.
- **Tuning of the controllers:** Unstable responses of the GFM controllers in PSCAD were encountered when using MATLAB to determine their control parameters by applying a step response test as described in Section 4.2. As a result, the outer voltage control loop had to be made significantly slower than the desired factor of 10 compared to the inner current control loop, to obtain stable controller responses in PSCAD. A comparable behaviour was experienced with the GFL unit when comparing the response of the power and current control loop in MATLAB. The cause of this could not be determined and should be investigated further.
- **Comparison of different GFM control structures:** In this project, the modelled GFM controller is based on a VSM control structure. However, all GFM control structures presented in section 2.2.2 are characterised by their black start capability. Different control structures could be modelled in the *STATCOM-BESS* and compared in future work.
- **Transformer investigations:** During system energisation, the relationship between inrush currents and magnetisation currents was analysed and a harmonic investigation was performed in Chapter 5. As the harmonic components of the inrush currents in Section D.3 could not be properly allocated to the magnetisation currents of the unloaded *Transformer 2*, for future work, the transformer model from

PSCAD used in this thesis needs to be further investigated. This is also required to understand the incomprehensible high magnetisation currents compared to the currents measured at the transformer terminals, observed in Chapter 5.2.

Expansion of the Dynamic Load Model

While the implementation of one single induction motor was interesting for gaining an understanding of dynamic load behaviour, its DOL start-up caused high current transients. These current transients required a reduction in motor size for the further stable operation of the *STATCOM-BESS*. As these current transients in the initial moment of the motor start-up were decisive for the success of this energisation step, thoughts have been put into how to provide different dynamic load models, as the applied motor size of 3 MVA might not accurately represent a realistic scenario as stated in Section 6.1.
To demonstrate the effect on the current transients when applying different load models of the same size and motor proportion, a dynamic load with two 1.5 MVA induction motors *M1* and *M2* is touched upon. These motors are started with a slight time shift of 10 ms. A comparison of the current transients with one 3 MVA or two 1.5 MVA induction motors is shown in the following figure.

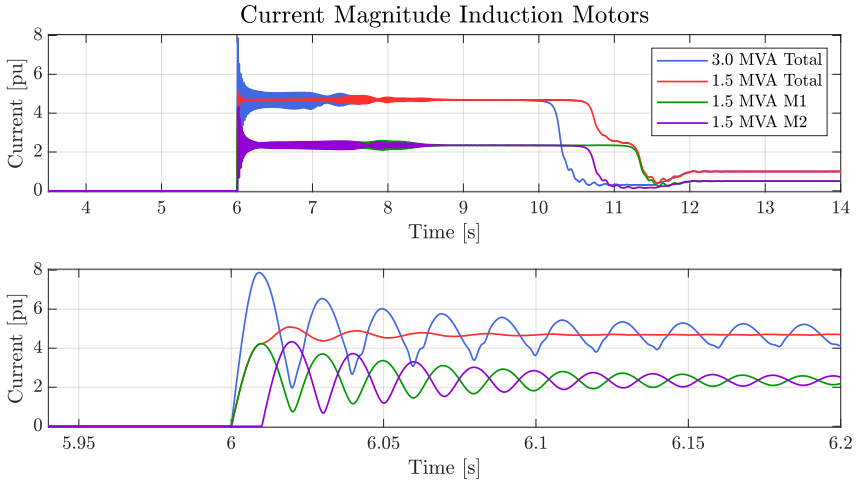

Figure 9.1: The blue line shows the current magnitude of a 3 MVA induction motor. In contrast, the red line shows the combined current magnitude of the two 1.5 MVA induction motors *M1* and *M2*. The start-up of motor *M2* is 10 ms delayed, leading to a phase shift of 180 ° and a damping of the high current spikes. Note that 1 pu represents the motor magnitude current of 74.2 A, measured at the motor terminal.

While the total current magnitude of the two 1.5 MVA motors during start-up is still a multiple of the current drawn at nominal speed, the current spikes at the terminal of the dynamic load are reduced. Therefore, it can be shown that two 1.5 MVA induction motors with slightly shifted starting times reduce the transient currents and allow the energisation of bigger dynamic loads. The results have demonstrated the need for future work in research and testing of different dynamic load models, to investigate which size and composition are still acceptable for a successful block loading process. Furthermore, the application of mitigation techniques for induction motors such as star-delta and soft starting can be investigated, to avoid DOL and reduce current and voltage disturbances.

References

[1] Eremia Mircea and Shahidehpour Mohammad, "HANDBOOK OF ELECTRICAL POWER SYSTEM DYNAMICS", Tech. Rep., 2013. [Online]. Available: https://onlinelibrary.wiley.com/doi/.

[2] G. Fotis, V. Vita, and T. I. Maris, "Risks in the European Transmission System and a Novel Restoration Strategy for a Power System after a Major Blackout", *Applied Sciences (Switzerland)*, vol. 13, no. 1, Jan. 2023.

[3] Stankovski Andrej, Gjorgiev Blazhe, Locher Leon, and Sansavini Giovanni, "Power Blackouts Europe: Analyses, key insights, and recommendations from empirical evidence", 2023.

[4] Energinet, "Power outage on Bornholm on Monday morning", 2022. [Online]. Available: https://en.energinet.dk/About-our-news/News/2022/10/10/Bornholm-power-outage/ (visited on 02/01/2024).

[5] Keith Bell, *What happened on August 9th – the investigations*, 2020. [Online]. Available: https://ukerc.ac.uk/news/august-9-investigations/ (visited on 02/01/2024).

[6] ofgem, "9 August 2019 power outage report", 2020. [Online]. Available: https://www.ofgem.gov.uk/sites/default/files/docs/2020/01/9_august_2019_power_outage_report.pdf (visited on 02/02/2024).

[7] S Almeida De Graaff, "Power system restoration-World practices & future trends Country Approach Blackstart: Top-down Blackstart: Bottom-up", Tech. Rep., 2019.

[8] Pagnani Daniela, "Design and Integration of Black-Start Service Provision by Offshore Wind Farms: To Assure Resilience in 100%-Renewable-based Future Power Systems", Ph.D. dissertation, Aalborg University, 2023. [Online]. Available: https://vbn.aau.dk/en/publications/design-and-integration-of-black-start-service-provision-by-offsho.

[9] NationalGridESO, "NGESO Black Start from Non-Traditional Generation Technologies", Tech. Rep., 2019. [Online]. Available: https://www.nationalgrideso.com/document/148201/download.

[10] ESO, "Future Energy Scenarios", Tech. Rep., 2023. [Online]. Available: www.nationalgrideso.com/future-energy/future-energy-scenarios.

[11] National Grid ESO, "Black Start from Distributed Sources - System Operability Framework", Tech. Rep., 2017.

[12] ENTSO-E, "P5-Policy 5: Emergency Operations Document Control Chapters", Tech. Rep., 2017.

[13] B. Badrzadeh, *Power system restoration accounting for a rapidly changing power system and generation mix Power system operation and control C2 TECHNICAL BROCHURES*. 2023.

[14] ELIA, "REVIEW OF BLACK START ANCILLARY SERVICES ELIA-National Control Center & Market Development", Tech. Rep., 2018.

[15] D. Pagnam, L. H. Kocewiak, J. Hjerrild, F. Blaabjerg, and C. L. Bak, "Overview of Black Start Provision by Offshore Wind Farms", in *IECON Proceedings (Industrial Electronics Conference)*, vol. 2020-October, IEEE Computer Society, Oct. 2020, pp. 1892–1898.

[16] National Grid ESO, "Black Start from Non-Traditional Generation Technologies - Power Island Strength and Stability in support of Black Start", Tech. Rep., 2019.

[17] D. Pagnani, Kocewiak, J. Hjerrild, F. Blaabjerg, and C. L. Bak, "Integrating black start capabilities into offshore wind farms by grid-forming batteries", *IET Renewable Power Generation*, vol. 17, no. 14, pp. 3523–3535, Oct. 2023.

[18] D. Pagnani, L. Kocewiak, J. Hjerrild, F. Blaabjerg, and C. L. Bak, "Challenges and Solutions in Integrating Black Start into Offshore Wind Farms", Tech. Rep., 2020.

[19] National Grid ESO, "Wind Tender Technical Requirements & Assessment Criteria", Tech. Rep., 2022.

[20] ELIA, "DESIGN NOTE ON RESTORATION SERVICES ELIA", Tech. Rep., 2018. [Online]. Available: `https://www.elia.be/en/electricity-market-and-system/system-services/re-energizing-after-a-black-out`.

[21] National Grid ESO, *Grid Code, Issue 6, Revision 21, 4 March 2024*, Mar. 2024. [Online]. Available: `https://www.nationalgrideso.com/document/287271/download`.

[22] NationalGridESO, "Black Start from Non-Traditional GenerationTechnologies - Case study: Wind variability", Tech. Rep., 2019.

[23] W. Sang, W. Guo, S. Dai, C. Tian, S. Yu, and Y. Teng, *Virtual Synchronous Generator, a Comprehensive Overview*, Sep. 2022.

[24] S. K. Chaudhary, R. Teodorescu, J. R. Svensson, L. H. Kocewiak, P. Johnson, and B. Berggren, "Black Start Service from Offshore Wind Power Plant using IBESS", in *2021 IEEE Madrid PowerTech, PowerTech 2021 - Conference Proceedings*, Institute of Electrical and Electronics Engineers Inc., Jun. 2021.

[25] D. Pagnani, F. Blaabjerg, C. L. Bak, F. M. F. Da Silva, H. Kocewiak, and J. Hjerrild, "Offshore wind farm black start service integration: Review and outlook of ongoing research", *Energies*, vol. 13, no. 23, Dec. 2020.

[26] J. Rocabert, A. Luna, F. Blaabjerg, and P. Rodríguez, "Control of power converters in AC microgrids", *IEEE Transactions on Power Electronics*, vol. 27, no. 11, pp. 4734–4749, 2012.

[27] R. Rosso, X. Wang, M. Liserre, X. Lu, and S. Engelken, *Grid-Forming Converters: Control Approaches, Grid-Synchronization, and Future Trends - A Review*, 2021.

[28] D. B. Rathnayake, M. Akrami, C. Phurailatpam, *et al.*, "Grid Forming Inverter Modeling, Control, and Applications", *IEEE Access*, vol. 9, pp. 114 781–114 807, 2021.

[29] ENTSO-E Technical Group on High Penetration of Power Electronic Interfaced Power Sources, "High Penetration of Power Electronic Interfaced Power Sources and the Potential Contribution of Grid Forming Converters - Technical Report", Tech. Rep., 2019. [Online]. Available: www.entsoe.eu.

[30] A. Jain, J. N. Sakamuri, and N. A. Cutululis, "Grid-forming control strategies for black start by offshore wind power plants", *Wind Energy Science*, vol. 5, no. 4, pp. 1297–1313, Oct. 2020.

[31] A. Alassi, "Black-Start Provision from Grid-Forming Converters: A New Network Restoration Paradigm", Tech. Rep., 2023.

[32] L. Yu, R. Li, and L. Xu, "Distributed PLL-Based Control of Offshore Wind Turbines Connected with Diode-Rectifier-Based HVDC Systems", *IEEE Transactions on Power Delivery*, vol. 33, no. 3, pp. 1328–1336, Jun. 2018.

[33] T. Noguchi, H. Tomiki, S. Kondo, and I. Takahashi, "Direct Power Control of PWM Converter Without Power-Source Voltage Sensors", Tech. Rep. 3, 1998, p. 473.

[34] M. Ndreko, S. Rüberg, and W. Winter, "Grid Forming Control for Stable Power Systems with up to 100 % Inverter Based Generation: A Paradigm Scenario Using the IEEE 118-Bus System", Tech. Rep., 2018.

[35] H. Brantsaeter, L. Kocewiak, and A. R. Ardal, "Passive Filter Design and Offshore Wind Turbine modelling for system level harmonic studies", 2015.

[36] Manitoba Hydro - PSCAD, *Frequency Dependent Models*. [Online]. Available: https://www.pscad.com/webhelp/ol-help.htm#EMTDC/Transmission_Lines/Frequency_Dependent_Models.htm (visited on 03/03/2024).

[37] Manitoba Hydro - PSCAD, *Type 4 Wind Turbine Generators*, 2018. [Online]. Available: https://www.pscad.com/knowledge-base/article/227 (visited on 03/03/2024).

[38] Manitoba Hydro - PSCAD, *Adjusting Saturation Properties*. [Online]. Available: https://www.pscad.com/webhelp-v502-ol/EMTDC/Transformers/The_Classical_Approach/more_classical_tx.htm (visited on 05/29/2024).

[39] Manitoba Hydro - PSCAD, *PSCAD Application Help System: Transformers - The Classical Approach*. [Online]. Available: https://www.pscad.com/webhelp/EMTDC/Transformers/The_Classical_Approach/the_classical_approach.htm (visited on 03/03/2024).

[40] S. Ghimire, K. V. Kkuni, S. C. Jakobsen, *et al.*, "Grid-Forming Control Methods for Weakly Connected Offshore WPPs", in *IET Conference Proceedings*, vol. 2023, Institution of Engineering and Technology, 2023, pp. 246–253. [Online]. Available: https://ieeexplore.ieee.org/document/10365130.

[41] S. D'Arco, J. A. Suul, and O. B. Fosso, "Automatic Tuning of Cascaded Controllers for Power Converters Using Eigenvalue Parametric Sensitivities", *IEEE Transactions on Industry Applications*, vol. 51, no. 2, pp. 1743–1753, Mar. 2015.

[42] R. Teodorescu, M. Liserre, and P. E. e. Rodriguez, *Grid converters for photovoltaic and wind power systems*. 2011, p. 398.

[43] P. Werle and H. Brendel, *Springer Handbook of Power Systems* (Springer Handbooks), 1st ed., K. O. Papailiou, Ed. Singapore: Springer Singapore, 2021, pp. 451–462. [Online]. Available: https://link.springer.com/10.1007/978-981-32-9938-2.

[44] M. Rezkalla, M. Pertl, and M. Marinelli, "Electric power system inertia: requirements, challenges and solutions", *Electrical Engineering*, vol. 100, no. 4, pp. 2677–2693, Dec. 2018.

[45] J. Dolado, J. L. Rodríguez Amenedo, S. Arnaltes, and J. Eloy-Garcia, "Improving the Inertial Response of a Grid-Forming Voltage Source Converter", *Electronics (Switzerland)*, vol. 11, no. 15, Aug. 2022.

[46] B. Bahrani, S. Kenzelmann, and A. Rufer, "Multivariable-PI-based dq current control of voltage source converters with superior axis decoupling capability", *IEEE Transactions on Industrial Electronics*, vol. 58, no. 7, pp. 3016–3026, Jul. 2011.

[47] L. Huang, C. Wu, D. Zhou, and F. Blaabjerg, "A Power-Angle-Based Adaptive Overcurrent Protection Scheme for Grid-Forming Inverter under Large Grid Disturbances", *IEEE Transactions on Industrial Electronics*, vol. 70, no. 6, pp. 5927–5936, Jun. 2023.

[48] T. Dragicevic, S. Vazquez, and P. Wheeler, "Advanced Control Methods for Power Converters in DG Systems and Microgrids", *IEEE Transactions on Industrial Electronics*, vol. 68, no. 7, pp. 5847–5862, Jul. 2021.

[49] D. Zhou and F. Blaabjerg, "Bandwidth oriented proportional-integral controller design for back-to-back power converters in DFIG wind turbine system", *IET Renewable Power Generation*, vol. 11, no. 7, pp. 941–951, Jun. 2017.

[50] T. Kerekes, "Lecture 5: Control of the Grid Side Converter - Control of Grid Connected Photovoltaic and Wind Power Systems - AAU Energy", Tech. Rep., 2023. [Online]. Available: www.energy.aau.dk.

[51] Peng Jinsheng, "Assessment of Transformer Energisation Transients and their Impacts on Power Systems", Tech. Rep., 2013.

[52] F. Faria Da Silva and C. Leth Bak, "Electromagnetic Transients in Power Cables", Tech. Rep., 2013. [Online]. Available: http://www.springer.com/series/4622.

[53] Manitoba Hydro - PSCAD, *Breaker, Faults and Timed Logic*, 2020. [Online]. Available: https://www.pscad.com/knowledge-base/article/604 (visited on 03/08/2024).

[54] H. Ito, "Cigre Green Books: Switching Equipment", Tech. Rep., 2019. [Online]. Available: http://www.springer.com/series/15209.

[55] ABB, "Live Tank Circuit Breakers - Buyer´s Guide", Tech. Rep., 2003. [Online]. Available: https://library.e.abb.com/public/92a2585c6d325c39c1257b130057b191/1HSM9543%2022-00en%20CB%20Buyers%20Guide%20Edition%202.pdf (visited on 03/14/2024).

[56] J. Panek, "Temporary Overvoltages: Causes, Effects and Evaluation", *IEEE Power Engineering Review*, vol. 10, no. 6, pp. 14–15, 1990.

[57] "DS/EN IEC 60071-1:2019 - Insulation co-ordination - Part 1: Definitions, principles and rules",

[58] National Grid, "Limits for Temporary Overvoltages in England and Wales Network", Tech. Rep., 2016.

[59] "DS/EN 61000-4-30:2015 - Electromagnetic compatibility (EMC) - Part 4-30: Testing and measurement techniques - Power quality measurement methods", Tech. Rep., 2015.

[60] I. Romero Navarro, Lunds universitet. Institutionen for industriell elektroteknik och automation., and U. Media-tr., *Dynamic load models for power systems : estimation of time-varying parameters during normal operation*. Dept. of Industrial Electrical Engineering and Automation [Institutionen for industriell elektroteknik och automation], Univ, 2002.

[61] Manitoba Hydro - PSCAD, "PSCAD Cookbook Induction Machines Study", Tech. Rep., 2020. [Online]. Available: https://www.pscad.com/knowledge-base/article/49 (visited on 05/10/2024).

[62] F. Jörg Randermann, "Starten und steuern von Drehstrom-Asynchronmotoren", Tech. Rep., 2010. [Online]. Available: www.eaton.com.

[63] R. Fischer, *Elektrische Maschinen*, 10th ed. 1999, pp. 241–242.

[64] Paul Krause, Oleg Wasynczuk, Scott Sudhoff, and Steven Pekarek, *Analysis of Electric Machinery and Drive Systems*, Third Edition, P. Krause, O. Wasynczuk, S. Sudhoff, and S. Pekarek, Eds. Wiley, Jun. 2013. [Online]. Available: https://onlinelibrary.wiley.com/doi/book/10.1002/9781118524336.

[65] A. Wahl and L. Kilgore, "Transient Starting Torques in Induction Motors", 1940.

[66] J. F. Nolasco, J. A. Jardini, and E. Ribeiro, *Overhead Lines* (CIGRE Green Books), K. O. Papailiou, Ed. Cham: Springer International Publishing, 2017. [Online]. Available: http://link.springer.com/10.1007/978-3-319-31747-2.

[67] Jack Kelly, *Harmony Energy and FRV launch Clay Tye – Europe's joint largest battery storage system by MWh*, 2024. [Online]. Available: https://harmonyenergy.co.uk/harmony-energy-and-frv-launch-clay-tye-europes-joint-largest-battery-storage-system-by-mwh/ (visited on 05/21/2024).

[68] CIGRE - Working Group C4.307, *Transformer Energization in Power Systems: A Study Guide*. CIGRE, 2014.

[69] D. Lyck, D. Chatterjee, J. K. Schwarzkopf, and O. Lukas Headley, "Decomposing Power System Harmonics Using Audio Source Separation Techniques - A Study on Application of the NMF Method MSc 2nd Semester Report", Tech. Rep., 2023. [Online]. Available: https://kbdk-aub.primo.exlibrisgroup.com/permalink/45KBDK_AUB/a7me0f/alma9921564298105762.

[70] H. Jeon, Y. Jung, S. Lee, and Y. Jung, "Area-efficient short-time fourier transform processor for time–frequency analysis of non-stationary signals", *Applied Sciences (Switzerland)*, vol. 10, no. 20, pp. 1–10, Oct. 2020.

[71] J. Arrillaga and N. R. Watson, *Power system harmonics*. J. Wiley & Sons, 2003.

[72] Manitoba Hydro - PSCAD, *2nd Order Complex Pole with Gain*, 2024. [Online]. Available: https://www.pscad.com/webhelp/Master_Library_Models/CSMF/2nd_Order_Functions/2complex.htm (visited on 05/30/2024).

A Appendix: System Data and Transformer Saturation

This appendix provides an overview of the parameters used to model the *STATCOM-BESS*, the frequency-dependent line model of the overhead line and the two transformers including an explanation of the transformer saturation.

Table A.1: Parameters used for the model of the *STATCOM-BESS* including the implemented filter.

STATCOM with integrated BESS			
Nominal apparent power	51 MVA	Nominal frequency	50 Hz
Nominal reactive power	$\pm$50 Mvar	Nominal voltage (L-L,RMS)	33 kV
Nominal active power	10 MW	Base impedance	21.4 Ω
Nominal phase current (RMS)	0.892 kA	Series reactor	3.4 mH
Nominal phase current (Peak)	1.262 kA	Shunt capacitor	7.3 μF

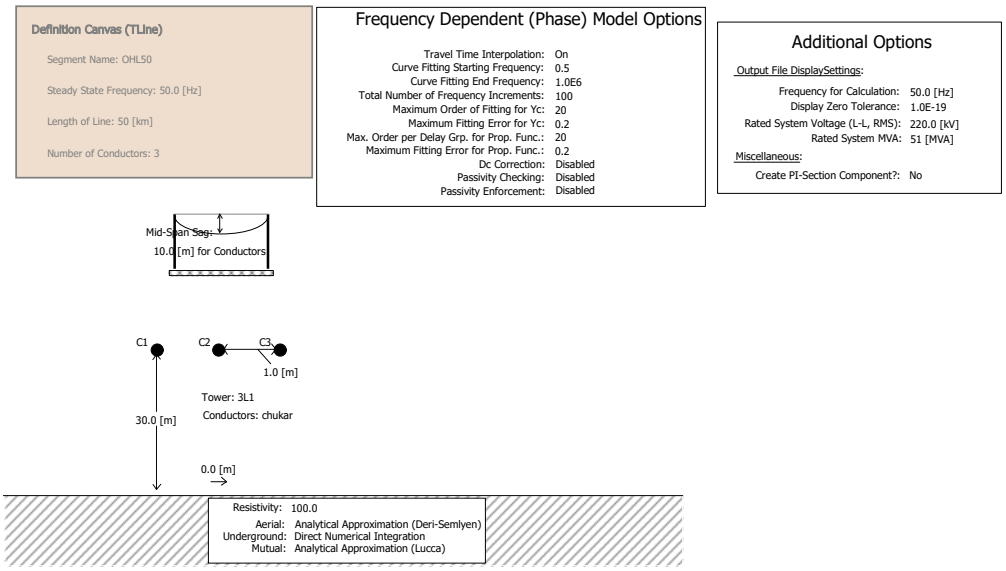

Figure A.1: Parameters used for the frequency-dependent line model of the overhead line. The data is based on [37].

```
--------------------------------------------------
 LOAD FLOW RXB FORMATTED DATA @       50.00 Hz:
--------------------------------------------------

 Base of Per-Unit Quantities : 220.00 kV (L-L)  , 51.00 MVA
 NOTE: Base values could be changed using Additional Options Component

  Positive Sequence (Long-Line Corrected)
  ...............

  Resistance      Rsq   [pu]:       0.179637608E-02
  Reactance       Xsq   [pu]:       0.144385130E-01
  Susceptance     Bsq   [pu]:       0.201072698
  Surge Impedance Zcsq  [pu]:       0.267969078

  Zero Sequence (Long-Line Corrected)
  ............

  Resistance      Rsq   [pu]:       0.926841539E-02
  Reactance       Xsq   [pu]:       0.810828364E-01
  Susceptance     Bsq   [pu]:       0.554463501E-01
  Surge Impedance Zcsq  [pu]:        1.20928310
```

Figure A.2: Line Parameters at 50 Hz used for the frequency-dependent line model of the overhead line. The data is based on [37].

Transformer Data and Saturation

As described in Section 2.1.3, inrush currents caused by transformer saturation are one of the major challenges during power system energisation. This makes it necessary to include saturation characteristics of transformers in power system restoration studies. Due to the inductive nature of the transformer in steady-state operation conditions, the magnetic flux lags the primary voltage by 90°. In steady-state, the transformer operates predominantly in the linear range of its saturation curve between the negative and positive knee points. This curve can be seen in the Figure A.3. [43]

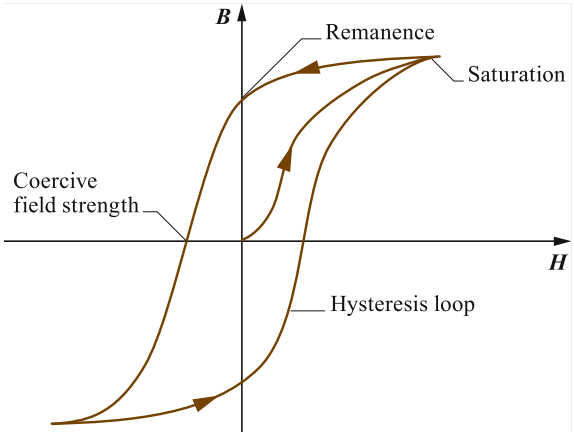

Figure A.3: Transformer hysteresis curve [43].

In an ideal scenario, where the transformer is energised exactly at the peak of the sinusoidal voltage and the transformer core has no remanence, its flux starts to increase from zero for one-fourth of a period until the voltage reaches its zero-crossing point. Under these circumstances, the iron core is operated predominantly within its linear range and

does not saturate, and therefore no inrush currents occur.[43]
However, suppose the transformer is energised at zero-crossing of the voltage. In that case, the magnetic flux increases linearly until the knee point of the hysteresis curve is reached. This happens after around one-quarter of a period, at the peak of the sinusoidal wave or shortly afterwards. After reaching the knee point, any applied voltage drives a disproportional high current, causing the transformer to go into saturation and to draw high inrush currents. [43]
When the first voltage halfwave drives the core into saturation, nearly the complete following halfwave of opposite polarity is used for desaturation. This process results in high inrush currents with a half-wave characteristic for multiple cycles, only being damped through the leakage inductance, the resistance of the primary winding and the power line [39], [43], [51].
It is also worth mentioning that the saturation of transformers is a highly non-linear phenomenon, as the resulting inrush currents are typically superimposed by a DC component and harmonics, especially even harmonics. [51], [68]

The parameters used for modelling the transformers including their saturation characteristic can be found in Table A.2.

Table A.2: Parameters used for modelling the transformers. The data is based on [37], except for the air core reactance as in [39], where it is stated that the air core reactance is typically twice as large as the leakage reactance. Also note that the same data is used for both transformers, with the high-voltage side characterised by the grounded star winding.

Transformer data			
Configuration		**Saturation**	
Nominal power	51 MVA	Place saturation on winding	Middle
Nominal frequency	50 Hz	Hysteresis	None
Nominal voltage (L-L,RMS)	33/220 kV	Remanence	None
Connection group	Ynd1	Inrush decay time constant	0.5 s
Ideal Transformer Model	Yes	Air core reactance	0.09 pu
Leakage Reatance	0.045 pu	Nominal magnetising current	2 %
Eddy current losses	0.0025 pu	Knee voltage	1.17 pu
Copper losses	0.0025 pu		

B Appendix: Initial Black Start Investigations

B.1 Basic Schematics PIR and On-load Tap Changer

Figure B.1 shows the basic schematics of an on-load tap-changer and a parallel PIR [53]. These schematics are the basis for the implementation of the corresponding mitigation techniques for the energisation process in Chapter 5.

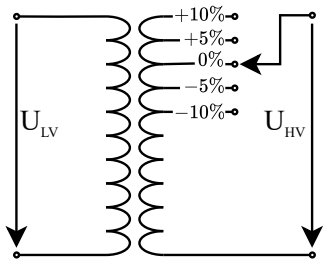

(a) Schematic on-load tap changer implemented in *Transformer 1* in the PSCAD model.

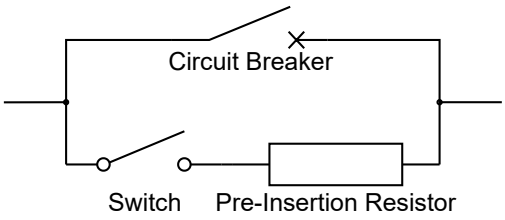

(b) Schematic of the parallel PIR used by PSCAD [53].

Figure B.1: Schematic of the implemented mitigation techniques in PSCAD to limit transient inrush currents.

B.2 Harmonic Analysis for Black Start with Voltage Source

For a better understanding of the superimposed frequency components in the currents shown in Figure 5.2 and 5.3, especially when *Transformer 2* is energised, a harmonic analysis is performed. In a previous project [69] by one of the authors, a harmonic analysis of time-varying voltage and current signals was performed using STFT and spectrograms. The STFT divides a time-domain signal into several time frames using a window function and performs a Fast Fourier Transform (FFT) in each time frame [69], [70]. The intensity or amplitude of each frequency component contained in each time frame can then be illustrated in a spectrogram. This project [69] provides the basis for the harmonic analysis carried out in this section. Therefore, the following MATLAB code based on [69] is used to run the short-time Fourier transform and to plot the spectrogram of the current signals shown in Figure 5.2 and 5.3.

```
1  %Define window length
2  WindowLength=1024;
3  %Define overlap length
4  OverlapLength=0.75*WindowLength;
5  %Define sampling frequency
6  Fs = 1/100e-6;
7
8  %Conduct STFT with defined parameters above
9  [s,f,t]=stft(I1_A,Fs,'Window',hann(WindowLength,"periodic"), ...
10 'OverlapLength',OverlapLength, 'FFTLength',Fs,FrequencyRange="onesided");
11 %Convert spectrogram complex data into current amplitudes
12 s_mag=abs(s);
13 s_mag_conv = (s_mag/(WindowLength/4));
14
15 %Plot spectrogram
16 surf(t,f,s_mag_conv,'EdgeColor','none');grid on
17 axis xy; axis tight; view(0,90);
```

The defined parameters for the *WindowLength*, *OverlapLength* and *FFTLength* are chosen according to [69] as a trade-off between a high time resolution and low spectral leakage. Note also that the total number of time frames is increased by implementing an overlap length of 75 % in the used *Hann* window. The sampling frequency *Fs* corresponds to the simulation time step set in the PSCAD simulation. The parameter *I1_A* represents the corresponding single phase current signal. The conversion of the short-time Fourier transform's output parameters *s* into the current amplitude *s_mag_conv* in lines 12 and 13 of the code above is determined experimentally and successfully validated in [69].

Using the code presented above, the following spectrograms of the output current of the voltage source are created and the effect of the tap changer and the PIR on the harmonic performances is evaluated. Figure B.2 shows the amplitudes of the frequency components contained in the output phase currents of the voltage source without applying tap changers or PIRs. Note that only low-order harmonics could be detected, which is why

the frequency range for the harmonic analysis in this section is limited to 600 Hz.

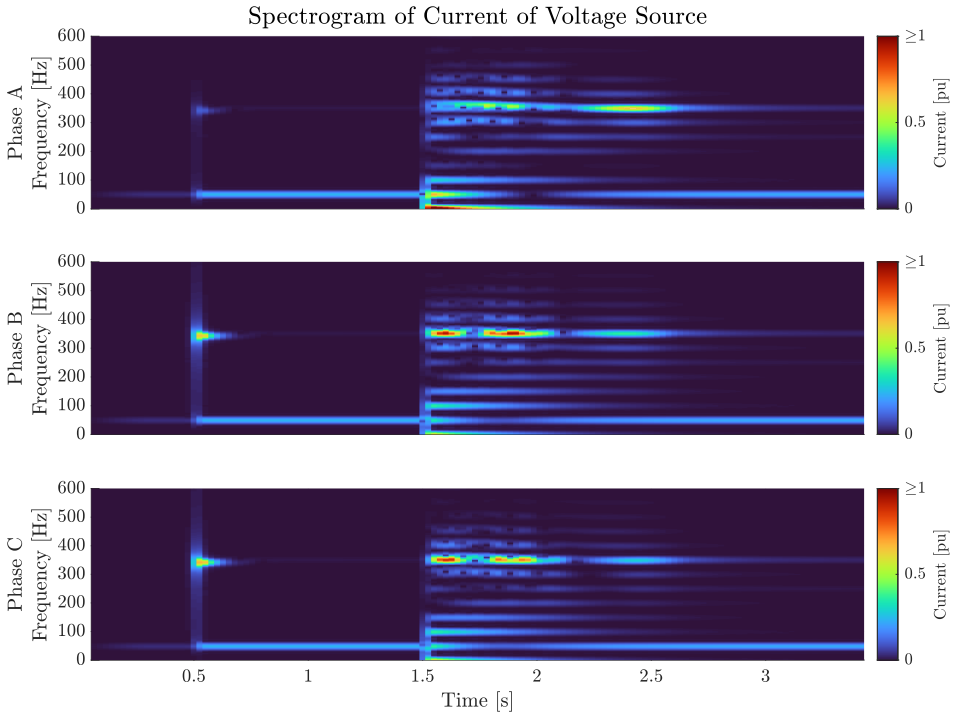

Figure B.2: Spectrogram of the amplitudes of the frequency components contained in the output current of the voltage source without tap changer in *Transformer 1* and without PIRs in *BRK2* and *BRK3*. Note that the colour bar on the right side shows the current amplitude of the frequency components, where 1 pu corresponds to the nominal phase current of 1.262 kA.

In this figure, a 7th harmonic component can be seen when the overhead line is energised, which is more prominent in Phases B and C. This 7th harmonic component is consistent with the behaviour visible in Figure 5.2. When *Transformer 2* is energised, a high DC component (0 Hz) occurs in Phase A, which is less distinct in Phase B and C. Additionally, in all phases, the fundamental component shows a dip between 1.75 s and 2 s, which is due to the strongly fluctuating decay of the current transients seen in Figure 5.2. Furthermore, harmonic orders can be seen from the 2nd to the 11th harmonic, with the 2nd and 7th harmonics having the highest amplitudes. Another notable observation is that the decay process is not uniform, especially at the 7th harmonic, where up and down swings of the amplitude can be observed.

As some of these behaviours can already be seen in Figure 5.2, the fundamental reliability of the methods used for this analysis is considered as satisfactory. However, it is also important to mention that due to the division into time frames and the overlapping through the applied windowing function by the STFT, a slight temporal mismatch between the actual presence of the harmonics in current signals and the representation in the spectrogram becomes visible, e.g. the harmonic distortion increases before the actual energisation of *Transformer 2*.

It should also be noted that the spectrogram shows spectral leakage over a wide fre-

quency range at sudden amplitude changes due to the selected windowing parameters [69]. This should also be taken into account for the following spectrograms.

Figures B.3 and B.4 show the effect on the previously identified frequency components when PIRs in the breakers *BRK2* and *BRK3* and the tap changers in *Transformer 2* are applied to attenuate the large transient currents. Note that the colour bar on the right side shows the current amplitude of the frequency components, where $1\,\mathrm{pu}$ corresponds to the nominal phase current of $1.262\,\mathrm{kA}$.

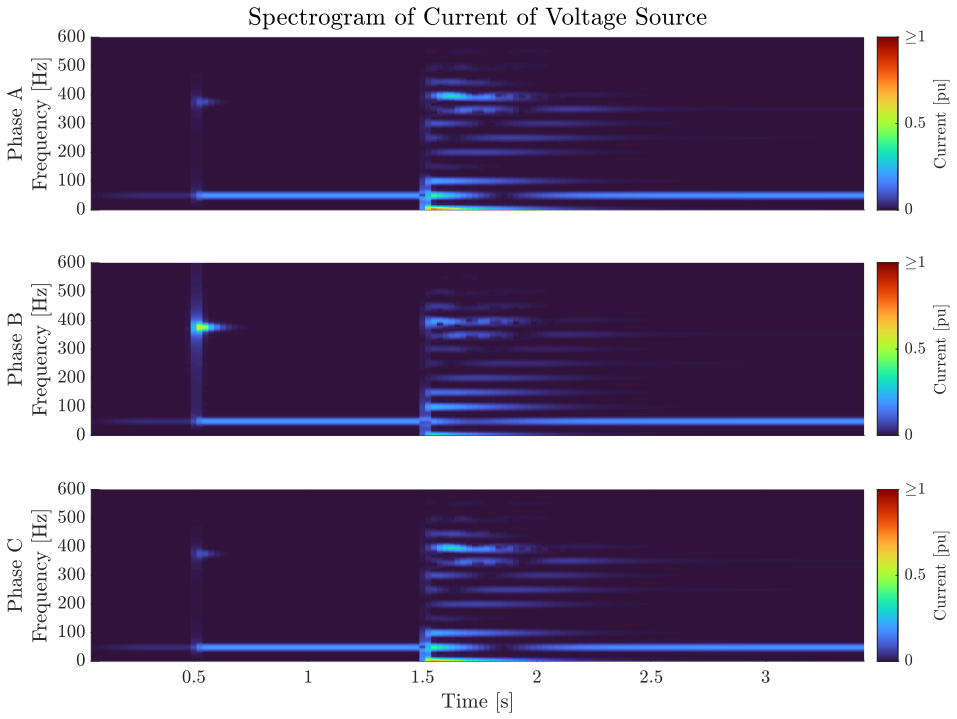

Figure B.3: Spectrogram of the amplitudes of the frequency component contained in the output current of the voltage source with tap changer in *Transformer 1* but without PIRs in *BRK2* and *BRK3*.

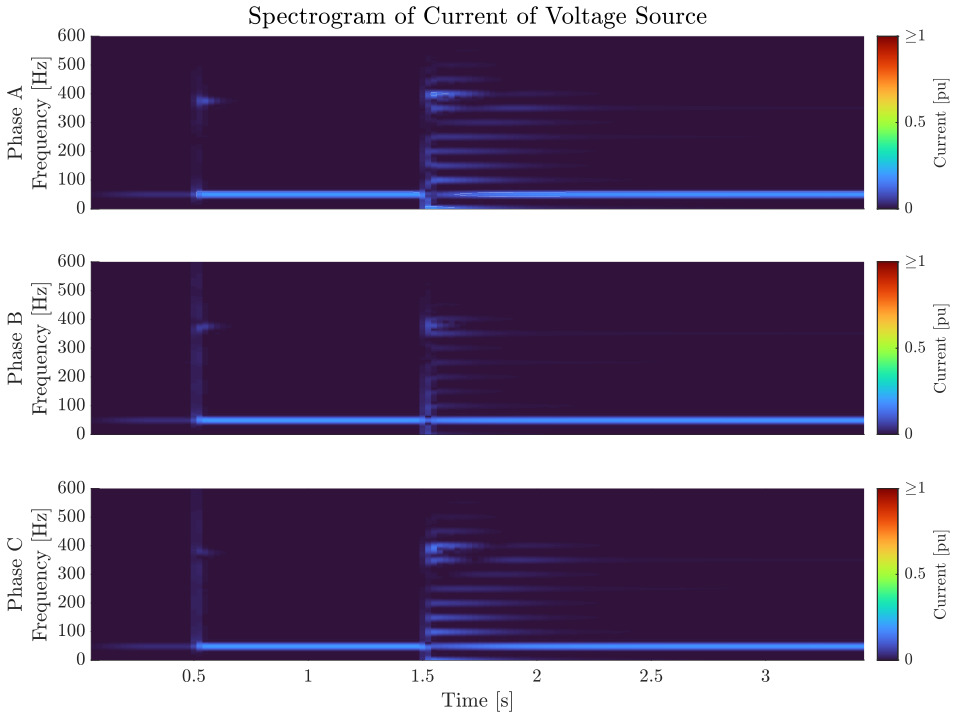

Figure B.4: Spectrogram of the amplitudes of the frequency component contained in the output current of the voltage source with tap changer in *Transformer 1* and with PIRs in *BRK2* and *BRK3*.

The figures B.3 and B.4 show that the applied mitigation techniques significantly reduce the previously identified harmonic components, including the DC component. This further demonstrates the suitability and importance of their application, even though the harmonic components including the DC component can only be damped and not eliminated.

For a further investigation of the source of the harmonic components visible in Figure B.4, the spectrogram for the magnetization currents of *Transformer 2* shown in Figure 5.9 is provided in Figure B.5. In this figure, tap changers and PIRs were applied during the simulation. Note that in this spectrogram $1\,\mathrm{pu}$ corresponds to a nominal phase current of $0.189\,\mathrm{kA}$, as the primary side of *Transformer 2* is connected to $220\,\mathrm{kV}$.

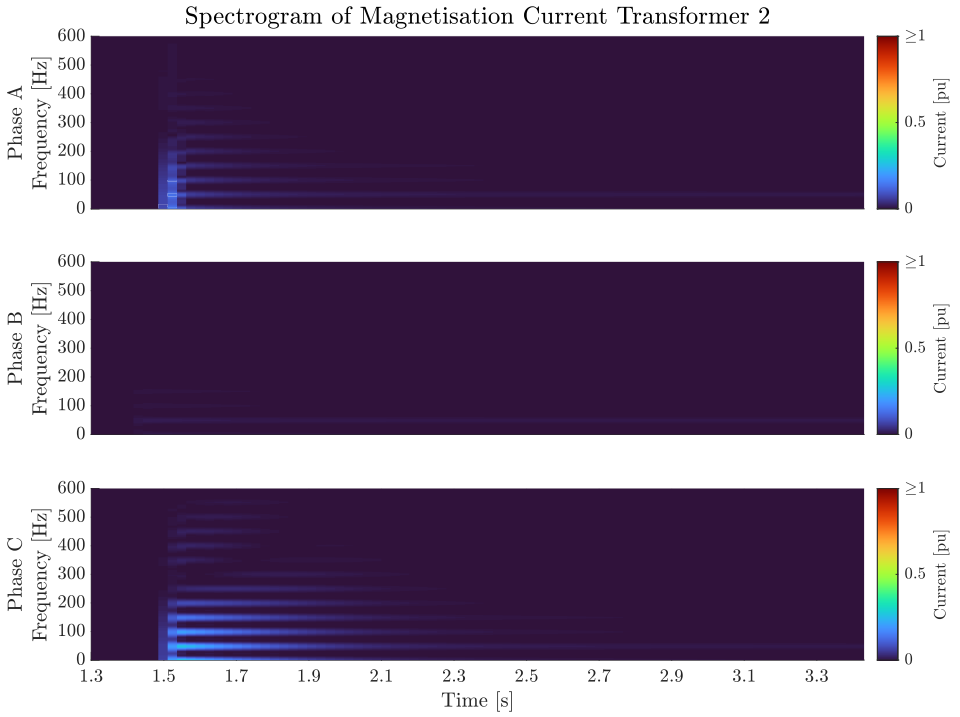

Figure B.5: Spectrogram of the amplitudes of the frequency component contained in the magnetisation current of *Transformer 2* with tap changer in *Transformer 1* and with PIRs in *BRK2* and *BRK3*. Note that the colour bar on the right side shows the current amplitude of the frequency components, where $1\,\mathrm{pu}$ corresponds to the nominal phase current of $0.189\,\mathrm{kA}$.

Here it can be seen that the most prominent frequency components in the magnetisation current of *Transformer 2* are the DC component ($0\,\mathrm{Hz}$) and the 2nd, 3rd, 4th and 5th harmonic. These reach their maximum shortly after the energisation of *Transformer 2* at $1.5\,\mathrm{s}$, which correlates with the magnetisation current shown in Figure 5.9. It can also be observed that the amplitudes of the 6th and 7th harmonics in particular do not decay evenly, but show slight fluctuations.
Overall, the occurrence of low-order harmonics, in particular even harmonics, and the described harmonic amplitude swings correspond to the typical characteristics of magnetisation currents of saturated magnetic cores during transformer energisation [68], [71]. However, since not all frequency characterises seen in the spectrogram of the current between the filter and *Transformer 2* in Figure B.4 can be linked to the magnetisation current, it can be assumed that further components are involved in the composition of its frequency components. This is, however, not investigated further in this project.

B.3 Energy Dissipation PIR

In the following figure, the energy dissipation of the PIRs implemented in the breakers *BRK2* and *BRK3* is calculated.

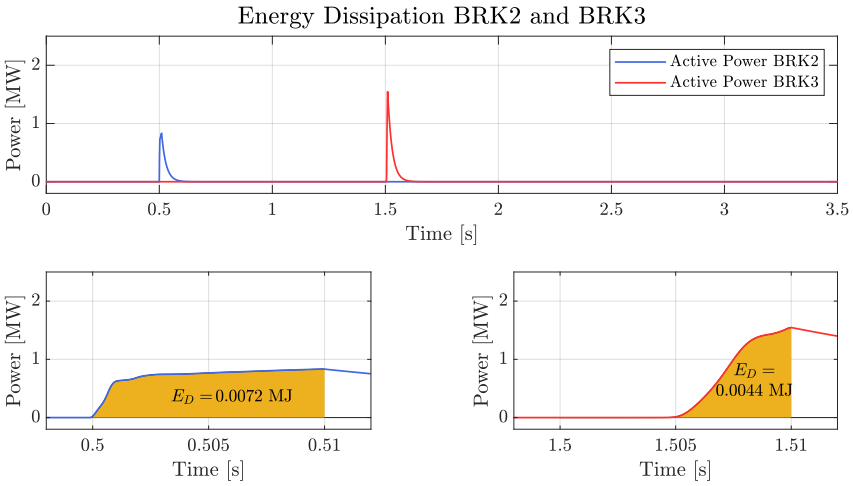

Figure B.6: Active power loss through breakers *BRK2* and *BRK3*, calculated from the difference between the active power flow before and after the breakers (upper subfigure) and their respective energy dissipation during their on-time of 10 ms (lower zoomed subfigures).

The approximated energy dissipation is determined by applying the trapezoidal numerical integration method. This is done by gradually integrating and summing the area under the active power curve using the MATLAB command *trapz*.

C Appendix: Black Start with Voltage Source

This Section provides additional figures for the investigations of the black start with an ideal voltage source in Section 5.2. This includes the magnetisation currents of *Transformer 1* in Figure C.1 and the line-line RMS voltages at *Bus1* and *Bus3* in Figure C.2.

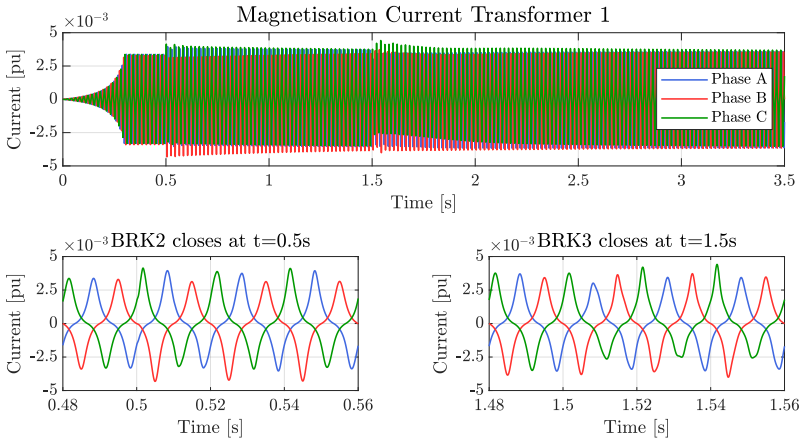

Figure C.1: Magnetisation currents of *Transformer 1*, mentioned in Section 5.2 "Black Start with Voltage Source". Note that the polarity of the magnetisation current is changed to match other current measurements, as PSCAD measures magnetisation current in the transformer model with opposite polarity.

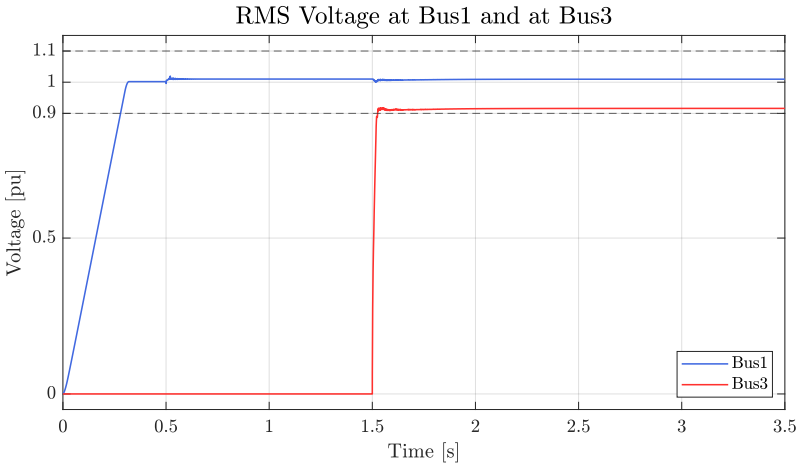

Figure C.2: Response of the line-to-line RMS value at *Bus1* and *Bus3* during the black start with the ideal voltage source. Note that 1 pu correspond to a line-line RMS voltage of 33 kV and 220 kV respectively. The RMS value is calculated digitally in PSCAD for each simulation time step with an observation window of 20 ms.

D Appendix: Black Start with STATCOM-BESS

This appendix provides additional investigations into the black start of the system up to *Bus4* using *STATCOM-BESS* as the black start service provider.

D.1 Investigations on Signal Filtering

As discussed in Section 5.3, investigations into signal filtering are to be carried out in order to improve the robustness and thus the performance of the controller of the *STATCOM-BESS* when voltage and current disturbances are present. Therefore, the effect of different characteristic frequencies f_0 of a second-order LPF, i.e. $20\,\mathrm{kHz}$, $2\,\mathrm{kHz}$ and $0.2\,\mathrm{kHz}$ on $v_{d,meas}$ and $v_{q,meas}$ will be investigated in this section. The transfer function of the second-order LPF from the PSCAD library [72] is shown in the following.

$$G(s) = \frac{1}{1 + 2\zeta\frac{s}{\omega_0} + \frac{s^2}{\omega_0^2}} \tag{D.1}$$

The damping ratio ζ of the second-order LPFs is chosen to be 0.9. The input signals $i_{d,meas}$ and $i_{q,meas}$ are also filtered by a second-order LPF. Its characteristic frequency is kept at $0.1\,\mathrm{kHz}$ and the damping ratio at 0.9 for this investigation, as these values have been found to be effective for the attenuation of disturbances in $i_{d,meas}$ and $i_{q,meas}$.

The effect of the filtering on v_{meas} and i_{meas} can be seen in Figure D.1 when energising the overhead line at $0.5\,\mathrm{s}$ and *Transformer 2* at $1.5\,\mathrm{s}$. For the investigation of the characteristic frequency of the filters, the phases with the most severe oscillations were chosen.

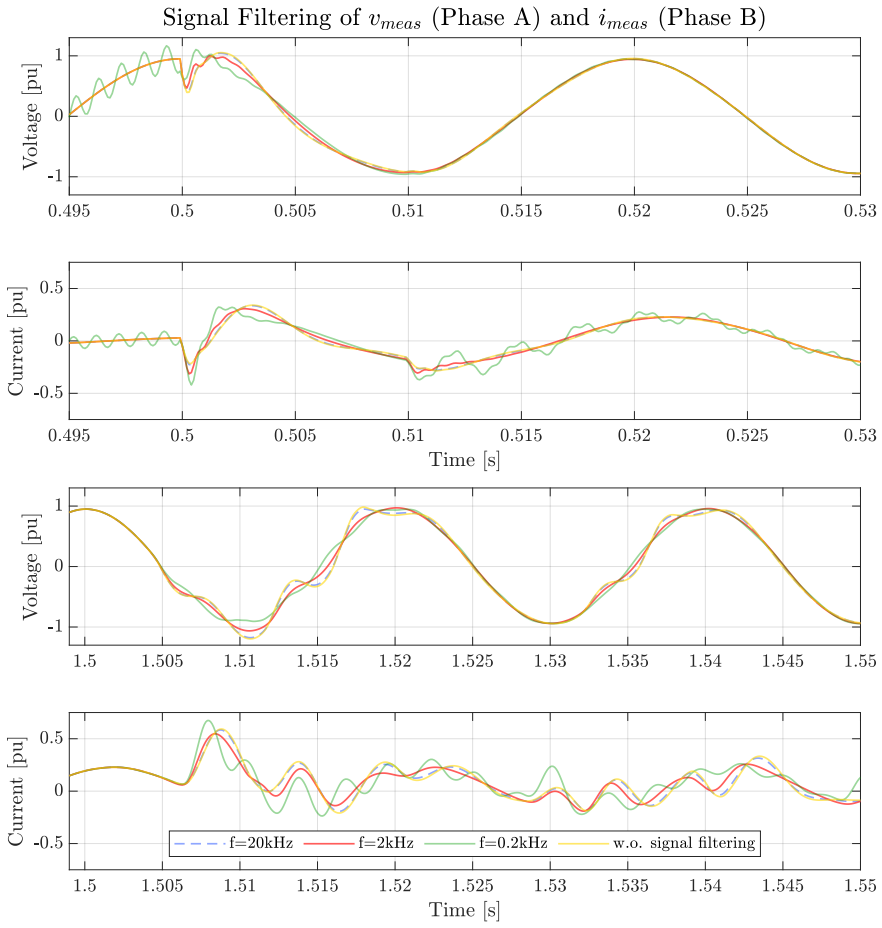

Figure D.1: Effect of signal filtering on v_{meas} (Phase A) and i_{meas} (Phase B) when applying different characteristic frequencies in a second-order LPF for filtering $v_{d,meas}$, $v_{q,meas}$, $i_{d,meas}$ and $i_{d,meas}$. Note that a second-order LPF with a characteristic frequency of $0.1\,\mathrm{kHz}$ is applied to the current in all subfigures, while the characteristic frequency of the second-order LPF applied to the voltage is varied.

In this figure, it can be seen that a characteristic frequency of $0.2\,\mathrm{kHz}$ even intensifies the already present voltage and current disturbances significantly, while $20\,\mathrm{kHz}$ have minimum to no filtering effect. For a characteristic frequency of $2\,\mathrm{kHz}$ the voltage and current disturbances can be significantly reduced. This value represents a compromise between damping capabilities and not decreasing the response time of the controller to ensure rapid counteraction to voltage swells and dips such as at $0.5\,\mathrm{s}$ in the first subfigure. It was also found that a characteristic frequency lower than $2\,\mathrm{kHz}$ can even lead to an increase in current transients. Thus a characteristic frequency of $2\,\mathrm{kHz}$ will be used for filtering $v_{d,meas}$ and $v_{q,meas}$ and $0.1\,\mathrm{kHz}$ for $i_{d,meas}$ and $i_{q,meas}$ in the following of this project.

D.2 RMS Voltages and Magnetisation Current

This section provides additional figures for the investigations of the black start with a *STATCOM-BESS* as described in Section 5.3. This includes the magnetisation currents of *Transformer 1* in Figure D.2 and the line-line RMS voltages at *Bus1* and *Bus3* in Figure D.3.

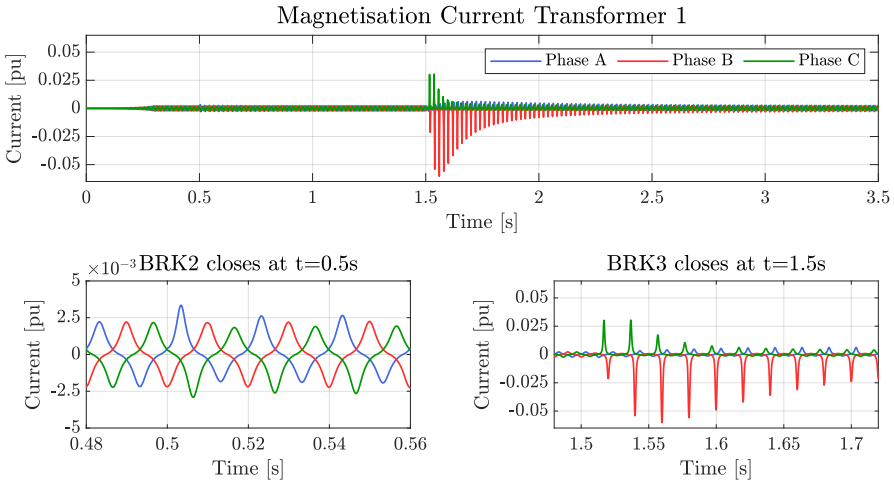

Figure D.2: Magnetisation currents of *Transformer 1* during the black start. Note that 1 pu corresponds to the nominal phase current of 1.262 kA and that the polarity of the magnetisation current is changed to match with Figure 5.13, as PSCAD measures magnetisation current in the transformer model with different polarity.

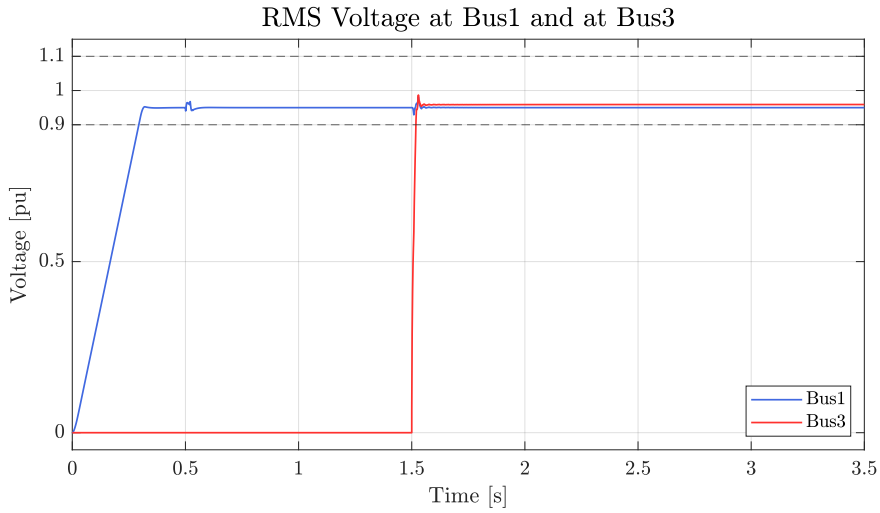

Figure D.3: Response of the line-to-line RMS value at *Bus1* and *Bus3* during the black start with the *STATCOM-BESS*. Note that 1 pu correspond to a line-line RMS voltage of 33 kV and 220 kV respectively. The RMS value is calculated digitally in PSCAD for each simulation time step with an observation window of 20 ms.

D.3 Harmonic Analysis for Black Start with STATCOM-BESS

Based on the descriptions and defined parameters in Section B.2, following three harmonic analyses are carried out in this section:

- Current measured between the filter and *Transformer 1*
- Current measured between the overhead line and *Transformer 2*
- Magnetisation current of *Transformer 2*

The corresponding spectrograms can be found in the following. Note that the colour bar only reaches up to $0.15\,\mathrm{pu}$ for better visibility of the present frequency components.

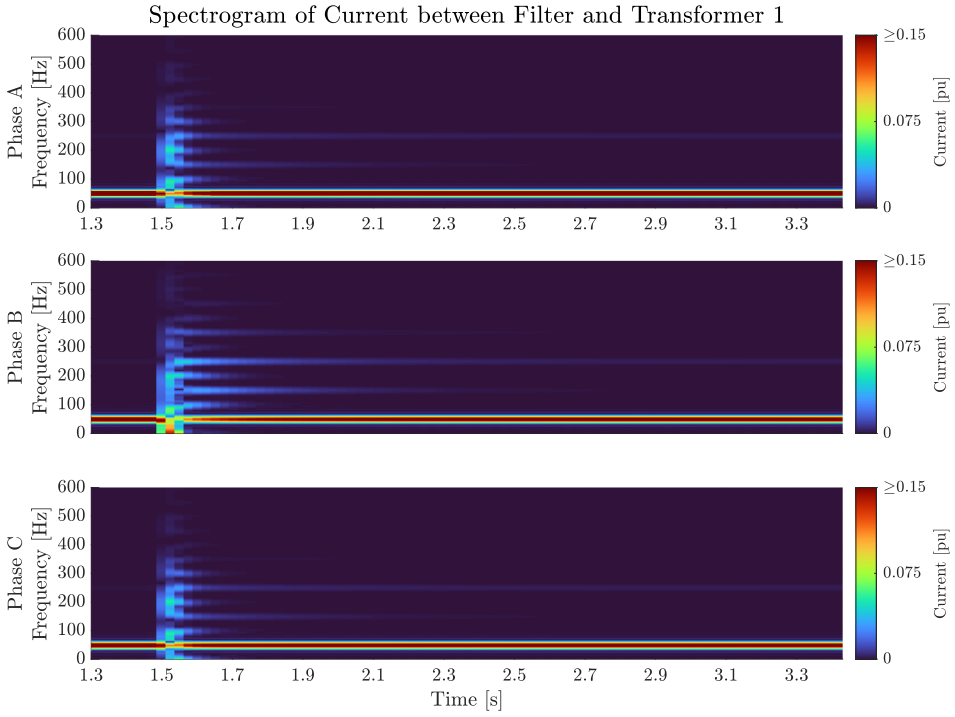

Figure D.4: Spectrogram of the amplitudes of the frequency component contained in current signal measured between the filter and *Transformer 1*. Note that the colour bar on the right side shows the current amplitude of the frequency components, where $1\,\mathrm{pu}$ corresponds to the nominal phase current of $1.262\,\mathrm{kA}$.

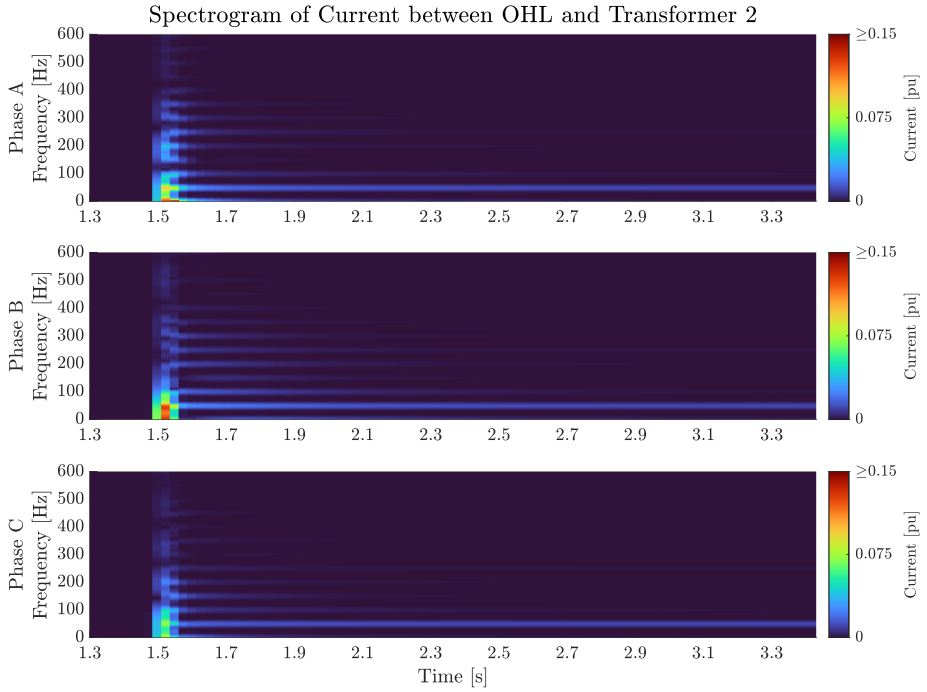

Figure D.5: Spectrogram of the amplitudes of the frequency component contained in the current between overhead line and *Transformer 2*. Note that the colour bar on the right side shows the current amplitude of the frequency components, where $1\,\mathrm{pu}$ corresponds to the nominal phase current of $0.189\,\mathrm{kA}$.

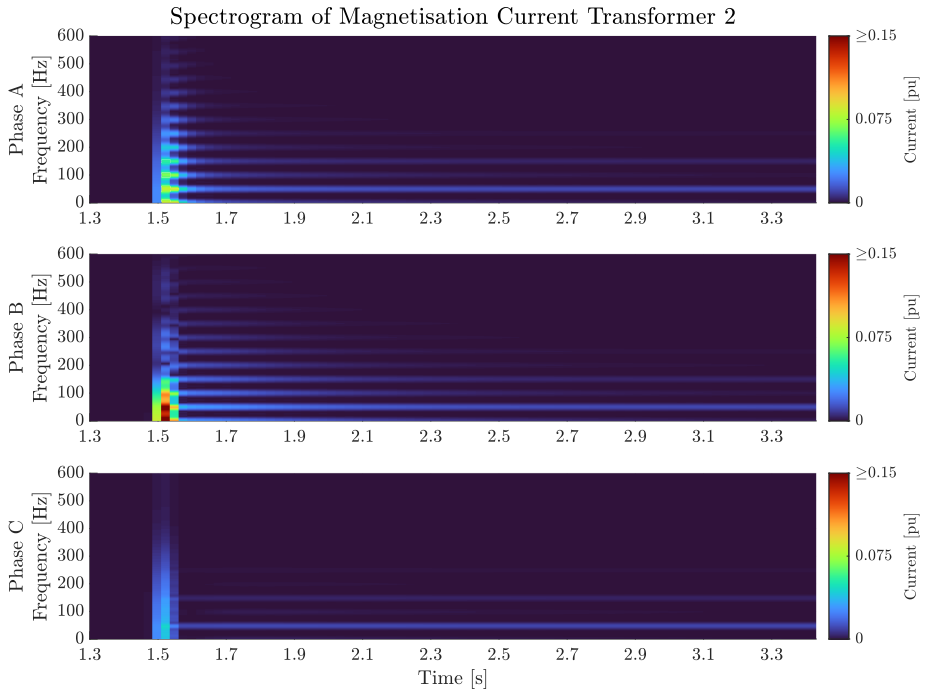

Figure D.6: Spectrogram of the amplitudes of the frequency component contained in the magnetisation current of *Transformer 2*. Note that the colour bar on the right side shows the current amplitude of the frequency components, where $1\,\mathrm{pu}$ corresponds to the nominal phase current of $0.189\,\mathrm{kA}$.

Figure D.4 shows that low-order harmonics with decreasing amplitude occur after *Transformer 2* is energised. It can also be seen that the 3rd and 5th harmonics decay the slowest and superimpose the current the longest. In addition, the presence of decreasing DC components can be identified, which is most prominent in Phase B. In Figure D.6 it can be seen that the amplitudes of the low-order frequency components are significantly higher in Phase A and B compared to Phase C. Further, it can be noted that the 2nd and 3rd harmonic components in Phase A and B superimpose the current magnetisation current the longest. It is also noticeable that the 3rd harmonic reaches a stagnation point in all phases, after which no further visible decay can be observed.
The Figures D.5 and D.6 highlight the difference between the characteristic of the transient inrush current between the overhead line and *Transformer 2* and the magnetisation currents of *Transformer 2*. It can be observed that the magnetisation currents in Phase A and B have higher amplitudes than the current measured between the overhead line and *Transformer 2*. In Phase C of the current between the overhead line and *Transformer 2*, frequency components occur that are not recognisable in the magnetisation currents. This allows the conclusion that, in addition to the magnetisation currents, further components are involved in the composition of the frequency components shown in Figure D.5 and thus in Figure D.4. However, this is not further investigated in this project.

E Appendix: Block Loading

In this appendix, relevant parameters used to model the GFL unit and the squirrel cage induction motor are shown. Furthermore, additional figures and descriptions for the analysis of the block loading of dynamic and static loads in Chapter 6 can be found.

E.1 Modeling of the GFL unit and Induction Motor

Table E.1 provides an overview of the parameters used for the modelling of the GFL unit connected to *Bus4*. The series reactor and the shunt capacitor form the LC filter of the GFL unit, whose values are calculated based on Section 4.1. It should also be noted that the parameters T_{LPF} refer to the time constant of the corresponding LPFs marked in Figure 6.2. Moreover, the parameters K_p and T_i refer to the proportional gain and the integrator time constant of the tuned PI controllers in the corresponding GFL control loops.

Table E.1: Overview of the ratings and parameters used for the modelling of the GFL unit.

GFL unit			
Nominal Ratings and Filter		**Control Parameters**	
Nominal apparent power	10.53 MVA	f-P Control	K_f: 3 T_{LPF}: 0.01 s
Nominal reactive power	$\pm$3.29 Mvar	MAF	Number of Samples: 200 Frequency: 50 Hz Initial Output: 50 Hz
Nominal active power	10 MW	V-Q Control	K_v: 3.12 T_{LPF}: 0.01 s
Nominal voltage (L-L,RMS)	33 kV	Power Control	K_P: 0.375, T_i: 0.1 s
Nominal phase current (Peak)	0.261 kA	Current Control	K_P: 0.375, T_i: 0.1 s T_{LPF}: 0.001 s
Base impedance	103.41 Ω	PLL	K_P: 9.16, K_i: 0.82
Series reactor	16.45 mH		
Shunt capacitor	1.54 μF		

Table E.2 provides the main motor parameter of the squirrel cage induction motor used for the dynamic load model that is connected to the distribution system.

Table E.2: Overview of the parameters of the squirrel cage induction motor used for the dynamic load model.

Technical Data Induction Motor	
Motor type	Squirrel cage induction motor
Nominal apparent power	3 MVA
Nominal voltage (L-L,RMS)	33 kV
Nominal phase current (Peak)	74.2 A
Base angular frequnecy	314.16 rad/s
Angular moment of inertia	0.742 s
Stator resistance	0.0054 pu
Rotor resistance	0.00607 pu

E.2 Static Load

In Figure E.1, the effect of signal filtering in the f-P droop control of the GFL unit is demonstrated.

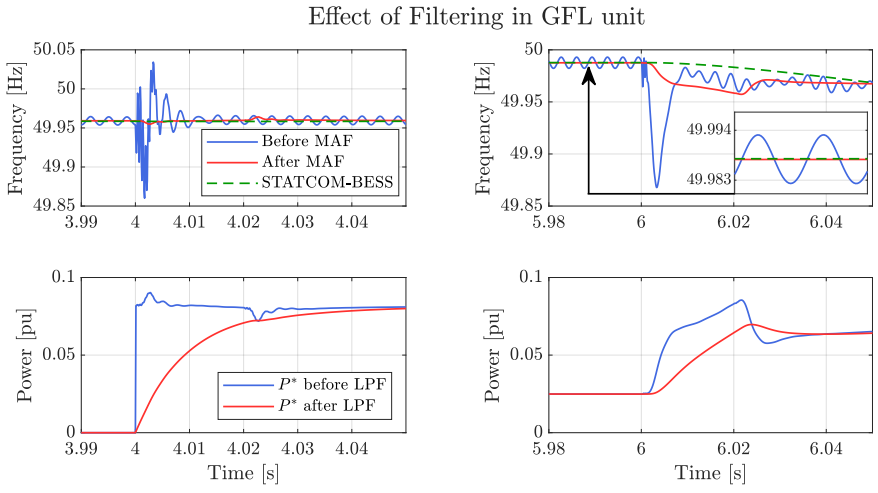

Figure E.1: Effect of the MAF and LPF in the f-P droop control of the GFL unit. It should be noted that the GFL unit is energised for the first time at 4 s.

The effect of the MAF on the frequency estimation of the PLL can be seen in the top two subfigures. It is noteworthy here that the MAF significantly smoothes the frequency disturbances occurring when energising the GFL unit including its LC filter and the static load. In addition, it proves to be efficient in eliminating steady-state ripples in the frequency estimation, resulting in only minor errors in tracking the frequency set by the *STATCOM-BESS* in a steady state.

In the lower subfigures, the impact of the LPF on the active power reference is shown. Here, it can be seen that rapid changes can be absorbed by the LPF, which reduces the overall rate of change of the active power reference of the GFL unit. In addition, residual oscillations are damped.

In Figure E.2 the active power, reactive power and the frequency response of the *STATCOM-BESS* during the block loading with and without the GFM unit connected are further investigated.

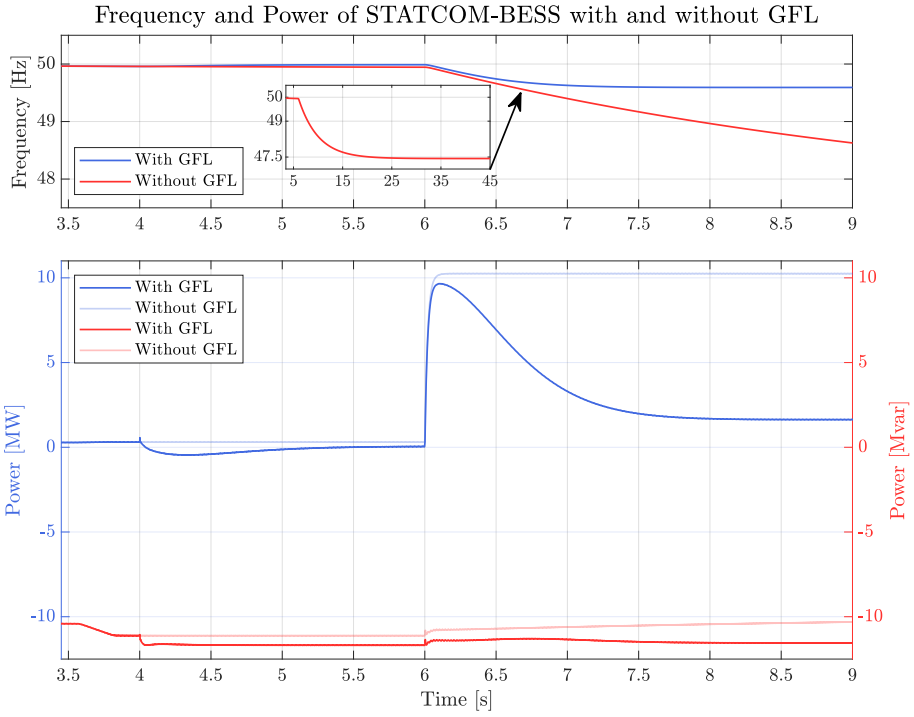

Figure E.2: Active power, reactive power and the frequency response of the *STATCOM-BESS* with and without the GFM unit connected. Additionally, the upper subfigure has a zoom-out showing the total frequency drop of the *STATCOM-BESS* without the GFL unit for 45 s.

For the frequency response of the *STATCOM-BESS* without the support of the GFL unit, the frequency drops to a minimum of 47.44 Hz, while with the GFL unit connected, the frequency only drops to 49.59 Hz. The reason for the frequency dropping below 47.5 Hz is the active power output of the *STATCOM-BESS*, exceeding 10 MW, as shown in the bottom subfigure in Figure E.2. This is caused by the active power drawn by the static load along with transmission losses.
Another notable observation is that the reactive power absorbed by the *STATCOM-BESS* is lower when the GFL unit is not connected. This is primarily due to the capacitance of the filter of the GFL unit providing around 0.5 Mvar and to a much lesser extent to the local supply of the passive components, e.g. *Transformer 2*, by the GFL unit. If the current is only supplied by the *STATCOM-BESS* instead, it has to flow over a comparatively long distance causing reactive power losses at the inductive components of the

transformer and the overhead line. These reactive power losses slightly compensate for the reactive power caused by the capacitive components in the system. The described effects of reduced reactive power in the system due to load current that is provided by the *STATCOM-BESS* can also be observed between 6 s and 7.5 s with the GFL unit connected, where an initial high current from the *STATCOM-BESS* towards the static load compensates partly the reactive power provided by the overhead line *OHL50*.
Furthermore, there is a gradual decrease in reactive power from 6 s, which is particularly noticeable in the test case without the GFL unit. The reason for this is the drop in frequency to 47.44 Hz, which affects the impedance of frequency-dependant components such as filters and the overhead line *OHL50*. Therefore the reactive power of these components is influenced. In the case with support from the GFL unit, the frequency deviation is so small, that frequency-dependant deviations in reactive power are not visible.

E.3 Dynamic Load

For a better understanding of the effect of the power response of the GFL unit, the dynamic load test case from Figure 6.9 in Section 6.3 is repeated in the below Figure E.3. This time, only the power response of the *STATCOM-BESS* is shown, while the GFL unit is connected or disconnected. The dynamic load is again set to be 5 MVA, with 3 MVA falling onto the induction motor.

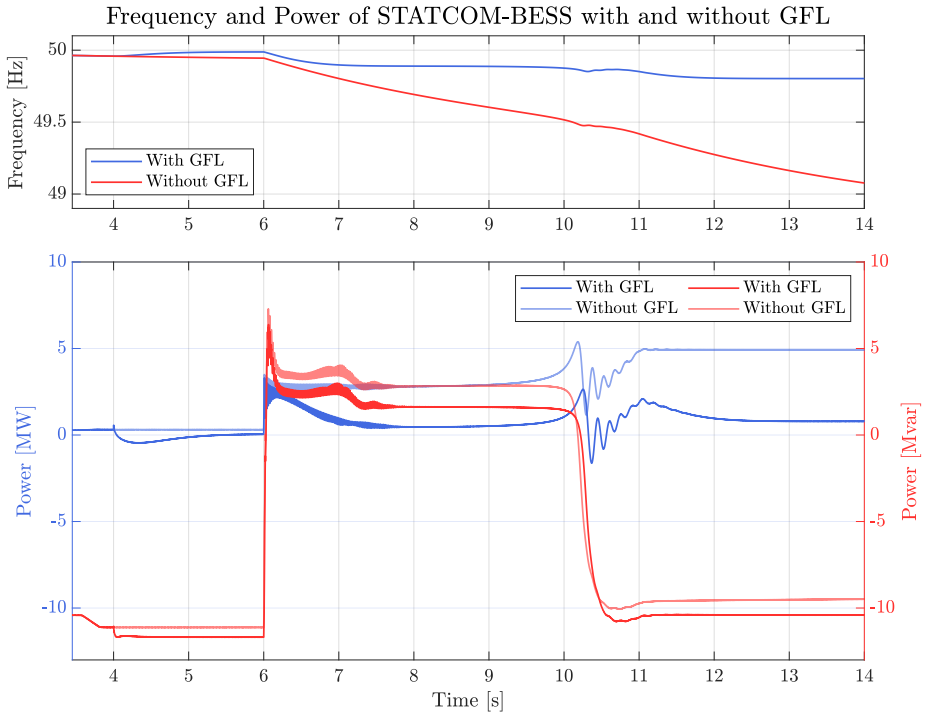

Figure E.3: Frequency and power response of the *STATCOM-BESS*, with and without support from the GFL unit. The GFL unit is connected at 4 s and the dynamic load is connected at 6 s.

The upper subfigure shows the frequency response of the *STATCOM-BESS* with and

without the support of the GFL unit. It can be seen that the GFL unit limits the frequency of the *STATCOM-BESS* to $49.8\,\mathrm{Hz}$ ultimately when the power demand reaches a steady state. Without GFL unit, the frequency is still decaying toward an estimated value of $48.75\,\mathrm{Hz}$, according to its steady-state active power output of about $5\,\mathrm{MW}$.
The lower subfigure shows that the GFL supports the *STATCOM-BESS* in terms of active power, but due to its V-Q droop characteristic rarely in reactive power. Still, its active power support affects the reactive power flow in the system.
From $4\,\mathrm{s}$ to $6\,\mathrm{s}$ and after $10\,\mathrm{s}$, the GFL unit provides the majority of active power, leading to an unloaded overhead line. The reactive power produced by the overhead line is not compensated by a load current flow through its inductive components, and the reactive power has to be absorbed by the *STATCOM-BESS*. However, during the acceleration period of the induction motor, the produced reactive power of the overhead line is helpful to support the reactive power demand of the induction motor and therefore de-loads the *STATCOM-BESS* in this period.
Overall, it can be seen that the connection of the GFL unit does not cause further oscillations in the power output of the *STATCOM-BESS*. This proves that the GFL unit and the *STATCOM-BESS* have a stable interaction even under fast-changing load conditions, as seen at around $11\,\mathrm{s}$.